NON-EQUILIBRIUM CURRENT FLUCTUATIONS IN GRAPHENE

A Thesis
Presented to
The Academic Faculty

by

Alexander David Wiener

In Partial Fulfillment
of the Requirements for the Degree
Doctor of Philosophy in the
School of Physics

Georgia Institute of Technology
May 2013

NON-EQUILIBRIUM CURRENT FLUCTUATIONS IN GRAPHENE

Approved by:

Professor Markus Kindermann,
Advisor
School of Physics
Georgia Institute of Technology

Professor Carlos Sa de Melo
School of Physics
Georgia Institute of Technology

Professor Walter de Heer
School of Physics
Georgia Institute of Technology

Professor Angelo Bongiorno
School of Chemistry
Georgia Institute of Technology

Professor Phillip N. First
School of Physics
Georgia Institute of Technology

Date Approved: 5 December 2012

For my teachers

"Bitter are the roots of study, but how sweet their fruit."

Aristotle

ACKNOWLEDGEMENTS

More people deserve acknowledgement for their assistance in this work than I could recognize in one thesis. Besides my parents, who were an endless source of support emotionally, intellectually and occasionally financially, I wish to thank my friends Brett Ashenfelter and Lillian MacLeod for their love and encouragement throughout this long process. I also owe a debt to the staff and to all of my friends in the School of Physics. In particular, I thank Ed Greco, Daniel Borrero, Danny Caballero, Adam Perkins, Lee Miller, Chris Malec, Jeremy Hicks and anyone else I've forgotten for their companionship and for thoughtful discussions on many topics. I am especially thankful for the collaboration and commiseration of Seungjoo Nah, who's influence throughout this process has been invaluable. This work would not have been completed without the intellectual and emotional support of all of these people, and I am grateful for the role they have played in this period of my life. Finally, I thank my teachers, past and present, for sharing their unique understanding of the world and for encouraging me to form my own. In particular, this work would not have been possible without the guidance of my advisor Markus Kindermann, or the committee members who generously offered their time in my assistance.

TABLE OF CONTENTS

LIST OF TABLES

LIST OF FIGURES

SUMMARY

We analyze experimental evidence of transport through evanescent waves in graphene, reconciling existing experimental data with theory. We propose novel experimental geometries that provide more compelling evidence of evanescent waves. We investigate the shot noise generated by evanescent modes in graphene for several experimental setups. For two impurity-free graphene strips kept at the Dirac point by gate potentials, separated by a long highly doped region, we find that the Fano factor takes the universal value $F = 1/4$. For a large superlattice consisting of many strips gated to the Dirac point, interspersed among doped regions, we find $F = 1/(8 \ln 2)$. These results differ from the value $F = 1/3$ predicted for a disordered metal, providing an unambiguous experimental signature of evanescent mode transport in graphene. For a graphene nano-ribbon transistor geometry, we explain that the experimentally observed anomalous voltage scale of the Fano factor can arise from doping by the contacts to the electrical circuit. These observations provide strong evidence of evanescent mode transport in graphene.

CHAPTER I

INTRODUCTION

Carbon, the basis of organic chemistry, is one of the few elements known since antiquity. [61] The sixth element, carbon has four valence electrons, and can form many structures with a variety of physical properties. For instance, graphite, a three dimensional form of carbon, is an opaque conductor made of many stacked atomic carbon layers that are weakly bound by van der Waals forces. Known to humans since the fourth millennium B.C. when it was used in southeastern Europe to paint decorative pottery, [61] graphite is soft enough to shed some of its weakly bound layers when rubbed on paper. In contrast, diamond is a face-centered cubic form of carbon that is transparent, electrically insulating and one of the hardest known materials. Due to the variety of structures it can form, carbon provides a fertile subject for scientific inquiry.

Graphene is a two dimensional carbon structure with atoms arranged in a hexagonal honeycomb lattice (see Fig. 1). A popular research subject in several fields, graphene has many electronic and mechanical properties with potential applications in future generations of nano-engineered materials. In addition to high structural rigidity, graphene has an unusual electronic band structure, with low energy excitations described by massless chiral Dirac fermions. These particles obey the rules of quantum electrodynamics despite traveling roughly 300 times slower than the speed of light. [41, 87, 86] Graphene is therefore interesting from a theoretical point of view, exhibiting exotic quantum relativistic effects such as Klein tunneling and zitterbewegung in an ordinary, non-relativistic condensed matter setting.

Since 2004, researchers have experimentally and theoretically investigated many

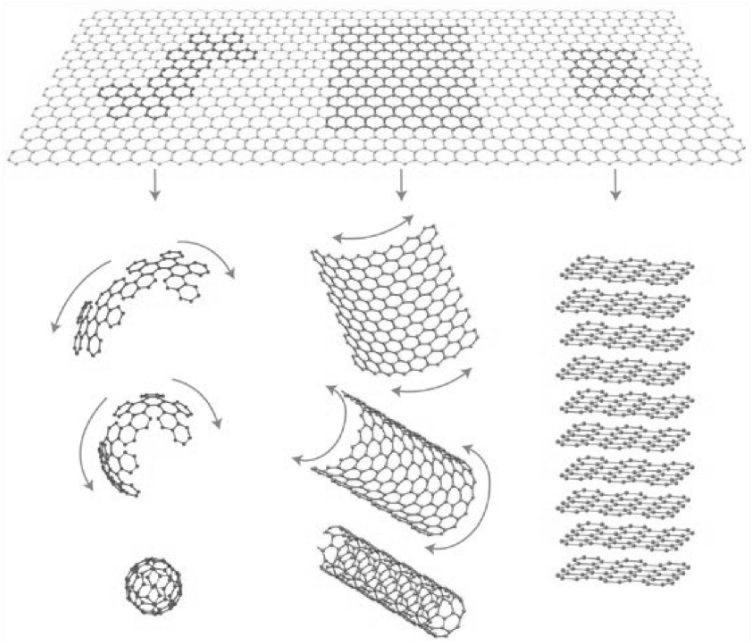

Figure 1: Carbon allotropes in different dimensions. Graphene (2D) can be cut and folded into fullerenes (0D) and carbon nanotubes (1D). Graphite (3D) consists of vertically stacked layers of 2D graphene. (Adapted from Geim *et al.* [68])

properties of graphene, including Klein tunneling, [87] ballistic transport, [121] magnetic phenomena, [74, 133] the integer quantum hall effect, [122, 184] and disorder effects [113] and their connections to soft membranes [120] and quantum gravity in curved space. [62] Graphene also displays unusual mesoscopic effects [133, 86] that can arise from the boundary conditions for various edge types. [116, 173, 134, 3] The unique electronic properties of graphene are attractive for many potential applications in next generation electronics, such as valleytronic [166, 143] and field effect transistor devices. [46, 79, 97, 166, 178, 64, 183]

Graphene is also useful as a theoretical building block for other carbon allotropes of different dimensionality, as illustrated in Fig. 1. A rolled up graphene sheet with pentagons introduced to the lattice forms a fullerene, [7] a spherical carbon molecule

with discrete energy states. Rolling the graphene sheet along one direction and connecting carbon bonds at the former edges creates a one-dimensional carbon nanotube, [144, 45] another structurally robust carbon allotrope with interesting electronic properties. Graphite, a three dimensional carbon structure, consists of stacked layers of graphene that are coupled weakly by van der Waals interactions. Graphene is a useful model system for a number of carbon structures, and this insight motivated the earliest graphene studies.

While the production of single layer graphite most likely began with the invention of the pencil around 1564, [135] scientific studies of graphene started in the 19th century. By the 1800s, scientists were aware of the layered structure of bulk graphite, and several exfoliation techniques were known. [54] One method, developed by Edward Goodrich Acheson, [2] produced colloidal graphitic suspensions which likely contained small monolayer graphene flakes. More significantly, Acheson discovered silicon carbide (SiC), which he called "carborundum." While SiC was initially used as an abrasive, Acheson later found that the silicon tends to evaporate upon heating, leaving behind high purity graphite. This insight gained importance nearly a century later, when researchers began to study graphite and SiC for their electronic properties and discovered that graphene layers can form on a SiC substrate.

Early experimental work in thin graphitic films began with Brodie's 1859 production [32] of "graphitic oxide," consisting of graphene sheets with extra functional hydrogen and oxygen groups connecting adjacent carbon atoms. Brodie found that he could separate individual layers by immersing the material in water. Nearly a century later, in 1962, Boehm found a way to use hydrazine in order to reduce the graphite oxide to graphene monolayers, creating and measuring the first suspended graphene flakes. [27] Boehm also first provided a name for graphene in 1982. [28] He viewed graphene as a macromolecule, and chose the suffix -*ene* to describe hydrogen at the edges of the "molecule."

Graphene growth gained popularity in the latter quarter of the 20th century following a study of the graphitic layers formed in heated SiC by van Bommel *et al.* [168] This work confirmed the observation of Acheson that graphitic layers form when silicon sublimates through the crystal faces. Furthermore, van Bommel *et al.* noted an asymmetry between growth on the carbon and silicon terminated crystal faces. While graphite growth on the silicon face is epitaxial (aligned with the silicon substrate), growth on the carbon terminated face is rotationally disordered.

Forbeaux *et al.* [65] confirmed these findings in 1998, and found that the graphite layers are essentially electronically decoupled from the substrate. This observation suggested that freely suspended graphene layers can grow on top of a SiC substrate, a single layer at a time. Ruoff *et al.* recognized the importance of this discovery and developed a method for mechanically exfoliating graphene in 1999. [108] This method was later adapted by Novoselov and Geim *et al.* in their landmark 2004 paper, [121] credited with starting the graphene revolution. Concurrently, de Heer *et al.* have pioneered the synthesis and characterization of epitaxial graphene as an electronic material. [20, 54]

Theoretical studies of graphene began after the second world war, when graphite became crucial for its role in moderating nuclear reactions. P. R. Wallace first calculated the band structure of graphene in 1947, [174] using the tight-binding model as a step toward determining the electronic structure of bulk graphite. This calculation was subsequently improved and expanded by others, resulting in the Slonczewski-Weiss-McClure (SWM) band structure of graphite, [110, 154] which was able to describe many experimental observations. [29, 111, 158, 157, 179, 60] In the 1980s, Semenoff [151] and Haldane [75] recognized the connection between the graphene Hamiltonian for low energy carriers and the massless Dirac equation, providing a link between conventional condensed matter systems and quantum electrodynamics. This connection generated much theoretical interest in graphene, [71, 145, 6, 72, 185]

which became relevant to experiments on carbon nanotubes prior to the celebrated 2004 work of Novoselov and Geim *et al.* [121]

Non-equilibrium current fluctuations, or shot noise, provide an important diagnostic quantity for mesoscopic physics. Such fluctuations arise from the quantized nature of the charge carries in electrical conductors, and they becomes less important as the size of the conductor increases and the number of carriers becomes large. Shot noise measurements supply information about the temporal correlations of the charge carriers. This is in contrast to the current correlations arising from thermal fluctuations in electron occupation numbers, which do not contain any more information than conductance measurements alone. Shot noise yields information beyond the conductance, and is a useful quantity for studying transport in mesoscopic systems.

The shot noise in ballistic graphene [121, 184, 20, 42] has attracted much attention since the seminal paper by Tworzydło *et al.*, [167] which showed that shot noise can be generated in an impurity-free sheet of graphene. This result is surprising at first sight, as the shot noise vanishes in conductors without electron scattering. [88, 98, 138, 90] The unanticipated noise is caused by evanescent (exponentially damped) waves that backscatter electrons, even in clean graphene.

Tworzydło *et al.* [167] showed that the shot noise in a clean sheet of graphene at its Dirac point, i.e., zero chemical potential, is not only non-zero, but also universal. The shot noise normalized by the mean current and expressed in units of the electron charge e (this quantity is commonly referred to as the Fano factor F) takes the value $F = 1/3$ for short and wide graphene strips. This prediction has generated much theoretical interest in the topic, [43, 142, 155, 146, 102, 150, 156, 70] and considerable experimental activity. [59, 50]

So far, two experiments [59, 50] have tested the prediction of Tworzydło *et al.*, [167] measuring a Fano factor close to $F = 1/3$. However, the universal shot noise value for evanescent mode transport at the Dirac point of graphene [167] is identical to

the one expected for conventional disordered conductors in the diffusive regime, [19] making the interpretation of these experiments ambiguous. It has been confirmed in numerous regimes, both with [70] and without [146, 102, 150, 156] electron-electron interactions, that a Fano factor close to $F = 1/3$ is also expected for disordered graphene, independent of the chemical potential. Therefore, the measured Fano factor $F = 1/3$ could be due to either evanescent mode transport or impurities in the measured samples.

The experiment of Danneau *et al.* [50] also measured a strong dependence of the Fano factor on the chemical potential, an additional signature of evanescent mode transport. Such dependence on the chemical potential is expected for clean graphene; [167, 150, 156] as the chemical potential departs from the Dirac point, an increasing number of evanescent waves become propagating and cease to backscatter electrons, decreasing the Fano factor. The observed dependence of F on the chemical potential does not occur in generic diffusive conductors, [146, 102, 150, 156] making it a more distinctive signature of evanescent mode transport.

However, other scenarios are also consistent with the doping dependence of F reported by Danneau *et al.*, [50] such as energy dependent scattering. This ambiguity must be resolved by additional experimental signatures of transport through evanescent modes in graphene. Furthermore, the energy scale of the measured dependence of the Fano factor on the chemical potential was considerably larger than theory predicts. [167] As the dependence of F on the chemical potential provides the main evidence for evanescent wave transport in the experiment, [50] this deviation from the theoretical prediction requires explanation. Motivated by these observations, we present new theoretical results in order to explain the anomalous Fano factor energy scale observed. We also propose new experimental geometries for which the shot noise takes novel, unambiguous values.

This thesis is organized as follows. In Chp. 2, we review a theoretical model for

graphene based on a tight binding approach, resulting in the massless Dirac Hamiltonian for low energy charge carriers. We then describe the formalism used for calculations of Klein tunneling, which we employ throughout this thesis. A discussion of shot noise follows in Chp. 3, including a summary of research on shot noise in graphene, emphasizing the shortcomings of existing theoretical and experimental results. To resolve the ambiguity in the predicted shot noise value for clean graphene, we propose in Chp. 4 several experimental geometries for which the shot noise shows unambiguous signatures of evanescent mode transport. The dependence of the Fano factor on chemical potential measured by Danneau *et al.* [50] is the subject of Chp. 5, where we show that the anomalously large energy scale observed is consistent with the theory of evanescent modes when the effects of doping by the leads are included. We conclude with a summary in Chp. 6.

CHAPTER II

THE ELECTRONIC STRUCTURE OF GRAPHENE

In this chapter, we review the lattice structure and basic electronic properties of monolayer graphene, beginning with the work of Wallace. [174] We use a tight-binding model to calculate the linear dispersion relation for low energy charge carriers. A Fourier transform results in the massless Dirac Hamiltonian, the basis of the theoretical model considered throughout this thesis. With the analogy to quantum electrodynamics established, we describe a few consequence of this connection, including electron helicity and Klein tunneling.

2.1 Lattice structure and dispersion relation

Monolayer graphene consists of a single atomic layer of carbon atoms arranged in a hexagonal lattice. We model it using a triangular lattice with a basis containing two atoms labelled A and B, as in Fig. 2a. While models also exist for bilayer and multilayer graphene, we consider only monolayer graphene in this thesis, referred to henceforth as simply "graphene."

Carbon has four valence electrons in a $2s^2 2p^2$ configuration. In graphene, the carbon atoms sp^2 hybridize, forming three sp^2 orbitals and one leftover half-filled p orbital. The hybridized sp^2 orbitals form σ bonds with in-plane nearest neighbors, creating a filled valence band. The leftover p orbital forms covalent bonds with nearby carbon atoms, creating an out-of-plane conducting π band, which is half filled.

The graphene lattice vectors are given by

$$\begin{aligned} \vec{a}_1 &= \frac{a}{2}\left(3, \sqrt{3}\right) \\ \vec{a}_2 &= \frac{a}{2}\left(3, -\sqrt{3}\right), \end{aligned} \tag{1}$$

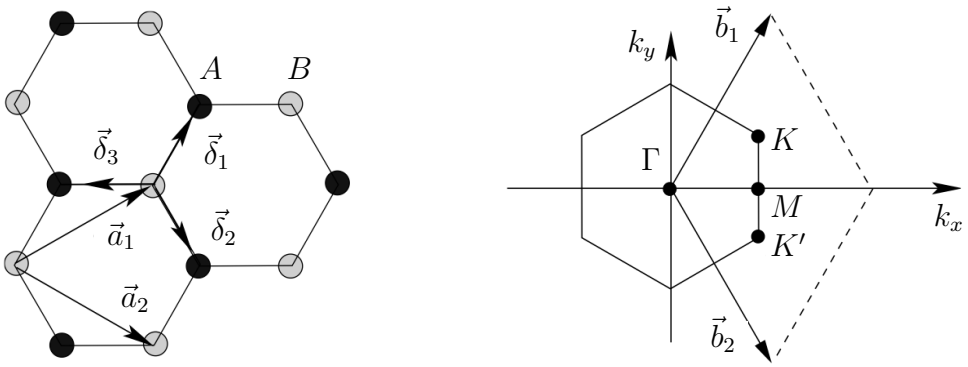

Figure 2: The hexagonal graphene lattice (a) with two carbon atoms per unit cell, labelled A and B. The lattice vectors are $\{\vec{a}_i\}$ and the nearest neighbor vectors are $\{\vec{\delta}_i\}$. The corresponding Brillouin zone (b) is also hexagonal, with reciprocal lattice vectors $\{\vec{b}_i\}$ and Dirac cones located at the K and K' points. (Adapted from Castro Neto *et al.* [42])

where $a \approx 1.42$ Å is the carbon-carbon distance, or lattice constant. The nearest neighbor vectors, which are inter-sublattice (A-B), are

$$\begin{aligned}\vec{\delta}_1 &= \frac{a}{2}\left(1, \sqrt{3}\right) \\ \vec{\delta}_2 &= \frac{a}{2}\left(1, -\sqrt{3}\right) \\ \vec{\delta}_3 &= -a\left(1, 0\right),\end{aligned} \tag{2}$$

and the next nearest neighbor vectors, which are intra-sublattice (A-A or B-B), are given by $\vec{\delta}'_1 = \pm\vec{a}_1$, $\vec{\delta}'_2 = \pm\vec{a}'_2$ and $\vec{\delta}'_3 = \pm\left(\vec{a}_2 - \vec{a}_1\right)$. In reciprocal space, the Brillouin zone is also hexagonal, with two independent corners labelled K and K'. These points are also referred to as Dirac points for reasons that will be made clear later in this chapter. The rest of the Brillouin zone corners can be connected to K and K' by linear combinations of the reciprocal lattice vectors

$$\begin{aligned}\vec{b}_1 &= \frac{2\pi}{3a}\left(1, \sqrt{3}\right) \\ \vec{b}_2 &= \frac{2\pi}{3a}\left(1, -\sqrt{3}\right).\end{aligned} \tag{3}$$

The K and K' points play a crucial role in the transport properties of graphene, and most of the work done on the physics of charge carriers in graphene concerns carriers within $|\vec{q}| \ll 2\pi/a$ of the Dirac points, whose locations in momentum space are given by

$$\begin{aligned} \vec{K} &= \frac{2\pi}{3a}\left(1, \frac{1}{\sqrt{3}}\right) \\ \vec{K}' &= \frac{2\pi}{3a}\left(1, -\frac{1}{\sqrt{3}}\right). \end{aligned} \tag{4}$$

The tight-binding Hamiltonian for electrons in graphene, including both nearest neighbors and next nearest neighbors and expressed in units where $\hbar = 1$, is given by

$$H = -t \sum_{\langle i,j\rangle,\sigma} \left(a^\dagger_{\sigma,i} b_{\sigma,j} + \text{H.c.}\right) - t' \sum_{\langle\langle i,j\rangle\rangle,\sigma} \left(a^\dagger_{\sigma,i} a_{\sigma,j} + b^\dagger_{\sigma,i} b_{\sigma,j} + \text{H.c.}\right), \tag{5}$$

where $t \approx 2.5$ eV and $t' \approx 0.1$ eV are the nearest and next nearest neighbor hopping energies, $a^\dagger_{\sigma,i}$ ($a_{\sigma,i}$) creates (annihilates) an electron with spin $\sigma \in \{\uparrow, \downarrow\}$ on site $\vec{R}_i$ on sublattice A (a similar definition for sublattice B is assumed) and "H.c." denotes the Hermitian conjugate.

The corresponding dispersion relation, first derived by Wallace [174], is given by

$$\begin{aligned} E_\pm(\vec{k}) &= \pm t\sqrt{3 + f(\vec{k})} - t' f(\vec{k}) \\ f(\vec{k}) &= 2\cos\left(\sqrt{3}k_y a\right) + 4\cos\left(\frac{\sqrt{3}}{2}k_y a\right)\cos\left(\frac{3}{2}k_x a\right), \end{aligned} \tag{6}$$

where the plus sign refers to the upper π^* conduction band and the minus sign refers to the lower π valence band. The dispersion relation is symmetric about $E = 0$ when $t' = 0$. The band structure of graphene Eq. (6) is plotted in Fig. 3 with non-zero t and t'.

Also plotted in Fig. 3 is a close-up view of the band structure near one of the corners of the Brillouin zone. The dispersion in this region is obtained [174] by expanding the general band structure relation of Eq. (6) close to the K or K' point.

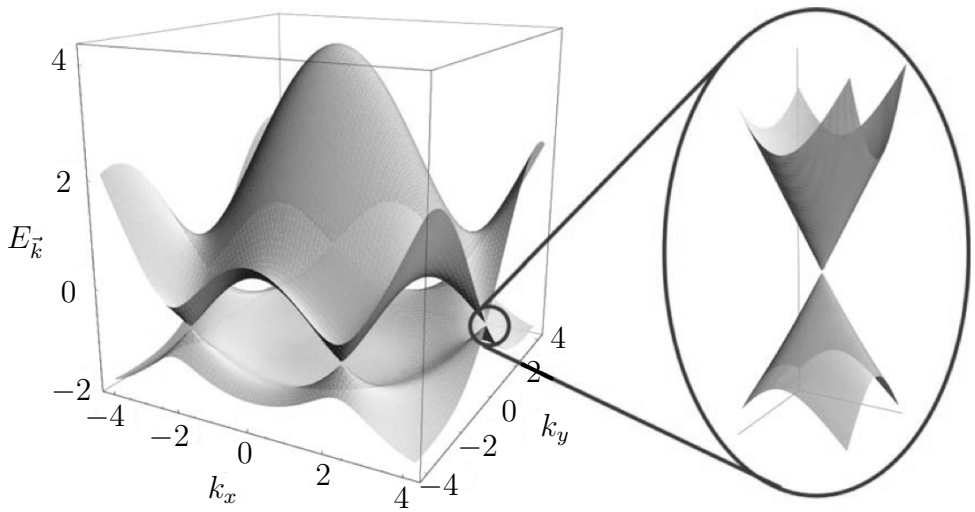

Figure 3: Electronic dispersion relation $E_{\vec{k}}$ for monolayer graphene, plotted in units of t with $t = 2.7$ eV and $t' = -0.2t$ eV. The spectrum is linear in the neighborhoods of the six corners of the hexagonal Brillouin zone. One such region is magnified to the right of the plot. All but two of these corners, known as the K and K' points, are equivalent and can be connected by reciprocal lattice vectors. (Adapted from Castro Neto *et al.* [42])

Writing $\vec{k} = \vec{K} + \vec{q}$ with $|\vec{q}| \ll |\vec{K}|$, we find

$$E_{\pm}(\vec{q}) \approx 3t' \pm v_{\mathrm{F}}|\vec{q}| - \left(\frac{9t'a^2}{4} \pm \frac{3ta^2}{8}\sin 3\theta_q\right)|\vec{q}|^2$$
$$\theta_q = \arctan\left(q_y/q_x\right), \tag{7}$$

where $v_{\mathrm{F}} = 3ta/2 \approx 3 \times 10^8$ cm/s is the Fermi velocity and θ_q is the angle in momentum space (recall that we have assumed $\hbar = 1$). Hence, up to second order in q/K, the dispersion near the Dirac points is rotationally symmetric in momentum space. We further note that the effect of non-zero t' shifts the location of the Dirac point in energy and breaks the electron-hole symmetry, making the π^* and π bands asymmetric. The π^* and π bands meet at the Dirac points, and the spectrum is gapless, leading to many interesting transport properties.

Typically, the next nearest neighbor terms in the tight-binding Hamiltonian are neglected by setting $t' = 0$ in this long wavelength regime, and the band structure for electrons with small momentum q compared to K or K' is given in the low carrier

regime by

$$E_{\pm}(\vec{q}) \approx \pm v_{\mathrm{F}}|\vec{q}| + \mathcal{O}\left((q/K)^2\right). \tag{8}$$

The linear dispersion relation Eq. (8) predicts a velocity that is independent of energy. This is in contrast to the case of quadratic dispersion in normal metals, where $E = q^2/(2m)$ implies that $v = q/m = \sqrt{2E/m}$. While the presence of charge carriers may cause a many-body renormalization of the carrier velocity, this effect is typically small in graphene monolayers, and we neglect it throughout this thesis.

The linear dispersion relation Eq. (8) causes the conduction and valence bands to intersect at the K and K' points, $q = 0$. Graphene is then a zero band-gap semiconductor with linear long wavelength dispersion for electrons and holes. The existence of two inequivalent points K and K' where these bands meet leads to a *valley degeneracy* of $g_v = 2$ for graphene. While processes that lead to inter-valley scatting can lift this degeneracy, such effects are beyond the scope of this thesis.

2.2 Massless Dirac fermions

In the long wavelength regime with $t' = 0$, graphene has a linear band structure described by Eq. (8) that resembles the energy of ultra-relativistic quantum mechanical particles described by a massless Dirac equation. For this reason, the K and K' points, where the conductance and valence bands meet, are known as Dirac points. In this section, we explore this analogy, concluding with the model Hamiltonian used throughout this thesis.

We begin by Fourier transforming the operators in the Hamiltonian of Eq. (5) so that, for example,

$$a_n = \frac{1}{\sqrt{N}} \sum_k e^{-i\vec{k}\cdot\vec{R}_n} a(\vec{k}), \tag{9}$$

where N is the number of unit cells in the graphene lattice. For low energy excitations,

this Fourier sum can be expanded around each of the Dirac points K and K', obtaining

$$\begin{aligned} a_n &\approx e^{-i\vec{K}\cdot\vec{R}_n} a_{K,n} + e^{-i\vec{K}'\cdot\vec{R}_n} a_{K',n} \\ b_n &\approx e^{-i\vec{K}\cdot\vec{R}_n} b_{K,n} + e^{-i\vec{K}'\cdot\vec{R}_n} b_{K',n} \,. \end{aligned} \tag{10}$$

Assuming that the fields $a_{K(K'),n}$ and $b_{K(K'),n}$ vary slowly over the length of the unit cell, it can be shown [151] by acting on these operators with the tight-binding Hamiltonian Eq. (5) that the long wavelength, low energy Hamiltonian for spin-less carriers near the Dirac points is given by

$$H = -iv_{\mathrm{F}} \int dx\, dy \left[\hat{\Psi}^{\dagger}_{K}(\vec{r}) \vec{\sigma} \cdot \vec{\nabla} \hat{\Psi}_{K}(\vec{r}) + \hat{\Psi}^{\dagger}_{K'}(\vec{r}) \vec{\sigma}^{*} \cdot \vec{\nabla} \hat{\Psi}_{K'}(\vec{r}) \right], \tag{11}$$

where $\vec{\sigma} = (\sigma_x, \sigma_y)$, $\vec{\sigma}^{*} = (\sigma_x, -\sigma_y)$ and $\hat{\Psi}^{\dagger}_{i} = (a^{\dagger}_{i}, b^{\dagger}_{i})$. The Hamiltonian Eq. (11) consists of two copies of the massless Dirac Hamiltonian describing momenta $\vec{p}$ near the K and K' points. In first quantized notation, which we use throughout this thesis, the two component free particle electron wave function $\psi(\vec{r})$ near the K point satisfies the two dimensional massless Dirac equation

$$H\psi(\vec{r}) = v_{\mathrm{F}} \vec{\sigma} \cdot \vec{p} \psi(\vec{r}) = E\psi(\vec{r}) \,, \tag{12}$$

where $\vec{p} = -i\vec{\nabla}$ is the momentum operator.

While the Hamiltonian Eq. (12) and its linear dispersion Eq. (8) arise from a tight binding model for a hexagonal carbon lattice Eq. (5), they describe massless two dimensional Dirac fermions, with pseudospin playing the role of spin in normal relativistic quantum systems. While quasiparticles in graphene can also have spin, Eq. (12) does not account for this effect, and it is not relevant to this thesis. Further details of the connection between the long wavelength Hamiltonian in graphene and the massless Dirac equation are discussed by Semenoff. [151]

Despite the relatively low carrier speed $v_{\mathrm{F}} \sim c/300$, quasiparticles in graphene obey a relativistic-like Dirac equation and are described by spinors. This spinor structure is responsible for many of the unique transport properties in graphene, and

its origin is in the A-B sublattice structure of graphene. The two equivalent but independent sublattices lead to chirality and the existence of a pseudospin quantum number, which is analogous to, but not the same as, spin. As a consequence of the lattice structure, carriers in graphene have spin, orbital and pseudospin quantum numbers. The intrinsic coupling between the orbital motion and the pseudospin is responsible for the correspondence between charge carrier transport in graphene and the massless Dirac equation. [51]

2.3 Cyclotron mass, wave functions and helicity

One important consequence of linear dispersion is a cyclotron mass that depends on the square root of the carrier density. This is in contrast to conventional metals with quadratic dispersion, for which the cyclotron mass is a constant. In the semi-classical approximation, the cyclotron mass m^* is given by [9]

$$m^* = \frac{1}{2\pi}\left[\frac{\partial A(E)}{\partial E}\right]_{E=E_{\mathrm{F}}}, \tag{13}$$

where $A(E)$ is the area in momentum space enclosed by the orbit and E_{F} is the Fermi energy. In graphene, the area for an orbit of energy E is

$$A(E) = \pi q^2(E) = \pi\frac{E^2}{v_{\mathrm{F}}^2}, \tag{14}$$

and hence $m^* = E_{\mathrm{F}}/v_{\mathrm{F}}^2 = k_{\mathrm{F}}/v_{\mathrm{F}}$. The density is given by $n = k_{\mathrm{F}}^2/\pi$, and the cyclotron mass for graphene is found to be

$$m^* = \frac{\sqrt{\pi}}{v_{\mathrm{F}}}\sqrt{n}. \tag{15}$$

The experimental verification of the square root dependence of the cyclotron mass on the density provides evidence for the existence of massless Dirac quasiparticles in graphene. Furthermore, fits to experimental data provide measurements of the Fermi velocity v_{F} and nearest neighbor hopping energy t. [57, 122, 83]

In momentum space with $\hbar = 1$, Eq. (12) takes the form

$$H_K = v_{\rm F}\vec{\sigma}\cdot\vec{q}$$
$$H_{K'} = v_{\rm F}\vec{\sigma}^*\cdot\vec{q}, \tag{16}$$

for momentum $\vec{k} = \vec{q} + \vec{K}$ around the K point or momentum $\vec{k} = \vec{q} + \vec{K}'$ around the K' point. The corresponding eigenfunctions with energy $E_\pm(|\vec{q}|) = \pm v_{\rm F}|\vec{q}|$ are given by

$$\psi_{\pm,K}(\vec{q}) = \frac{1}{\sqrt{2}}\begin{pmatrix} e^{-i\theta_q/2} \\ \pm e^{i\theta_q/2}\end{pmatrix};\quad \psi_{\pm,K'}(\vec{q}) = \frac{1}{\sqrt{2}}\begin{pmatrix} e^{i\theta_q/2} \\ \pm e^{-i\theta_q/2}\end{pmatrix}, \tag{17}$$

where $\theta_q = \arctan(q_y/q_x)$ is the angle in momentum space, as in Eq. (7). The wave functions Eq. (17) change sign when θ_q is increased by 2π and hence possess a Berry's phase of π, [122, 184, 21] a characteristic of spinors.

The pseudospin structure of graphene has important consequences for charge carriers. To illustrate this point, we define a helicity operator $\hat{h}$ as the projection of the momentum along the pseudospin direction:

$$\hat{h} = \frac{1}{2}\vec{\sigma}\cdot\frac{\vec{p}}{|\vec{p}|}. \tag{18}$$

Since the helicity operator is proportional to the Hamiltonian Eq. (16), we have

$$\hat{h}\psi_{\pm,K}(\vec{r}) = \pm\frac{1}{2}\psi_{\pm,K}(\vec{r})$$
$$\hat{h}\psi_{\pm,K'}(\vec{r}) = \mp\frac{1}{2}\psi_{\pm,K'}(\vec{r}). \tag{19}$$

Hence, electron (hole) states near the Dirac points in graphene have well defined positive (negative) helicity, and the eigenvalues of the pseudospin $\vec{\sigma}$ are aligned either with or against the momentum $\vec{p}$. The helicity eigenvalue is a good quantum number whenever the Hamiltonians Eq. (16) apply. It is not a good quantum number at large energy or for non-vanishing next nearest neighbor hopping energy ($t' \neq 0$).

In summary, electron and hole quasiparticle states near the K and K' points of graphene obey a massless Dirac-like equation as in Eq. (12). The massless Dirac

fermion states obey a dispersion relation that is linear in the momentum. The wave functions for these states have a pseudospin structure, independent of the spin structure, with the conduction and valence bands characterized by well defined helicity. These properties lead to interesting physics for the charge carriers on graphene, including zitterbewegung, [81, 85] ballistic transport over large distances, [121] unique magnetic properties [74, 133] including an anomalous fractional quantum Hall effect [122, 123] and an insensitivity to external electric potentials, an effect known as Klein tunneling. [89, 40] Reviews of the unique electronic properties of graphene are found in Refs. [42] and [51].

2.4 Klein tunneling

Low energy charge carriers in graphene display an insensitivity to potential barriers. [87, 86, 76, 79, 97, 127, 178] In classical mechanics, a particle with energy E will be confined by an electrostatic potential barrier of height greater than E. Nonrelativistic quantum mechanical particles can tunnel through such barriers, but the transmission probability is exponentially damped with increasing barrier height and width. For Dirac particles, such as the low energy electronic states near the K and K' points of graphene, the transmission probability depends only weakly on barrier height and may approach unity with increasing height. This effect, known as Klein tunneling, [89] leads to transport physics not seen in conventional semiconductor systems.

The origin of this paradoxical tunneling in graphene is the Dirac-like Hamiltonian Eq. (12), which allows solutions for a charge neutrality (Dirac) point separating positive (electron) and negative (hole) energy states. [42] While a square potential barrier with potential greater than this energy is repulsive to electrons, it is attractive to holes. Electron states on one side of the barrier can then match with hole states on

the other side, allowing for tunneling with little damping. As the height of the potential barrier increases, the transmission probability increases, and the transmission is perfect for normal incidence. [46, 107, 87]

Klein tunneling for low energy states in graphene can also be viewed as a consequence of pseudospin helicity. As considered in the previous section, electron and hole states in graphene are characterized by a well defined helicity, caused by the A-B sublattice structure. As the barrier potential has no off-diagonal pseudospin matrix elements, the incoming and reflected states would have opposite helicity for normal incidence, leading to a reflection probability of zero. The transmission probability for non-normal incidence depends on the potential profile along the barrier, with slowly varying barriers leading to increased reflection. [46] For a perfectly sharp, square barrier, the transmission probability can be determined from pseudospin conservation, with the result $T = \cos^2\theta$ for a particle incident at angle θ.

Since many of the calculations presented in this thesis relate directly to the formalism of Klein tunneling, we present a brief quantitative description. Consider a low energy particle traveling in the $+\hat{x}$ direction with energy E and momentum $\vec{q}$ (relative to the K point) incident from the left on on a barrier of height V_0 and width L, as in Fig. 4. Using a gauge transformation, the plane wave solutions Eq. (17) to the Dirac equation can be written in the form

$$\psi_{\vec{q}}(\vec{r}) = \frac{1}{\sqrt{2}} \begin{pmatrix} 1 \\ \pm e^{i\theta_q} \end{pmatrix} e^{i\vec{q}\cdot\vec{r}}, \tag{20}$$

where θ_q is the angle in momentum space. The wave functions to the left and right of the potential barrier, in regions labelled I and III, respectively, the wave function

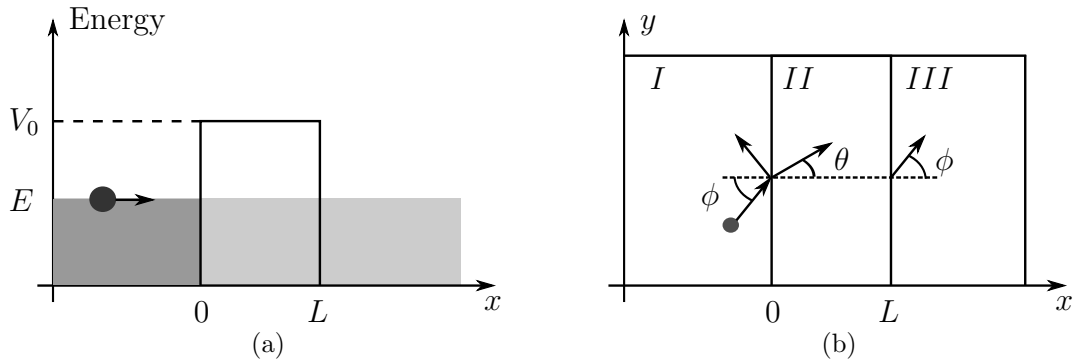

Figure 4: (a) A particle with energy E is incident on a potential barrier of height V_0 and width L. Classical trajectories are confined to the region to the left of the potential, marked with a dark gray rectangle. Quantum mechanical particles can tunnel through the potential barrier and be transmitted, but the transmission is exponentially damped with increasing potential height or width. Particles obeying a Dirac equation tunnel easily through such barriers, with a probability increasing to unity for normal incidence. (b) Overhead view of a massless Dirac fermion incident on a potential barrier in graphene. The particle has the wave function $\psi_{\rm I}$ left of the potential and an incident angle of ϕ with respect to the horizontal. The wave function is $\psi_{\rm II}$ within the potential barrier region, where the trajectory is at angle θ. To the right of the barrier, the wave function is given by $\psi_{\rm III}$ with angle ϕ. (Adapted from Castro Neto *et al.* [42])

takes the form

$$\psi_{\rm I}(\vec{r}) = \frac{1}{\sqrt{2}} \begin{pmatrix} 1 \\ se^{i\phi} \end{pmatrix} e^{i(q_x x + q_y y)} + \frac{r}{\sqrt{2}} \begin{pmatrix} 1 \\ se^{i(\pi-\phi)} \end{pmatrix} e^{i(q_y y - q_x x)}$$

$$\psi_{\rm III}(\vec{r}) = \frac{t}{\sqrt{2}} \begin{pmatrix} 1 \\ se^{i\phi} \end{pmatrix} e^{i(q_x x + q_y y)}, \tag{21}$$

where $\phi = \arctan(q_y/q_x)$, $q_x = k_{\rm F}\cos\phi$, $q_y = k_{\rm F}\sin\phi$ and $k_{\rm F}$ is the Fermi momentum.

Similarly, the wave function within the potential barrier, region II, is given by

$$\psi_{\rm II}(\vec{r}) = \frac{a}{\sqrt{2}} \begin{pmatrix} 1 \\ s'e^{i\theta} \end{pmatrix} e^{i(\tilde{q}_x x + q_y y)} + \frac{b}{\sqrt{2}} \begin{pmatrix} 1 \\ s'e^{i(\pi-\theta)} \end{pmatrix} e^{i(q_y y - \tilde{q}_x x)}, \tag{22}$$

where $\tilde{q}_x = \sqrt{(V_0 - E)^2/v_{\rm F}^2 - q_y^2}$ and $\theta = \arctan(q_y/\tilde{q}_x)$. The signs for the spinors are given by $s = \mathrm{sgn}(E)$ and $s' = \mathrm{sgn}(E - V_0)$.

The reflection and transmission amplitudes r and t, along with the coefficients a and b, are determined by enforcing continuity of the wave function at the boundaries between interfaces such that $\psi_{\rm I}(0,y) = \psi_{\rm II}(0,y)$ and $\psi_{\rm II}(L,y) = \psi_{\rm III}(L,y)$. It is not necessary to match the derivatives of the wave function, as with the regular Schrödinger equation, since the Dirac equation is a first order differential equation. The transmission probability $T = tt^*$ is found to be

$$T(\phi) = \frac{\cos^2\theta\cos^2\phi}{\left[\cos\left(\tilde{q}_x L\right)\cos\phi\cos\theta\right]^2 + \sin^2\left(\tilde{q}_x L\right)\left(1 - ss'\sin\phi\sin\theta\right)^2}. \tag{23}$$

The transmission probability Eq. (23) is unity, independent of ϕ, whenever $\tilde{q}_x L = n\pi$ where n is an integer. The transmission is also perfect for normal incidence $\phi = \theta = 0$, independent of the width of the barrier. The potential barrier becomes transparent in these situations, a manifestation of the Klein paradox for relativistic electrons. The transmission probability Eq. (23) simplifies in the limit $|V_0| \gg |E|$, [42] and we have

$$T(\phi) \simeq \frac{\cos^2\phi}{1 - \cos^2\left(\tilde{q}_x L\right)\sin^2\phi}. \tag{24}$$

In this case, there are multiple values of ϕ for which the barrier becomes transparent.

In general, magnetic fields or fluctuations in the electrostatic potential can break the lattice and time-reversal symmetries, altering the tunneling properties of graphene. This then breaks the valley symmetry, and the transmission becomes valley dependent. Such effects have led to an increased interest in "valleytronics," [166, 143] where the valley index of electrons is used to control the transmission properties, analogous to the manipulation of the spin quantum number in spintronics. [186] Such valley dependent effects are beyond the scope of this thesis.

We have shown that low energy electrons in graphene, incident on a rectangular potential barrier of arbitrary height and width, are perfectly transmitted for normal incidence when inter-valley scattering is neglected. This effect is a manifestation of the chiral nature of Dirac electrons in each valley, which suppresses backscattering. We

note that the result Eq. (23) allows for evanescent waves within the potential barrier region, which occur when $\tilde{q}_x$ is imaginary. Such modes are relevant to the transport when the chemical potential is close to the Dirac point, where the kinetic energy vanishes. In that case, the evanescent modes introduce additional scattering, altering the transmission probability. Transport through evanescent modes in graphene is the focus of this thesis, and the effect of such modes is introduced in Chp. 3.

CHAPTER III

NOISE IN MESOSCOPIC CONDUCTORS

In 1918, Walter Schottky studied the current fluctuations in vacuum tubes, finding [149] that the fluctuations persisted even after he had eliminated all then-known sources of noise. Schottky identified two distinct sources of noise in his experiments, which he called *Wärmeffekt*, now known as Johnson-Nyquist [84, 124] or thermal noise, and *Schroteffekt*, now known as shot noise. Thermal noise arises from thermal fluctuations in the motion of charge carriers, and is present in all conductors at non-zero temperature. Thermal noise is related to the conductance through the fluctuation-dissipation theorem, [124, 39] and hence provides no new information about the transport. Shot noise, in contrast, is caused by the discreteness of the charge carriers, and is not present in all conductors. Shot noise measurements yield information about the temporal correlations of the charge carriers, providing a useful tool for mesoscopic physics. Thorough reviews of thermal and shot noise can be found in Refs. [25] and [55].

3.1 Thermal noise

Thermal noise is a consequence of thermal fluctuations in the occupation numbers of the charge carriers in a conductor. This effect is always present at non-zero temperature. Schottky first identified thermal noise in 1918, [149] and John B. Johnson later observed it in 1928. [84] Johnson discussed his measurements with Harry Nyquist, his colleague at Bell Labs, who provided a theoretical explanation. [124]

Throughout this section, we consider the current of input and output states for various scattering situations. Rather than describing these states using Slater determinants, we use second quantization, ignoring electron-electron interactions. For

fermions in a conductor at temperature T, we introduce creation (annihilation) operators $\hat{a}^\dagger$ ($\hat{a}$), which obey the anti-commutation rule $\left\{\hat{a}, \hat{a}^\dagger\right\} = 1$.

Due to thermal fluctuations, the occupation number $n \equiv \hat{a}^\dagger \hat{a}$ is, on average, given by $\langle n \rangle = f(T)$ where f is the Fermi-Dirac distribution function

$$f = \frac{1}{e^{[(\epsilon-\mu)/k_B T]} + 1} \tag{25}$$

with energy ϵ, chemical potential μ and Boltzmann's constant k_B. States are occupied with probability f and unoccupied with probability $(1 - f)$. From the Pauli principle, we have $\left(\hat{a}^\dagger\right)^2 = 0$, and hence, using the anti-commutation relation, we find

$$n^2 = \hat{a}^\dagger \hat{a} \hat{a}^\dagger \hat{a} = \left(1 - \hat{a}\hat{a}^\dagger\right) \hat{a}^\dagger \hat{a} = n. \tag{26}$$

Noting this result, the mean squared deviation from the average is given by

$$\left\langle (\Delta n)^2 \right\rangle = f\left(1 - f\right), \tag{27}$$

where $\Delta n \equiv n - \langle n \rangle$. This fluctuation vanishes in the zero-temperature limit, when $f = 0, 1$. At high temperature, f is small such that $1 - f \approx 1$, and the fluctuations are determined by Maxwell-Boltzmann statistics.

Fluctuations in the occupation numbers of charge carriers lead to equilibrium current noise. Noise is described by its power spectral density $S(\omega)$, which is determined by the Fourier transform of the current-current correlation function [170, 52]

$$S(\omega) = \int_{-\infty}^{+\infty} e^{i\omega t} \langle \Delta I(t + t_0) \Delta I(t_0) \rangle \, dt, \tag{28}$$

where $\Delta I(t)$ is the time-dependent fluctuation in the current at voltage V and temperature T and $\langle \ldots \rangle$ denotes an average over the initial time t_0 or, equivalently, an ensemble average. For $\hbar\omega \ll k_B T$, the thermal noise is related to the conductance G by the fluctuation-dissipation theorem, [124, 39] with the result

$$S = 2 k_B T G. \tag{29}$$

Hence, a measurement of the thermal noise provides the same information as conductance measurements. Thermal noise affects all conductors in equilibrium with zero or non-zero voltage.

3.2 Shot noise

Shot noise is a non-equilibrium (transport) phenomenon caused by the discrete nature of charge carriers. It is seen in systems where the number of particles is small enough that the random deviations in their motion become significant. For example, the measured current of electrons in mesoscopic devices (or photons in quantum optical systems) fluctuates as a consequence of the stochastic processes that determine their arrival times at the detector. Unlike thermal noise, shot noise is present at zero temperature and can provide information about temporal correlations that conductance measurements alone cannot.

Shot noise is a useful diagnostic tool for studying correlations in many electrical and optical systems. It has been studied extensively in graphitic systems [125, 167, 114, 146, 156, 50, 102, 59, 142, 150, 43, 70, 177] and also in other mesoscopic systems such as tunnel barriers, [106, 94, 49, 140, 141, 148, 23, 96] quantum point contacts, [4, 171, 175, 69, 36, 48, 95, 103, 58, 105, 138, 90, 147, 169, 33] resonant tunnel barriers [47, 10, 137, 136] and quantum wells. [165, 44, 53] When the number of particles becomes large, the noise-to-signal ratio becomes small, and other sources of noise dominate the transport statistics.

In electrical circuits, shot noise is significant when the current is small or the time scale is short. For devices where electrons are transmitted randomly and independently with small probability, the number of transmitted charges Q in a time interval Δt is described by Poissonian statistics. With average particle number current $\bar{i}$, the mean number of events in the interval Δt is given by $\bar{i}\Delta t$, and the probability

distribution is

$$P(Q) = \frac{(\bar{i}\Delta t)^Q}{Q!} e^{-\bar{i}\Delta t}. \tag{30}$$

Poissonian devices include tunnel junctions, Schottky barrier diodes, p-n junctions and thermionic vacuum diodes. [52] For Poisson processes, the shot noise has the value

$$S = e\langle I \rangle \equiv S_{\text{poisson}} \tag{31}$$

at zero frequency and temperature.

This shot noise value is the maximum value for systems of non-interacting electrons. In general, electron correlations suppress the low frequency shot noise below the Poisson value. For example, macroscopic metallic systems have zero shot noise because inelastic electron-phonon interactions cause the current fluctuations to average out. [55] Graphene is also known to exhibit non-zero shot noise below the Poisson limit, as discussed in Sec. 3.3 and later chapters.

3.2.1 Single particle shot noise

Before presenting a scattering theory approach to calculating the shot noise, we consider an instructive thought experiment for single particle shot noise. [25] First, consider a single particle incident from the left on a barrier with transmission probability T (not to be confused with temperature, which we ignore for now) and reflection probability $R = 1 - T$. As in the previous section, we introduce creation, annihilation and number operators for the incident ($\hat{a}_{\text{in}}$), transmitted ($\hat{a}_T$) and reflected ($\hat{a}_R$) beams. The incident beam is populated with probability n_{in}, and the transmitted (reflected) beam is populated with probability $n_{T(R)}$. The experiment can be repeated many times, resulting in statistics for these occupation numbers.

In this example, we assume $n_{\text{in}} = 1$, and hence $\Delta n_{\text{in}} = 0$. Since the transmitted beam is occupied with probability T and unoccupied with probability R, we have $\langle n_T \rangle = T$ and $\langle n_R \rangle = R$. The fluctuations in the outgoing beam follow from $n_R^2 = n_R$

as in Eq. (26), which implies

$$\langle (\Delta n_R)^2 \rangle = \langle n_R^2 \rangle - \langle n_R \rangle^2 = \langle n_R \rangle \left(1 - \langle n_R \rangle\right) = TR. \tag{32}$$

Equation (26) is also valid for n_T, and we find $\langle (\Delta n_T)^2 \rangle = T(1-T) = TR$. This noise is known as *partition noise*, because it divides the incoming beam into two streams. The partition noise vanishes when the transmission or reflection is perfect, and it is maximal for $T = 1/2$. Since the particle is always either reflected or transmitted, we have $n_T n_R = 0$, and hence

$$\begin{aligned} \langle \Delta n_T \Delta n_R \rangle &= \langle \left(n_T - \langle n_T \rangle\right) \left(n_R - \langle n_R \rangle\right) \rangle \\ &= -\langle n_T \rangle \langle n_R \rangle = -TR. \end{aligned} \tag{33}$$

Suppose that we repeat the same experiment, allowing for thermal fluctuations in the incoming beam. The incoming state is occupied with probability f and unoccupied with probability $1 - f$, where f is the Fermi-Dirac distribution function. Hence, we have $\langle n_{\rm in} \rangle = f$, from which $\langle n_T \rangle = fT$ and $\langle n_R \rangle = fR$. Repeating the above calculation, where again $n_T n_R = 0$, the fluctuations in the beams are found to be

$$\begin{aligned} \langle (\Delta n_T)^2 \rangle &= Tf(1 - Tf) \\ \langle (\Delta n_R)^2 \rangle &= Rf(1 - Rf) \\ \langle \Delta n_T \Delta n_R \rangle &= -TRf^2. \end{aligned} \tag{34}$$

In this case, the fluctuations in the transmitted beam do not vanish in the limit $T = 1$, instead fluctuating like the incoming beam. When either $T \ll 1$ or $\langle n_{\rm in} \rangle \ll 1$, the factor $1 - Tf$ can be replaced by one. In the zero temperature limit, $f = 1$ and we recover the results from the previous thought experiment.

In mesoscopic conductors, the current is carried by many indistinguishable particles. The results derived above can be related to the shot noise in a conductor [25] by considering a system where ideal conductors guide the incident, transmitted and

reflected electrons to and from the mesoscopic system at various energies. In a non-interacting conductor, we may think of the current at different energies as separate and determined by independent occupation numbers $n(E)$. We consider electrons incident from one direction with a velocity $v(E)$ that depends only on the energy E. Within an energy interval dE, the incident current is given by $dI_{\rm in}(E) = en(E)v(E)d\rho(E)$ where $d\rho(E)$ is the electron density per unit length in this energy range. Using the density of states in the ideal conductors $\nu(E) \equiv d\rho/dE = [hv(E)]^{-1}$, the average incident, transmitted and reflected currents are given in this picture by

$$\begin{aligned}
\langle I_{\rm in}\rangle &= \frac{e}{h}\int f(E)dE \\
\langle I_T\rangle &= \frac{e}{h}\int f(E)TdE \\
\langle I_R\rangle &= \frac{e}{h}\int f(E)RdE.
\end{aligned} \tag{35}$$

The current noise, as the fluctuation of a collection of independent stochastic processes, is also given by a sum of the variances of the currents carried at individual energies. In the zero frequency limit, the current noise power is given by $S_{II} = (e^2/h)\int\langle\Delta n\Delta n\rangle dE$, and hence

$$\begin{aligned}
S_{I_{\rm in}I_{\rm in}} &= \frac{e^2}{h}\int f(1-f)dE \\
S_{I_TI_T} &= \frac{e^2}{h}\int Tf(1-Tf)dE \\
S_{I_RI_R} &= \frac{e^2}{h}\int Rf(1-Rf)dE.
\end{aligned} \tag{36}$$

In this case, the transmitted and reflected beams are correlated

$$S_{I_TI_R} = -\frac{e^2}{h}\int TfRfdE. \tag{37}$$

If either $T \ll 1$ or $f \ll 1$, the factor $1-Tf$ can be replaced by one. Since the average current is $\langle I\rangle = (e/h)\int TfdE$, this limit corresponds to the maximal Schottky result for the shot noise, [149] $S_{I_TI_T} = e\langle I\rangle$, the same result as for a Poisson process Eq. (31).

In general, the factor $1 - Tf \leq 1$ ensures that the shot noise is less than or equal to the Poisson value for systems of non-interacting fermions.

For ballistic systems with $T = 1$, the noise Eq. (36) vanishes in the zero temperature limit. As the temperature increases, thermal fluctuations in the incoming beam increase the noise. At high temperatures, $f \ll 1$, and the noise is given by the Poisson value, which is also achieved for $T \ll 1$. The noise result of Eq. (36) includes the effects of both the fluctuations in the incident beam due to thermal motion and the partition noise due to the discrete nature of the charge carriers. In order to separate the two contributions, the shot noise is usually defined as the zero temperature noise.

These thought experiments provide a basic physical description of the shot noise in mesoscopic devices, including both thermal fluctuations and partition noise caused by the reflected and transmitted waves. The maximum shot noise value for non-interacting fermion systems, such as those considered in this thesis, is that of a Poisson process, and is proportional to the average current. In general, electron interactions such as the Pauli exclusion principle or the Coulomb interaction cause the shot noise to deviate from the Poisson value. For this reason, shot noise is a useful quantity for studying correlations in mesoscopic systems.

While these thought experiments provide a qualitative description of the shot noise in mesoscopic conductors, quantitative analysis requires a detailed quantum mechanical calculation involving the wave functions. In the next section, we summarize [25, 55] a calculation of the shot noise based on the scattering formalism, resulting in the two-terminal Landauer formula for the conductance and shot noise. [91, 37, 38]

3.2.2 The two-terminal Landauer-Büttiker formula

In 1957, Rolf Landauer published [91] an analysis of electrical conduction based on the scattering formalism. He viewed the non-interacting mesoscopic system as a scattering region, connected by ideal leads to electron reservoirs in thermal equilibrium. The

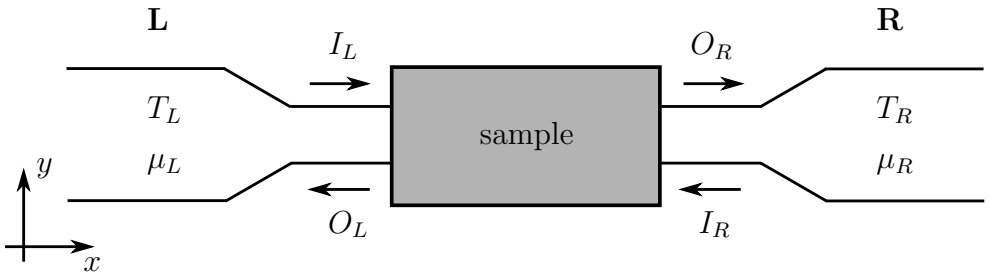

Figure 5: A two-terminal scattering system in which a mesoscopic sample is connected to two reservoirs labelled **L** and **R**. Both reservoirs are in thermal equilibrium, and reservoir $i = \{L, R\}$, at temperature T_i with chemical potential μ_i, has incoming (outgoing) state wave functions I_i (O_i). (Adapted from Blanter and Büttiker [25])

incoming states are populated according to Fermi-Dirac statistics and scattered into outgoing states, as in the thought experiments of the previous section. Landauer showed that the conductance for low temperatures is determined by the transmission matrix at the Fermi level. This surprisingly simple result is an important concept in mesoscopic physics, and the two-terminal Landauer formula [63, 80] and its multi-terminal generalization [34, 35, 162, 12, 153] have been studied extensively [88, 92, 98, 182, 37, 38, 93]

In Fig. 5, a mesoscopic sample is connected to electron reservoirs L and R. The left reservoir has temperature T_L and chemical potential μ_L, and the right reservoir has temperature T_R and chemical potential μ_R. Both reservoirs are in thermal equilibrium, and we denote the one-dimensional incoming (outgoing) state wave functions for reservoir $i = \{L, R\}$ by I_i (O_i). We assume one-dimensional currents along the $+\hat{x}$ direction. For notational simplicity, we assume that each lead has an equal number N of incoming and outgoing modes at energy ϵ. While this symmetry is not required for the derivation of the Landauer formula, the key results in this thesis are derived in the continuum limit, where $N \gg 1$.

With an equal number of modes in each reservoir, the incoming and outgoing

states are related by the $2N \times 2N$ dimensional *scattering matrix* S:

$$\begin{pmatrix} \vec{O}_L \\ \vec{O}_R \end{pmatrix} = S \begin{pmatrix} \vec{I}_L \\ \vec{I}_R \end{pmatrix}. \tag{38}$$

The scattering matrix can be written in terms of the $N \times N$ transmission and reflection matrices

$$S \equiv \begin{pmatrix} s_{11} & s_{12} \\ s_{21} & s_{22} \end{pmatrix} = \begin{pmatrix} r & t' \\ t & r' \end{pmatrix}, \tag{39}$$

where the matrix s_{bn} contains amplitudes $s_{bn,am}$ describing scattering from incoming mode m in lead $a = \{L, R\}$ to outgoing mode n in lead $b = \{R, L\}$. The matrices $r(r')$ and $t(t')$ describe the reflection and transmission of states incoming from the left (right). Flux conservation implies that the scattering matrix it unitary, and it is also symmetric for systems with time reversal symmetry.

Alternatively, the relationship between incoming and outgoing states on the left and right of the scattering region can be written in terms of the *transfer matrix* M where

$$\begin{pmatrix} \vec{O}_R \\ \vec{I}_R \end{pmatrix} = M \begin{pmatrix} \vec{I}_L \\ \vec{O}_L \end{pmatrix}, \quad M \equiv \begin{pmatrix} \left(t^\dagger\right)^{-1} & r' \left(t'\right)^{-1} \\ -\left(t'\right)^{-1} r & \left(t'\right)^{-1} \end{pmatrix}. \tag{40}$$

The transfer matrix obeys the composition rule $M(x, y) = M(x, z)M(z, y)$, convenient for systems that can be partitioned into subsystems with known transmission and reflection matrices. It also satisfies the identity $M(x, x) = \mathbb{I}$ (here $\mathbb{I}$ is the $2N \times 2N$ identity matrix) and the current conservation rule $M\sigma_z M^\dagger = \sigma_z$. Many theoretical transport studies on graphene use the transfer matrix, [146, 85, 167, 163, 164, 46] and some of the results presented in this thesis rely on its convenient composition rule.

In second quantization, the current operator in lead L is given by

$$\hat{I}(t) = \frac{e}{h} \sum_{\alpha,\beta} \int_{-\infty}^{\infty} d\epsilon \int_{-\infty}^{\infty} d\epsilon' I_{\alpha\beta}(\epsilon, \epsilon') \hat{a}_\alpha(\epsilon) \hat{a}_\beta(\epsilon') e^{it(\epsilon - \epsilon')/\hbar}, \tag{41}$$

where $\hat{a}^\dagger_\alpha(\epsilon)$ and $\hat{a}_\alpha(\epsilon)$ are the creation and annihilation operators for the scattering state $\psi_\alpha(\vec{r}, \epsilon)$ and $\alpha = (a, m)$ and $\beta = (b, n)$ are composite indices. The matrix

element $I_{\alpha\beta}(\epsilon,\epsilon')$ is determined by the current passing through a cross section Σ_L of lead L. In terms of the wave functions, the matrix elements are given by

$$I_{\alpha\beta}(\epsilon,\epsilon') = \frac{1}{2}\int_{\Sigma_L} dy \left\{\psi_\alpha(\vec{r},\epsilon)\left[\hat{v}_x\psi_\beta(\vec{r},\epsilon')\right]^* + \psi^*_\beta(\vec{r},\epsilon')\hat{v}_x\psi_\alpha(\vec{r},\epsilon)\right\}, \tag{42}$$

where $\hat{v}_x$ is the operator for the x-component of the velocity and $\vec{r} = (x,y)$.

This matrix element simplifies at equal energies according to

$$I_{am,bn}(\epsilon,\epsilon) = \delta_{aL}\delta_{ab}\delta_{mn} - \sum_{p=1}^{N} s_{Lp,am}(\epsilon)s^*_{Lp,bn}(\epsilon). \tag{43}$$

Noting this result, and that $\langle \hat{a}^\dagger_\alpha(\epsilon)\hat{a}_\beta(\epsilon')\rangle = \delta_{\alpha\beta}\delta(\epsilon-\epsilon')f_a(\epsilon)$, where f_a is the Fermi-Dirac distribution in lead a, the average current in lead L reduces to

$$\begin{aligned}\langle \hat{I}(t)\rangle &= \frac{e}{h}\sum_\alpha \int_{-\infty}^{\infty} d\epsilon f_a(\epsilon) I_{\alpha\alpha}(\epsilon) \\ &= \frac{e}{h}\int_{-\infty}^{\infty} d\epsilon \left[f_L(\epsilon) - f_R(\epsilon)\right] \mathrm{Tr}\left(t(\epsilon)t^\dagger(\epsilon)\right),\end{aligned} \tag{44}$$

where we have used the unitarity of the scattering matrix. The distribution functions in the leads are

$$\begin{aligned} f_L(\epsilon) &= f(\epsilon - E_F - eV) \\ f_R(\epsilon) &= f(\epsilon - E_F) \\ f(\xi) &= \left[1 + \exp\left(\xi/k_BT\right)\right]^{-1}, \end{aligned} \tag{45}$$

where E_F is the Fermi energy and V is the electrochemical potential difference between the two reservoirs.

The conductance $G \equiv \lim_{V\to 0}\langle I\rangle/V$ is

$$G = \frac{e^2}{h}\int_{-\infty}^{\infty} d\epsilon \left(-\frac{\partial f}{\partial \epsilon}\right) \mathrm{Tr}\, tt^\dagger, \tag{46}$$

which simples to the Landauer formula

$$G = \frac{e^2}{h}\,\mathrm{Tr}\, tt^\dagger = \frac{e^2}{h}\sum_{n=1}^{N} T_n, \tag{47}$$

where $0 \leq T_n \leq 1$ are the eigenvalues of $tt^\dagger$, which is evaluated at the Fermi level. Surprisingly, the calculation of the conductance does not require knowledge of the eigenvectors, which can be complicated linear combinations of the incoming states.

The noise is found by substituting the current operator Eq. (41) into the noise power Eq. (28). The relation [38]

$$\langle \hat{a}_1^\dagger \hat{a}_2 \hat{a}_3^\dagger \hat{a}_4 \rangle - \langle \hat{a}_1^\dagger \hat{a}_2 \rangle \langle \hat{a}_3^\dagger \hat{a}_4 \rangle = \delta_{14}\delta_{23} f_1(1 - f_2) \equiv \Delta_{1234} \tag{48}$$

shows that there are no cross correlations between different incoming states. In Eq. (48), we have used shorthand notation where, for example, $\delta_{14} = \delta_{\alpha\gamma}\delta(\epsilon - \epsilon''')$ with $\alpha = (a, m)$ and $\gamma = (g, p)$ referring to lead $a(g)$ with mode index $m(p)$. In the zero frequency limit, the noise power of current fluctuations for spin-less particles is given by

$$S = \frac{e^2}{h} \int_0^\infty d\epsilon \left\{ \left[f_L \left(1 \mp f_L\right) + f_R \left(1 \mp f_R\right) \right] \mathrm{Tr}\left(tt^\dagger\right) \pm \left(f_L - f_R\right)^2 \mathrm{Tr}\left[tt^\dagger \left(1 - tt^\dagger\right) \right] \right\}, \tag{49}$$

where the upper (lower) sign refers to fermions (bosons). The first two terms, proportional to $\mathrm{Tr}\left(tt^\dagger\right)$, are the equilibrium contribution to the noise, while the third term, proportional to $\mathrm{Tr}\left[tt^\dagger\left(1 - tt^\dagger\right)\right]$, represents the non-equilibrium noise. The non-equilibrium noise is second order in the distribution functions, and can be neglected compared to the equilibrium noise at high temperatures where the distributions are approximately Maxwell-Boltzmann functions. The shot noise term enhances the current noise power compared to the equilibrium noise for fermions and decreases it for bosons.

Assuming eV and $k_B T$ are small enough, we may neglect the energy dependence of the scattering matrix and evaluate the transmission matrix at the Fermi energy. In equilibrium ($V = 0$), we have $f_L = f_R$, and the non-equilibrium shot noise vanishes, giving a noise power

$$S = 2k_B T \frac{e^2}{h} \mathrm{Tr}\, tt^\dagger = 2k_B T \frac{e^2}{h} \sum_{n=1}^{N} T_n \tag{50}$$

for fermions, where we have used the relation $f(1-f) = -k_B T\,(\partial f/\partial\epsilon)$ for the Fermi-Dirac distribution function. As expected, this result is the Johnson-Nyquist noise Eq. (29). At zero temperature, the shot noise is

$$S = eV\frac{e^2}{h}\,\mathrm{Tr}\left[tt^\dagger\left(1-tt^\dagger\right)\right] = eV\frac{e^2}{h}\sum_{n=1}^{N} T_n\left(1-T_n\right). \tag{51}$$

This result, due to Büttiker, [37] is the multi-channel generalization of the single channel formulas presented in Refs. [88, 98] and [182]. As with the conductance Eq. (47), the shot noise only depends on the eigenvalues of the transmission matrix, a powerful result for mesoscopic systems. For non-zero temperature and non-zero voltage, the noise power is given by [38, 109]

$$S = \frac{e^2}{h}\left[2k_BT\sum_{n=1}^{N} T_n^2 + eV\coth\left(\frac{eV}{2k_BT}\right)\sum_{n=1}^{N} T_n\left(1-T_n\right)\right]. \tag{52}$$

According to Eq. (51), there is no contribution to the shot noise from open or closed channels with $T_n = 1, 0$. This is because there are no fluctuations in the incoming beam at zero temperature, and a perfectly transmitting or reflecting barrier does not partition the incoming states. As T_n decreases from unity, the transmitted electron stream begins to deviate from the average current. When $T_n \ll 1$, the shot noise reaches the Poisson value, the maximum for non-interacting particles.

Suppression of the shot noise below the Poisson value is an important feature of some mesoscopic systems. A common measure for the shot noise in mesoscopic systems is the Fano factor F, defined as the ratio of the shot noise power to the Poisson value Eq. (31). For energy independent transmission, the Fano factor is found from Eq. (47) and Eq. (51) as

$$F = \frac{\sum_{n=1}^{N} T_n\left(1-T_n\right)}{\sum_{n=1}^{N} T_n}. \tag{53}$$

The Fano factor is an important diagnostic quantity in mesoscopic physics, and it is the subject of the remainder of this thesis. For metallic diffusive wires, the transmission eigenvalues are bi-modally distributed, [161, 18] leading to an $F = 1/3$ suppression of the shot noise, [19, 115, 5, 119, 24, 104, 160, 77] the same value as in ballistic

graphene. [167, 50, 59] Ballistic quantum cavities also show exhibit sub-Poissonian shot noise, with a Fano factor $F = 1/4$. [11, 82, 130]

Before discussing the shot noise in graphene, we note that the equations derived in this section can be amended to include the effects of spin and valley degeneracy. Both the conductance and the shot noise will be enhanced proportionally to these degeneracy factors, so that the conductance and noise power can be measured in units of $G_0 \equiv$ (degeneracy factor) $\times e^2/h$ and $S_0 \equiv eVG_0$, respectively. The twofold spin and valley degeneracies increase the conductance and shot noise in graphene by $g_s g_v = 4$. The Fano factor, however, is not sensitive to these degeneracies. For this reason, and for notational simplicity, we omit all degeneracy factors throughout this thesis.

3.3 Shot noise on graphene

A priori, one might expect impurity-free graphene to exhibit zero shot noise at low temperatures, since the transport is ballistic. [121] This assumption proves false. Electrical transport near the Dirac point is dominated by evanescent modes that cause scattering, even in pristine graphene. This observation has stimulated many research efforts in shot noise on graphene, both theoretical [155, 146, 102, 156, 43, 142, 150, 70, 177] and experimental, [114, 59, 50] and it is the motivation for this thesis.

3.3.1 Theory

Tworzydło *et al.* [167] first predicted non-zero shot noise at the Dirac point of clean graphene in 2006, following an analysis of the conductance based on the Landauer formula by Katsnelson. [85] Tworzydło *et al.* showed that the Fano factor displays a maximum of $F = 1/3$ for zero concentration. Furthermore, this result is universal (geometry independent) for short, wide graphene strips. Despite the ballistic dynamics of graphene, this value for the Fano factor is the same obtained for a disordered

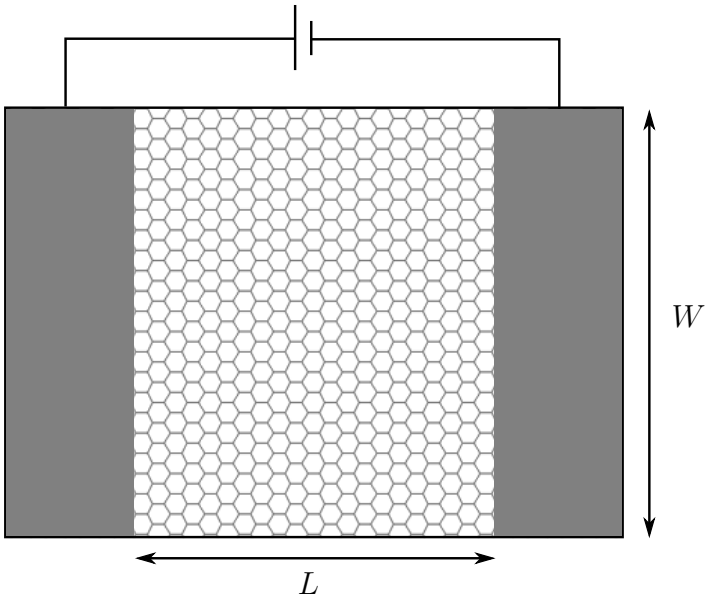

Figure 6: A graphene field effect transistor geometry, as considered by Tworzydło *et al.*, [167] consists of a sheet of graphene with length L and width W is contacted at either end by ideal leads (gray rectangles). A gate electrode (not shown) controls the potential in the central graphene region. (Adapted from Tworzydło *et al.* [167])

metal. [19, 115, 5, 119, 24, 104, 160, 77] This ambiguity is the topic of Chp. 4.

The graphene field effect transistor (FET) geometry considered by Tworzydło *et al.* consists of a sheet of clean graphene of length L and width W, contacted at either end by ideal leads, as in Fig. 6. A gate electrode controls the voltage in the central graphene region, tuning it to the Dirac point. The low energy conduction electrons in this geometry obey a Dirac Hamiltonian $H = v_{\mathrm{F}}\vec{\sigma}\cdot\vec{p} + V(x)$ as in Eq. (12). The leads are modeled using a large potential, such that all modes in the leads are propagating and none of the calculations depend on the chemical potential in the leads. In the central graphene region, a conduction electron with wave vector (k, q) has energy $\epsilon = V(x) + \hbar v_{\mathrm{F}}\sqrt{k^2 + q^2}$ and can be either propagating (real k) or evanescent (imaginary k). When the energy and potential are tuned to the Dirac point, the current is carried exclusively via evanescent waves.

Due to the translational symmetry in the y-direction, the transverse momentum q is a good quantum number everywhere in the FET. As considered for the case

of Klein tunneling in Sec. 2.4, the transmission probabilities T_n are determined by matching wave functions for each mode at the boundaries $x = 0, L$ between the leads and the undoped graphene. This matching is done analytically by choosing boundary conditions that do not mix modes at the interfaces. Physically, this is accomplished through either infinite mass confinement or the metallic or semiconducting armchair edge boundary conditions. When the number of modes in the graphene strip is large, the transmission probability for mode n at the Dirac point is given by [167]

$$T_n = \frac{1}{\cosh^2(q_n L)}. \tag{54}$$

The Fano factor follows in the Landauer picture from Eq. (53), with the result $F = 1/3$, independent of the boundary condition, when $W/L \gg 1$. Numerical calculations suggest this condition is met even for modest aspect ratios of $W/L \gtrsim 4$.

Away from the Dirac point, the transmission probability is

$$T_n = \left| \frac{k_n}{k_n \cos(k_n L) + i\,(\mu/\hbar v_{\mathrm{F}}) \sin(k_n L)} \right|^2, \tag{55}$$

where $k_n = \sqrt{(\mu/\hbar v_{\mathrm{F}})^2 - q_n^2}$ is the longitudinal wave number and μ is the chemical potential in the central graphene region. In this case, Tworzydło *et al.* calculate the Fano factor as a function of the chemical potential, finding that it reaches its maximum value $F = 1/3$ at the Dirac point. The Fano factor also shows oscillations with increasing chemical potential, a result of the increasing number of propagating modes introduced. It decays to $F \simeq 0.12$ as propagating modes begin to dominate the transport. These calculations are further supported by numerical simulations using a tight-binding model. [167] Sonin [156] has extended this calculation of the shot noise in the limit of infinite aspect ratio W/L. A dependence of the Fano factor on the chemical potential is not expected for diffusive transport, [102, 59] and its observation [50] provides indications of transport through evanescent modes in graphene.

Shot noise has also been examined theoretically in graphene in the presence of defects. First, San Jose *et al.* [146] considered smooth "charge puddle" disorder at low doping in one and two dimensions. Such disorder, which results in localized puddles of excess electron/hole accumulations, [87] can be caused by corrugation of the graphene sheet or ineffective charge screening. San Jose *et al.* calculated the Fano factor analytically for one dimensional disorder, with the result $F \lesssim 1/3$. The authors analyzed the case of two dimensional disorder numerically, with the universal result $F = 0.295$. Lewenkopf *et al.*, [102] have also studied the effect of disorder numerically, finding that the Fano factor is approximately independent of carrier density for strong disorder. Following these works, Schuessler *et al.* [150] developed an analytic theory for conduction in disordered graphene, valid for disorder leading to intra-valley scattering in the entire crossover regime from ballistic to diffusive transport. Together, these works show that the Fano factor value $F = 1/3$ is robust for many types of disorder.

Since the prediction of non-zero shot noise, many groups have studied shot noise on graphene in a variety of circumstances. For graphene FET geometries, Cayssol *et al.* [43] studied the effect of potential steps on the transport, finding that, for ballistic transport, the presence of metallic contacts can shift the location of the Fano factor maximum away from the Dirac point, even in clean graphene. Golub and Horovitz [70] used a kinetic equation approach to study the effect of the long-range Coulomb interaction on the shot noise. While the conductance and shot noise at the Dirac point are both affected by the presence of the interaction, the Fano factor remains $F = 1/3$. Rycerz *et al.* [142] have predicted other shot noise values in certain quantum billiard geometries. While the value $F = 1/3$ persists for many billiard geometries, greatly shrinking at least one billiard opening leads to tunneling behavior with $F = 1$. Other values $1/3 \leq F \leq 1$ are also predicted in the crossover regime between tunneling and pseudo-diffusive behavior. Shot noise has also been studied

theoretically for ballistic bilayer graphene [155] and graphene p-n junctions. [46]

3.3.2 Experiment

Prior to the ascendance of graphene, shot noise was studied in carbon nanotubes in a variety of situations. In 2002, Roche *et al.* [139] measured extremely low shot noise in suspended ropes of single-wall nanotubes. The noise was on the order of $S_{\text{Poisson}}/150$, a signature of one dimensional ballistic transport. In contrast, Onac *et al.* [125] observed Poissonian and super-Poissonian shot noise under different conditions in quantum dots made of single-walled carbon nanotubes, with a maximum Fano factor near $F \simeq 3$. The shot noise in nanotube-based quantum dots is controlled by the ratio of the tunneling rates between the dot and the leads, [53] and can in general be greater than, less than [23, 117, 118] or equal to the Poisson value. In addition to ropes and quantum dots, shot noise has also been studied for single [180] and multi-walled [126] carbon nanotubes and for nanotube systems such as Fabry-Perot interferometers, [78] single [56] and multi-walled [181] field effect transistors and spin diodes. [112]

In 2007, Miao *et al.* [114] verified the conductance value calculated by Tworzydło *et al.* [167] using the Landauer formula, but the shot noise was not measured. The first shot noise measurements on graphene FET devices were made nearly simultaneously in 2008 by DiCarlo *et al.* [59] and Danneau *et al.* [50] DiCarlo *et al.* verified the value $F = 1/3$ at the Dirac point, but they did not observe any voltage dependence of the Fano factor, as predicted by Lewenkopf *et al.* [102] for diffusive transport. This indicates that the transport in that experiment was diffusive. Following these observations, Danneau *et al.* were further able to measure a gate voltage dependence of the Fano factor, as expected in the ballistic regime, finding qualitative agreement with the theory of transport through evanescent modes. However, the observed voltage scale for the decay of the Fano factor was considerably larger than that predicted by

theory. [167] This discrepancy is the subject of Chp. 5.

While the prediction and experimental verification of the universal shot noise value $F = 1/3$ suggests that current at the Dirac point of graphene is carried by evanescent modes, it is an ambiguous signature, as this value agrees with the value for diffusive metals. Furthermore, the experiment that provides most of the evidence for evanescent mode transport shows significant deviations from the theory for the energy scale of the Fano factor. This thesis is motivated by these shortcomings.

In Chp. 4, we propose several geometries for which the Fano factor provides unambiguous signatures of evanescent mode transport. We consider graphene nano-ribbons based on the FET geometry considered by Tworzydło *et al.* and predict $F = 1/4$, a new value. We also calculate a novel Fano factor value $F = 1/(8 \ln 2)$ for the case of a long graphene superlattice. Verification of these predictions would provide compelling evidence for evanescent mode transport. In Chp. 5, we propose that the experiments of Danneau *et al.* [50] are consistent with the theory of evanescent mode transport when the effect of doping from the leads is accounted for. These calculations provide valuable contributions to shot noise studies on graphene.

CHAPTER IV

UNAMBIGUOUS SIGNATURES OF EVANESCENT MODE TRANSPORT ON GRAPHENE

Clean graphene is known to exhibit non-equilibrium current fluctuations. This noise is due to evanescent modes, which dominate transport near the Dirac point. However, the predicted [167] and experimentally verified [50, 59] universal value $F = 1/3$ is the same as that of a diffusive conductor, [19] and also that of diffusive graphene. [102] Hence, the measured Fano factor value $F = 1/3$ may be due to disorder, rather than evanescent modes. In this chapter, we propose experimental geometries for which the transport through evanescent modes at the Dirac point of graphene has unambiguous signatures.

We first study a sheet of graphene subject to gate potentials that induce two strips of graphene with chemical potential at the Dirac point, separated by a highly doped region. We show that the Fano factor takes a universal value in this geometry: $F = 1/4$. This value is different from that of diffusive conductors, and it provides an unambiguous signature of evanescent modes. Graphene devices with multiple potential steps, as required for the proposed test of evanescent transport, have been implemented experimentally. [159]

Similar results are obtained for longer cascades of $p > 2$ strips of graphene with evanescent transport. In particular, we take the limit $p \to \infty$ of a long graphene superlattice with a piecewise constant potential. Such superlattices have recently received much attention as a way to engineer the band structure of graphene, [1, 172, 128, 31, 129, 132, 13, 14, 26, 8, 131, 67] to the point of creating new Dirac cones in the electronic spectrum. [31, 129, 132, 13, 14, 26, 8] Under certain conditions, we find

another universal value of the Fano factor for such superlattices: $F = 1/(8\ln 2) \simeq 0.18$.

This chapter is organized as follows: in Sec. 4.1, we analytically derive the universal Fano factor $F = 1/4$ for two evanescent regions in series. We study the departures of F from this value numerically as asymmetries are introduced into the setup, an additional experimental signature of evanescent mode transport. In Sec. 4.2, we first generalize our approach to cascades of an arbitrary number p of evanescent regions in series before taking the long superlattice limit $p \to \infty$. We conclude with a summary in Sec. 4.3.

4.1 Evanescent mode transport through two evanescent strips in series

We analyze the transport through a graphene sheet of width W subject to gates that allow one to tune two strips of lengths L and R to a chemical potential close to the Dirac point. We denote the electrostatic potentials in those strips by V_L and V_R, respectively. The two strips are separated by a highly doped region of length λ at electric potential V_d, as in Fig. 7.

We model the leads contacting the sample by highly doped regions of graphene to the left and to the right of the sample at voltage V_ℓ, as in the calculations of Tworzydło *et al.* [167] It has been confirmed using density functional calculations that this model correctly describes transport into certain types of contacts. [17] In units where $\hbar = 1$, our model Hamiltonian takes the form

$$H_\gamma = v_{\rm F}\vec{\sigma}_\gamma \cdot \vec{p} + V(x), \tag{56}$$

where $\vec{\sigma}_\gamma = (\gamma\sigma_x, \sigma_y)$ is a vector of Pauli matrices with the valley index $\gamma = \pm 1$, $\vec{p} = -i\vec{\nabla}$ is the electron momentum and $v_{\rm F}$ is the electron velocity. The potential $V(x)$ takes the value V_d in the highly doped regions, V_ℓ in the leads and the gate voltages V_L and V_R in the regions that can be tuned to the Dirac point (see Fig. 7).

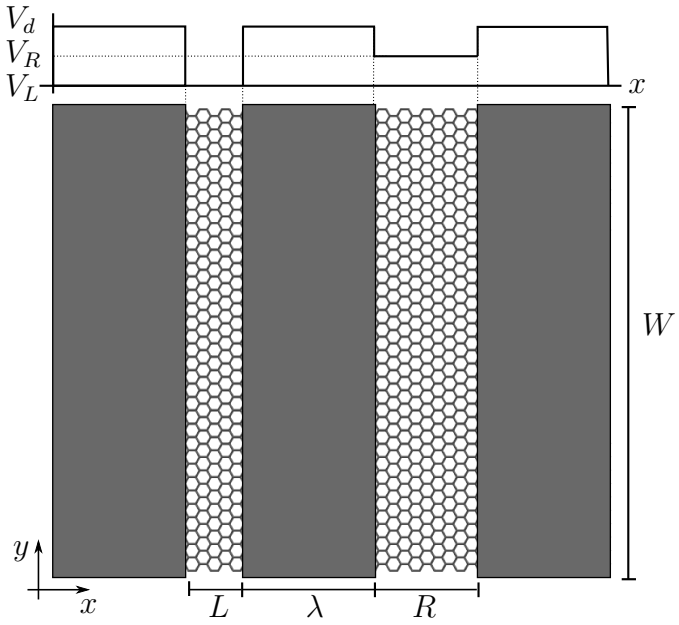

Figure 7: Schematic of a graphene strip of width W consisting of a highly doped region (gray rectangle) of length λ at voltage V_d separated by weakly doped regions of length L and R. Separate gate leads (not shown) control the voltages V_L and V_R in the weakly doped regions. The system is contacted at either end by ideal leads (not shown) at the lead potential V_ℓ. The electrostatic potential in the strip is plotted above the schematic as a function of x.

We assume that the microscopic potential, represented by the potential $V(x)$ in our long-wavelength theory, is smooth on the lattice scale, so that it does not scatter between valleys.

4.1.1 Wave functions and the transmission probability

Disregarding spin, the plane wave solutions to Eq. (56) take the form

$$\psi_{n,k}(\vec{r}) = \chi_{n,k}(y)e^{ikx}, \tag{57}$$

where

$$\chi_{n,k}(y) = a_n \begin{pmatrix} 1 \\ z_{n,k} \\ 0 \\ 0 \end{pmatrix} e^{iq_n y} + a'_n \begin{pmatrix} 0 \\ 0 \\ z_{n,k} \\ 1 \end{pmatrix} e^{iq_n y} + b_n \begin{pmatrix} z_{n,k} \\ 1 \\ 0 \\ 0 \end{pmatrix} e^{-iq_n y} + b'_n \begin{pmatrix} 0 \\ 0 \\ 1 \\ z_{n,k} \end{pmatrix} e^{-iq_n y}. \tag{58}$$

The complex number $z_{n,k}$ is defined as

$$z_{n,k} = \pm \frac{k + iq_n}{\sqrt{k^2 + q_n^2}}, \tag{59}$$

where the $\pm$ sign refers to the conduction and valence bands, respectively. These states have energy $\epsilon = V_d \pm v_{\mathrm{F}} \sqrt{k_d^2 + q_n^2}$ in the highly doped regions and $\epsilon = V_{L(R)} \pm v_{\mathrm{F}} \sqrt{k_{L(R)}^2 + q_n^2}$ in the left (right) gated regions. We choose $\left|V_{\ell(d)}\right| \gg v_{\mathrm{F}}/L, v_{\mathrm{F}}/R$ such that, at the Fermi level, all relevant modes are propagating in the leads and the highly doped regions (real $k_{\ell(d)}$). In the weakly doped regions, both propagating (real $k_{L(R)}$) and evanescent (imaginary $k_{L(R)}$) modes are possible. For particles incident from the left in the n-th mode, the scattering wave function can be constructed from the plane wave states of Eq. (57) as

$$\Psi(\vec{r}) = \begin{cases} \chi_{n,k_d} e^{ik_d x} + r_n \chi_{n,-k_d} e^{-ik_d x} & x < 0 \\ \alpha_n \chi_{n,k_L} e^{ik_L x} + \beta_n \chi_{n,-k_L} e^{-ik_L x} & 0 < x < L \\ \gamma_n \chi_{n,k_d} e^{-ik_d(x-L)} + \delta_n \chi_{n,-k_d} e^{-ik_d(x-L)} & L < x < L + \lambda \\ \epsilon_n \chi_{n,k_R} e^{ik_R(x-L-\lambda)} + \zeta_n \chi_{n,-k_R} e^{-ik_R(x-L-\lambda)} & L + \lambda < x < L + R + \lambda \\ t_n \chi_{n,k_d} e^{ik_d(x-L-R-\lambda)}. & x > L + R + \lambda \end{cases} \tag{60}$$

The transverse wave numbers q_n and the wave function coefficients $\{a_n, a'_n, b_n, b'_n\}$ depend on the boundary conditions at $y = 0$ and $y = W$. We consider a class of boundary conditions that do not couple longitudinal and transverse wave numbers. [167] Specifically, we consider the infinite mass, metallic armchair and semiconducting armchair edge boundary conditions (see Appendix A). For these boundary conditions, the transverse wave number is given by $q_n = (n + \alpha)\,\pi/W$, where

$$\alpha = \begin{cases} 1/2 & \text{infinite mass} \\ 0 & \text{metallic armchair} \\ 1/3 & \text{semiconducting armchair.} \end{cases} \tag{61}$$

In the continuum limit $W \gg L, R$, which we take for the remainder of this chapter, the

transport properties should be independent of the boundary conditions. Accordingly, α drops out of the calculation.

Enforcing continuity of the wave function at $x = 0$, $x = L$, $x = L + \lambda$ and $x = L + R + \lambda$ leads to eight independent equations:

$$\begin{aligned}
\begin{pmatrix} 1 \\ z_{n,k_d} \end{pmatrix} + r_n \begin{pmatrix} 1 \\ z_{n,-k_d} \end{pmatrix} &= \alpha_n \begin{pmatrix} 1 \\ z_{n,k_L} \end{pmatrix} + \beta_n \begin{pmatrix} 1 \\ x_{n,-k_L} \end{pmatrix}, \\
\alpha_n e^{ik_L L} \begin{pmatrix} 1 \\ z_{n,k_L} \end{pmatrix} + \beta_n e^{-ik_L L} \begin{pmatrix} 1 \\ x_{n,-k_L} \end{pmatrix} &= \gamma_n \begin{pmatrix} 1 \\ z_{n,k_d} \end{pmatrix} + \delta_n \begin{pmatrix} 1 \\ z_{n,-k_d} \end{pmatrix}, \\
\gamma_n e^{ik_d \lambda} \begin{pmatrix} 1 \\ z_{n,k_d} \end{pmatrix} + \delta_n e^{-ik_d \lambda} \begin{pmatrix} 1 \\ z_{n,-k_d} \end{pmatrix} &= \epsilon_n \begin{pmatrix} 1 \\ z_{n,k_R} \end{pmatrix} + \zeta_n \begin{pmatrix} 1 \\ x_{n,-k_R} \end{pmatrix}, \\
\epsilon_n e^{ik_R R} \begin{pmatrix} 1 \\ z_{n,k_R} \end{pmatrix} + \zeta_n e^{-ik_R R} \begin{pmatrix} 1 \\ x_{n,-k_R} \end{pmatrix} &= t_n \begin{pmatrix} 1 \\ z_{n,k_d} \end{pmatrix},
\end{aligned} \tag{62}$$

where the coefficients a_n, a'_n, b_n, b'_n have been eliminated. Since the Dirac equation is a first order differential equation, there is no need to enforce continuity of the first derivative of the wave function, as with the Schrödinger equation.

4.1.2 The universal limit

We first consider the situation in which both weakly doped regions of the sample are tuned to the Dirac point, $V_L = V_R = 0$. In the limit $|V_d| \gg v_\mathrm{F}/L$, the coefficient z_{n,k_d} approaches unity, and the system of Eq. (62) yields the transmission amplitude

$$t_n = \left[e^{ik_d \lambda} \sinh(n\mathcal{L}) \sinh(n\mathcal{R}) + e^{-ik_d \lambda} \cosh(n\mathcal{L}) \cosh(n\mathcal{R}) \right]^{-1} \tag{63}$$

for mode n at the Fermi level, which we choose to be at energy $\epsilon_\mathrm{F} = 0$. The dimensionless "lengths" $\mathcal{L}$ and $\mathcal{R}$ are given by $\mathcal{L} = \pi L/W$ and $\mathcal{R} = \pi R/W$. The Fano factor is found from the transmission probabilities $T_n = |t_n|^2$ using Eq. (53). [98, 37] In the continuum limit, $W \gg L, R$, the sums over the modes become integrals, and

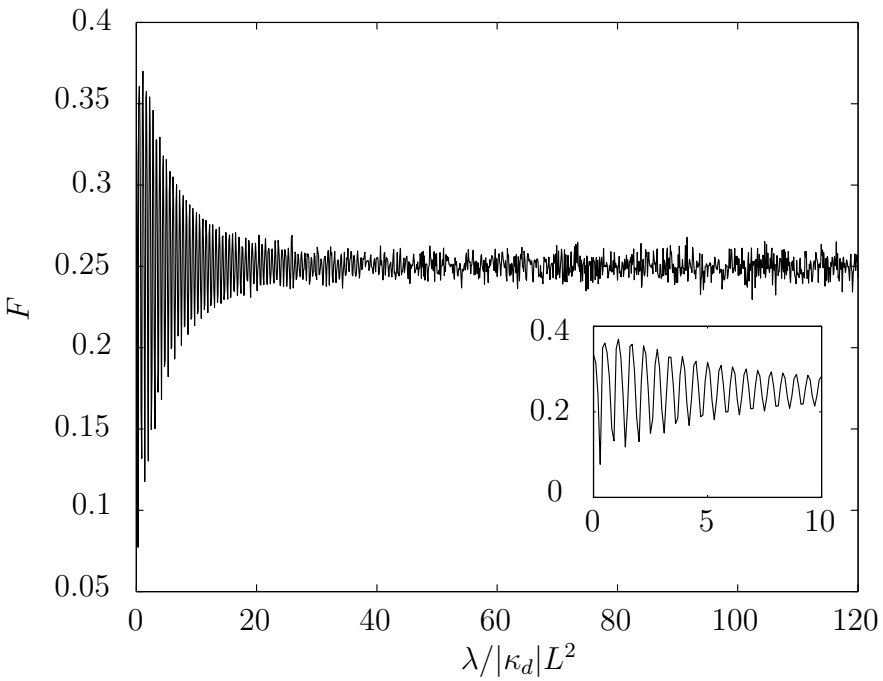

Figure 8: Fano factor F for two graphene strips as in Fig. 7 for $L = R$ and chemical potential at the Dirac point, as a function of the length of the highly doped region in units of $|\kappa_d|\, L^2$. The curve is calculated from Eq. (53) in the limit $N \to \infty$ and is shown magnified in the inset for small values of the lead thickness. The Fano factor approaches 0.33... as $\lambda \to 0$, in agreement with the calculations of Tworzydło *et al.* [167] For large values of the length of the highly doped region, the Fano factor approaches 0.25..., in agreement with the analytic calculations presented in the text.

the Fano factor is given by $F = 1 - I_2/I_1$ with

$$I_1 = \int_0^\infty T_n dn,$$
$$I_2 = \int_0^\infty T_n^2 dn. \tag{64}$$

In Fig. 8, the transmission probability determined from Eq. (63) is integrated numerically in order to obtain the Fano factor for a symmetric system ($L = R$) as a function of the thickness λ of the central, highly doped region. As $\lambda \to 0$, the Fano factor approaches 1/3. This result agrees with the calculations of Tworzydło *et al.*, [167] as this limit corresponds to transmission through a single graphene strip at the Dirac point. In contrast, the Fano factor approaches 0.25... in the limit $\lambda \gg |\kappa_d|\, L^2$, where $\kappa_d = V_d/v_{\rm F}$.

This numerical result suggests that the Fano factor may be accessible analytically in the limit $\lambda \gg |\kappa_d|\, L^2$, and we show in this section that it is. Consider first I_1. We write the transmission probability determined from Eq. (63) in the form

$$T_n = \frac{1}{\alpha(n)} \frac{1}{1 + \beta(n) \cos[2k_d(n)\lambda]}, \tag{65}$$

where

$$\begin{aligned} \alpha(n) &= \cosh^2(n\mathcal{L}) \cosh^2(n\mathcal{R}) + \sinh^2(n\mathcal{L}) \sinh^2(n\mathcal{R}) \\ \beta(n) &= 2 \cosh(n\mathcal{L}) \cosh(n\mathcal{R}) \sinh(n\mathcal{L}) \sinh(n\mathcal{R})/\alpha(n) \\ k_d(n) &= \sqrt{\kappa_d^2 - n^2\pi^2/W^2}. \end{aligned} \tag{66}$$

The transmission probability decays exponentially with $n\,(\mathcal{L} + \mathcal{R})$, and the integrals in Eq. (64) are thus cut-off at $n \simeq \max\{1/\mathcal{L}, 1/\mathcal{R}\}$.

Linearizing $k_d(n)$ about an index n_0 and disregarding a phase shift, the cosine function in Eq. (65) oscillates like $\cos[\omega(n_0)n]$ with

$$\omega(n_0) = \frac{2\pi^2 \lambda n_0}{|\kappa_d| W^2} \sim \frac{2\lambda}{|\kappa_d| L^2} \left(\frac{\pi L}{W}\right), \tag{67}$$

where we have used the scale of the exponential decay to write $n_0 \sim 1/\mathcal{L} = W/\pi L$. The key observation is that for $\lambda \gg |\kappa_d|\, L^2$, the cosine function oscillates rapidly on the scale of the exponential decay of T_n. Therefore, in this limit, $\alpha(n)$ and $\beta(n)$ are constant within one period of oscillation

$$\Delta n(n_0) = \frac{\kappa_d W^2}{\lambda \pi n_0} \tag{68}$$

of the $\cos[2k_d(n)\lambda]$ function around a given index n_0. Consequently, I_1, restricted to an interval of length $\Delta n(n_0)$ around n_0, becomes the integral of the function $[1 + \beta(n) \cos(\delta - \omega n)]^{-1}$, which can be done analytically. Here, δ and ω are found by linearizing $2k_d(n)\lambda = \delta(n_0) - \omega(n_0)n$ with

$$\begin{aligned} \delta(n_0) &= 2\kappa_d \lambda \left(1 + n_0^2\pi^2/2\kappa_d^2 W^2\right) \\ \omega(n_0) &= 2\pi^2 \lambda n_0/\kappa_d W^2. \end{aligned} \tag{69}$$

In the limit $\lambda/\left|\kappa_d\right| L^2 \to \infty$, the periods $\Delta n(n_0)$ are short compared to the decay scale of the transmission probability set by $\mathcal{L}+\mathcal{R}$, and the requisite sum over all periods becomes a second integral. In this limit, I_1 is given by

$$I_1 = \int_{-\infty}^{\infty} \frac{\omega(n_0) dn_0}{2\pi\alpha(n_0)} \int_{n_0-\pi/\omega}^{n_0+\pi/\omega} \frac{dn}{1+\beta(n_0)\cos\left(\delta-\omega n\right)}. \tag{70}$$

It can be shown using contour integration that the integral within each period is

$$\int_{-\pi}^{\pi} \frac{dx}{1+\beta\cos x} = \frac{2\pi}{\sqrt{1-\beta^2}} \tag{71}$$

when $|\beta|<1$. Noting that

$$\begin{aligned} 0 &\leq \left(\cosh n\mathcal{L}\cosh n\mathcal{R} - \sinh n\mathcal{L}\sinh n\mathcal{R}\right)^2 \\ &= \alpha\left(1-\beta\right), \end{aligned} \tag{72}$$

and that $\alpha > 0$ for all n, we have $\beta(n_0) \leq 1$. Equality is achieved only in the limit $n \to \infty$. However, this limit is not relevant to the transport, as the transmission probability is exponentially damped, with the maximum mode index scaling like $n_{\max} \simeq \max\left\{1/\mathcal{L}, 1/\mathcal{R}\right\}$. Hence, β is strictly less than unity. To fulfill the other side of the inequality, we note that

$$0 \leq 2\cosh n\mathcal{L}\cosh n\mathcal{R}\sinh n\mathcal{L}\sinh n\mathcal{R}, \tag{73}$$

as $\sinh(n)$ is negative only for $n<0$ and $\cosh(n)$ is positive for all n. Then $0 \leq \beta(n) < 1$, and the integral over each period converges.

In the limit $\lambda/|\kappa_d|L^2 \gg 1$, we find

$$I_1 = \int_0^{\infty} \frac{1}{\gamma_-(n_0)} dn_0, \tag{74}$$

where

$$\gamma_{\pm}(n_0) = \cosh^2(n_0\mathcal{L})\cosh^2(n_0\mathcal{R}) \pm \sinh^2(n_0\mathcal{L})\sinh^2(n_0\mathcal{R}). \tag{75}$$

In the same limit, the integral I_2 of Eq. (64) can be calculated in the same manner, with the result

$$I_2 = \int_0^{\infty} \frac{\gamma_+(n_0)}{\gamma_-^3(n_0)} dn_0. \tag{76}$$

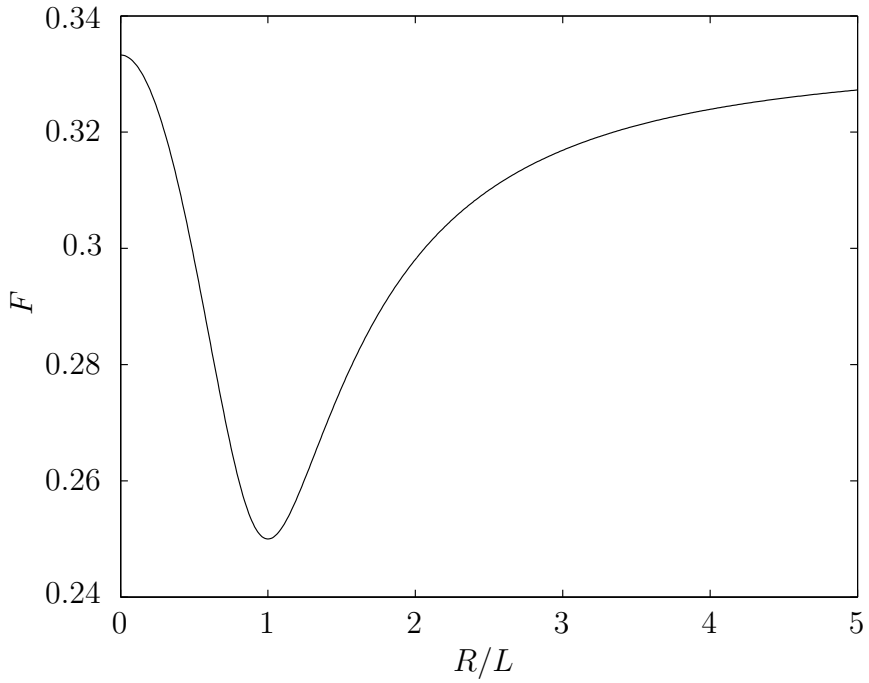

Figure 9: Length ratio dependence of the Fano factor for two graphene strips as in Fig. 7 with chemical potential at the Dirac point. The curve is calculated from the integrals given in Eq. (74) and Eq. (76) in the continuum limit with $\lambda \gg |\kappa_d|\, L^2$. The Fano factor shows a minimum of $0.25\ldots$ for the symmetric case ($R/L = 1$) and tends toward $0.33\ldots$ as $R/L \to 0$ or $R/L \to \infty$, in agreement with the results of Tworzydło *et al.* [167]

For the symmetric case, $L = R$, the integrals in Eq. (74) and Eq. (76) can also be evaluated analytically, resulting in a Fano factor of $F = 1/4$, in accordance with the numerical results shown in Fig. 8.

Evanescent transport in this geometry thus has an unambiguous signature, with a Fano factor that differs from the one in a disordered sample. For the asymmetric case, we calculate the Fano factor numerically as a function of R/L, with the results plotted in Fig. 9. The Fano factor approaches $1/3$ in the limit $R/L \to \infty$, which corresponds to a single graphene region at the Dirac point, as considered by Tworzydło *et al.* [167]

4.1.3 Digression on the probability distribution

Coincidentally, the Fano factor value $F = 1/4$ for this geometry is the same as that of a ballistic quantum dot. [82] Despite this coincidence, transport through the two systems is not equivalent. The probability distribution of transmission eigenvalues $P(T)$ is defined as

$$P(T) = \int_0^\infty \delta\left(T_n - T\right) dn, \tag{77}$$

where $\delta(x)$ is the Dirac delta function. We write the probability distribution integral as an integral over a single period of $\cos\left(2k\lambda\right)$, summed over all periods (indexed by n_0). In the limit $\lambda/|\kappa_d|L^2 \gg 1$, this sum becomes a second integral. Writing the transmission probability as in Eq. (65), we have

$$P(T) = \sum_{n_0} \int_{n_0-\pi/\omega}^{n_0+\pi/\omega} \delta\left(\frac{1}{\alpha}\frac{1}{1+\beta\cos 2k\lambda} - T\right) dn. \tag{78}$$

Again, we assume a linearized longitudinal wave number k such that $2k\lambda \approx \delta - \omega n$.

Recall that for functions $f(x)$ and $g(x)$, the Dirac delta function satisfies

$$\int_{-\infty}^{\infty} f(x)\delta\left[g(x)\right] dx = \sum_i \left|\frac{f(x_i)}{g'(x_i)}\right|, \tag{79}$$

where $\{x_i\}$ are the roots of $g(x)$. Using this relation, the integral of the Dirac function over each period is given by

$$\int_{n_0-\pi/\omega}^{n_0+\pi/\omega} \delta(T_n - T)dn = 2\left|\frac{1}{dT_n/dn}\right|_{n=n_i}, \tag{80}$$

where $T_{n_i} = T$ and each period contains two such roots, leading to the factor of 2 in the numerator. However, the equation $T_n = T$ does not have roots for all periods n_0 for all T. In order to have a root within the period n_0, we require that $\max\left(T_n\right) \geq T$ and $\min\left(T_n\right) \leq T$ within the period. For any n_0, we have

$$\max_{n_0}(T_n) = \frac{1}{\alpha\left(1-\beta\right)} = 1. \tag{81}$$

The minimum within the period n_0 is found to be

$$\min_{n_0}(T_n) = \frac{1}{\alpha\left(1+\beta\right)} = \frac{1}{\cosh^2(2n_0\mathcal{L})}. \tag{82}$$

Since

$$\left|\frac{dT_n}{dn}\right| = \frac{\omega(n_0)}{\alpha(n_0)} \frac{\beta(n_0)\sin\left(\delta-\omega n\right)}{\left[1+\beta(n_0)\cos\left(\delta-\omega n\right)\right]^2}, \tag{83}$$

we have

$$P(T) = \frac{1}{\pi}\int_0^\infty dn_0 \frac{\alpha(n_0)\left[1+\beta(n_0)\cos\left(\delta-\omega n_i\right)\right]^2}{\beta(n_0)\sin\left(\delta-\omega n_i\right)} \Theta\left(T-\mathrm{sech}^2\left(2n\mathcal{L}\right)\right), \tag{84}$$

where $\Theta(x)$ is the Heaviside step function and we have used the limit $\lambda/|\kappa_d|L^2 \gg 1$ to convert the sum over periods to an integral, so that $\sum_{n_0} \to \int dn_0\, \omega(n_0)/2\pi$.

Recall that n_i is defined such that $T_{n_i} = T$. Hence,

$$\delta - \omega n_i = \arccos\left[\frac{1}{\beta(n_0)}\left(\frac{1}{\alpha(n_0)T}-1\right)\right]. \tag{85}$$

Using the property $\sin\left(\arccos x\right) = \sqrt{1-x^2}$, we have

$$\begin{aligned}\cos\left(\delta-\omega n_i\right) &= \frac{1}{\beta\alpha T}(1-\alpha T)\\ \sin\left(\delta-\omega n_i\right) &= \sqrt{1-\frac{1}{\beta^2\alpha^2T^2}(1-\alpha T)^2}.\end{aligned} \tag{86}$$

Therefore, the full probability distribution of transmission eigenvalues $P(T)$ for this geometry is

$$P(T) \propto \frac{1}{\sqrt{T^2(1-T)}}\int_0^\infty dn \frac{\Theta\left(T-\mathrm{sech}^2\left(2n\mathcal{L}\right)\right)}{\sqrt{T\cosh^2\left(2n\mathcal{L}\right)-1}}. \tag{87}$$

For the case of a symmetric chaotic quantum dot, one has, in contrast, [82]

$$P_{\mathrm{dot}}(T) \propto \frac{1}{\sqrt{T(1-T)}}. \tag{88}$$

While these two distributions have the same ratios between their second and first moments, the third moment distinguishes them. The third cumulant $\langle \delta I^3 \rangle$ is proportional to $T(1-T)(1-2T)$. [100, 101, 99] It is easily shown that this quantity vanishes for $P_{\mathrm{dot}}(T)$, but it does not for $P(T)$.

The dependence of the Fano factor on the ratio R/L shown in Fig. 9 is a more distinctive signature of evanescent wave transport than the value $F = 1/4$ at $L = R$

alone. Unfortunately, the lengths of the gated regions cannot be changed easily in an experiment. However, the gate voltages V_L and V_R can be controlled. We discuss the dependence of F on those gate voltages in the next subsection.

4.1.4 Voltage induced signatures of evanescent mode transport

Here, we obtain the dependence of the Fano factor on the gate voltage V_R in the symmetric configuration, $L = R$ (cf. Fig. 7), with the left gated region at the Dirac point, V_L=0. Enforcing continuity of the wave function at each highly-weakly doped region interface, as in the previous section, the transmission amplitude as a function of k_R, the longitudinal wave number in the right weakly doped region, takes the form

$$t_n = k_R \left[e^{-ik_d\lambda} \cosh n\mathcal{L} \left(k_R \cos k_R L - i\kappa_R \sin k_R L \right) + e^{ik_d\lambda} \frac{n\pi}{W} \sinh n\mathcal{L} \sin k_R L \right]^{-1}, \tag{89}$$

where $\kappa^2_{R(d)} = k^2_{R(d)} + q_n^2$ with $\kappa_{R(d)} = V_{R(d)}/v_{\rm F}$. We consider the limit $\lambda/\left|\kappa_d\right| L^2 \to \infty$ of the resulting expression for the Fano factor, following the methods of the previous section.

From the transmission amplitude Eq. (89), it can be shown the the transmission probability takes the form

$$T_n = \frac{1}{c_1} \frac{1}{c_2 \cos 2k_R\lambda + c_3 \sin 2k_R\lambda + c_4}, \tag{90}$$

where $\{c_1, c_2, c_3, c_4\}$ are functions of k_R and q_n but independent of k_d. The specific form of these functions depends on whether $k_R = \sqrt{V_R^2 - q_n^2}$ is real or imaginary (in which case we write $k_R \to ik_R$). The c_1 to c_4 functions are listed in Table 1 for real and imaginary k_R.

In order to calculate the Fano factor using the integrals I_1 and I_2 of Eq. (64), we first note that any integral involving a function of the transmission probability T can be split into regions where k_R is real and imaginary. For an arbitrary function $f(T)$, we have

$$\int_0^\infty f(T_n) dn = \int_{q_n \le V_R} f\left(T_n^{\rm Re}\right) dn + \int_{q_n > V_R} f\left(T_n^{\rm Im}\right) dn, \tag{91}$$

Table 1: Form of the c functions appearing in the transmission probability Eq. (90) for real ($\Re$) and complex ($\Im$) values of k_R. When k_R is complex, it is assumed to be of the form ik_R where k_R is a real number. Hence, all references to k_R in the table assume a real number, and the complex nature of the wave number is already reflected in the form of the coefficients as they appear here.

	$k \in \Re$	$k \in \Im$
c_1	$2k_R^2$	$2k_R^2$
c_2	$q_n k_R \sin 2k_R L \sinh 2q_n L$	$q_n k_R \sinh 2k_R L \sinh 2q_n L$
c_3	$-2V_R q_n \sin^2 k_R L \sinh 2q_n L$	$-2V_R q_n \sinh^2(k_R L) \sinh 2q_N L$
c_4	$2q_n^2 \sin^2 k_R L \sinh q_n L + \cosh^2(q_n L)\times$ $\times \{V_R^2 + k_R^2 + (k_R^2 - V_R^2)\cos 2k_R L\}$	$2k_R^2 \cosh^2(k_R L)\cosh^2(q_n L) + \sinh^2(k_R L)\times$ $\times \{V_R^2 - q_n^2 + (V_R^2 + q_n^2)\cosh 2q_n L\}$

where $T_n^{\mathrm{Re/Im}}$ is the transmission probability Eq. (90) with the real/imaginary forms of c_1 to c_4. As in the previous section, we approximate the functions $\{c_1, c_2, c_3, c_4\}$ as constant within one oscillation of $\cos(2k_R\lambda)$, indexed by n_0. This approximation is again exact in the limit $\lambda/|\kappa_d|L^2 \gg 1$, where the cosine function oscillates rapidly compared to the scale of the decay of the transmission probability. We then integrate I_1 and I_2 by first integrating over each period before summing over all periods. In the continuum limit, this sum becomes a second integral, as in the previous section.

For I_1, we have

$$I_1 = \int_0^\infty \frac{\omega(n_0)dn_0}{2\pi c_1(n_0)} \int_{n_0-\pi/\omega}^{n_0+\pi/\omega} \frac{dn}{c_2(n_0)\cos 2k(n)\lambda + c_3(n_0)\sin 2k(n)\lambda + c_4(n_0)} \tag{92}$$

The innermost integral over each period can be found using contour integration, with the result

$$\begin{aligned} \int_{-\pi}^{\pi} \frac{dx}{a\cos x + b\sin x + c} &= \frac{2\pi}{(c^2 - a^2 - b^2)^{1/2}} \\ \int_{-\pi}^{\pi} \frac{dx}{(a\cos x + b\sin x + c)^2} &= \frac{2\pi c}{(c^2 - a^2 - b^2)^{3/2}} \end{aligned} \tag{93}$$

Using these relations, the Fano factor is found to be

$$F = 1 - \frac{\int_0^\infty g(n_0)dn_0}{\int_0^\infty f(n_0)dn_0}, \tag{94}$$

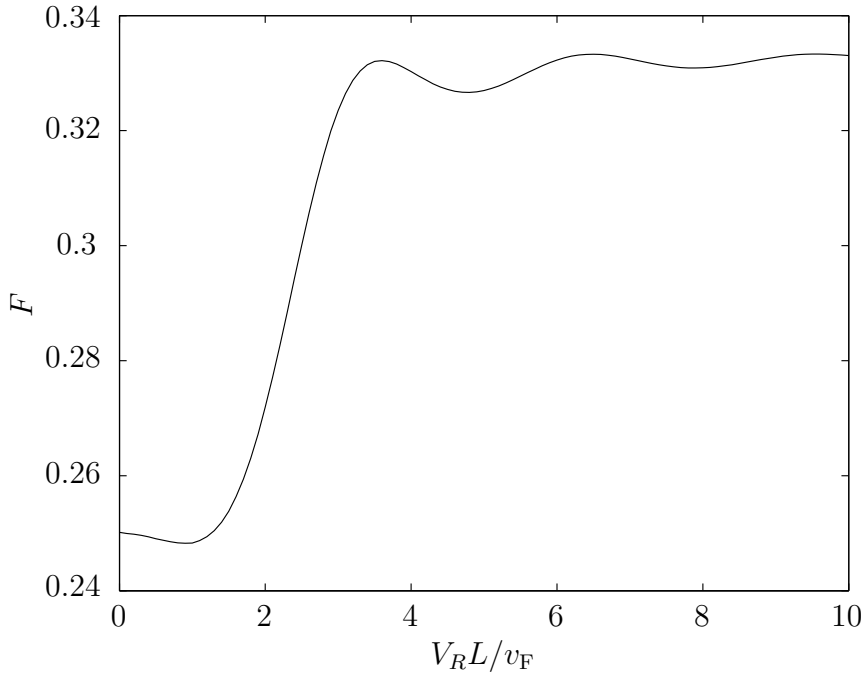

Figure 10: The Fano factor for two graphene strips as in Fig. 7 for $L = R$ and $\lambda \gg |\kappa_d|\, L^2$ as a function of gate voltage V_R in the right graphene region, measured in units of v_F/L. Gate leads fix the chemical potential in the left evanescent region to the Dirac point ($V_L = 0$). The Fano factor is $0.25\ldots$ when V_R is at the Dirac point, as previously calculated, and it approaches $0.33\ldots$ as $V_R \gg v_F/L$.

where

$$f(x) = \frac{c_1(x)}{[c_4^2(x) - c_3^2(x) - c_2^2(x)]^{1/2}}$$
$$g(x) = \frac{c_1^2(x)c_4(x)}{[c_4^2(x) - c_3^2(x) - c_2^2(x)]^{3/2}} = f^3(x)\frac{c_4(x)}{c_1(x)} \tag{95}$$

We perform this final integration, corresponding to the sum over periods $\Delta n(n_0)$, numerically, with the result plotted in Fig. 10. The Fano factor is $1/4$ when the gate voltage V_R is at the Dirac point, as previously calculated, and it approaches $1/3$ in the limit $V_R \gg v_F/L$. The crossover between $F = 1/3$ and $F = 1/4$ within a gate voltage interval of $\Delta V_R \simeq v_F/L$ serves as another distinctive signature of evanescent mode transport.

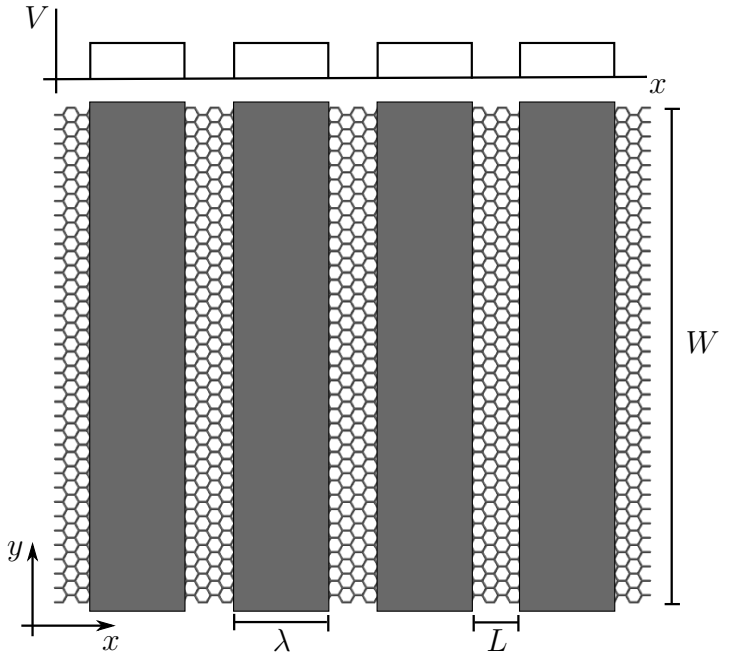

Figure 11: Schematic of a segment of a graphene superlattice of width W, consisting of evanescent graphene regions of length L separated by doped regions (gray rectangles) of length λ at the potential V_d. Separate gate leads (not shown) fix the voltages in the graphene regions to the Dirac point, $V = 0$. The superlattice is contacted at either end by leads at potential V_ℓ (not shown). The superlattice potential is plotted above the schematic as a function of x.

4.2 Evanescent mode transport in a graphene superlattice

In this section, we investigate the shot noise for transport through a graphene superlattice consisting of many evanescent strips tuned to the Dirac point, alternating with doped regions, as depicted in Fig. 11. In Sec. 4.2.2, we take the long superlattice limit of an infinite number of such regions. We take the graphene regions gated to the Dirac point to be of length L, and they are separated by doped regions of length λ at the voltage V_d. The contacts at both ends are again modeled by highly doped graphene at the lead potential V_ℓ. The potential V_ℓ drops out of the calculation in the limit $V_\ell, V_d \gg v_{\rm F}/L$.

4.2.1 Transmission through a cascade of evanescent strips in series

In order to calculate the transmission probability through the graphene superlattice depicted in Fig. 11, we employ the transfer matrix method. [46] The transfer matrix $M(x, x')$ for the requisite Dirac spinors of a mode with transverse momentum q satisfies the equation

$$\partial_x M(x, x') = \left[-i \frac{V(x)}{v_{\rm F}} \sigma_x + q \sigma_z \right] M(x, x'). \tag{96}$$

In addition, one has [46] $M(x, x) = I$, $M(x, x') = M(x, x'')M(x'', x')$, $\det M(x, x') = 1$ and $M^\dagger(x, x')\sigma_x M(x, x') = \sigma_x$. The latter condition ensures current conservation.

We write the transfer matrix in the doped regions as $M_d(x, x') = A_d(x)A_d^{-1}(x')$. Here, $A_d(x)$ satisfies Eq. (96) in the doped regions, where $V(x) = V_d$. Similarly, the transfer matrix in the lead regions contacting either end of the superlattice is $M_\ell(x, x') = A_\ell(x)A_\ell^{-1}(x')$, where $A_\ell(x)$ satisfies Eq. (96) in the lead regions with $V(x) = V_\ell$. Following Ref. [46], we choose matrices $A_{\ell(d)}(x)$ that allow one to project onto right and left moving states:

$$A_j(x) = \sqrt{\frac{\kappa_j}{2k_j}} \begin{pmatrix} \frac{k_j + iq}{\kappa_j} e^{-ik_j x} & \frac{-k_j + iq}{\kappa_j} e^{ik_j x} \\ e^{-ik_j x} & e^{ik_j x} \end{pmatrix}, \tag{97}$$

where $j = \{\ell, d\}$ and $k_j^2 = \kappa_j^2 - q^2$ with $\kappa_j = V_j / v_{\rm F}$.

The transfer matrix in the evanescent regions, where the electric potential vanishes, is $M_e(x, x') = \exp\left[q\sigma_z (x - x')\right]$. The transfer matrix through a single sequence consisting of a region at the Dirac point followed by a doped segment is then given by $M_1(L + \lambda, 0) = M_e(L + \lambda, \lambda)M_d(\lambda, 0)$. The transfer matrix for p doped-evanescent segments in series, contacted at either end by ideal leads, is found using M_1 and the matrices A_ℓ of Eq. (97) as

$$M_p(x, x') = A_\ell(x)A_\ell^{-1}\left(pL + p\lambda\right)\left[M_1\left(L + \lambda, 0\right)\right]^p A_\ell(0)A_\ell^{-1}(x') \tag{98}$$

at $x > p(L + \lambda)$ and $x' < 0$.

From the asymptotic form of $M_p(x,x')$ in the leads, one extracts the transmission amplitudes through the entire array, as explained in Ref. [46]: $T^{(p)} = 1/\left|\alpha\right|^2$, where

$$\begin{pmatrix} \alpha & \beta^* \\ \beta & \alpha^* \end{pmatrix} = \lim_{x\to\infty} A_\ell^{-1}(x) M_p(x,-x) A_\ell(-x), \tag{99}$$

where $|\alpha|^2 - |\beta|^2 = 1$ due to current conservation. With Eq. (98), this matrix becomes

$$\begin{pmatrix} \alpha & \beta^* \\ \beta & \alpha^* \end{pmatrix} = A_\ell^{-1}(p(L+\lambda)) \left[M_1(L+\lambda,0)\right]^p A_\ell(0). \tag{100}$$

The transmission probability $T_n^{(p)}$ of mode n is obtained by setting $q = q_n$ in the above equations, and we find

$$T_n^{(p)} = \frac{2\Delta^2(n)}{\left[\cosh^2(n\mathcal{L}) - 1\right]\cosh\left[2p\cdot\operatorname{arcsinh}\left(\Delta(n)\right)\right] + \left[\cos\left(2k_d(n)\lambda\right)\cosh^2(n\mathcal{L}) - 1\right]}. \tag{101}$$

Here, $\Delta(n) = \sqrt{\cos^2\left[k_d(n)\lambda\right]\cosh^2(n\mathcal{L}) - 1}$. As previously mentioned, the transmission probability becomes independent of the lead potential in the limit $\kappa_\ell, \kappa_d \gg 1/L$ that we have assumed. In the special case of $p = 2$, this equation reduces to Eq. (65).

The Fano factor can be calculated numerically for a cascade of arbitrary length by substitution of the transmission probability Eq. (101) into the integrals I_1 and I_2 of Eq. (64). In the large λ limit, as considered in the previous sections, the transmission probability Eq. (101) is highly oscillatory. As p increases, the transmission probability also shows exponentially damped peak regions. For these reasons, the numerical calculation of the Fano factor must be done carefully.

First, we create lists of $I_{1(2)}(p,\lambda)$ in the limit $\lambda \gg |\kappa| L^2$ and look for regions where the integrals have reached their limiting behavior for each p. The integrals are then averaged over these λ values in order to obtain the large λ limit of the Fano factor. Hence, for fixed p, the Fano factor $F[p]$ and its standard deviation $\Delta F[p]$ are found numerically from the λ averaged integrals $\langle I_{1(2)}\rangle$ and their standard deviations $\Delta I_{1(2)}$

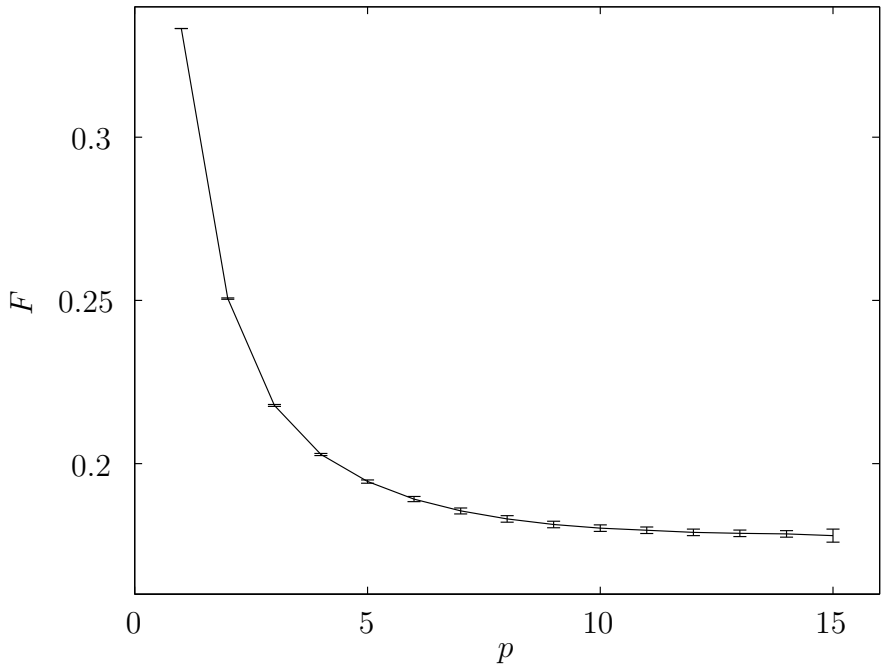

Figure 12: Fano factor for a graphene superlattice, as pictured in Fig. 11, as a function of p, the length of the cascade. The curve is calculated from the transmission probability given in Eq. (101) with $\lambda = 10|\kappa_d|L^2$. The Fano factor starts at its maximum value of 1/3 for a single graphene strip, as considered by Tworzydło *et al.* [167] In the long superlattice limit, $p \to \infty$, the Fano factor approaches 0.180..., in agreement with our analytic calculations. The error bars are caused by errors in the numerical integration.

according to

$$F[p] = \frac{\langle I_2 \rangle}{\langle I_1 \rangle}$$
$$\Delta F[p] = \sqrt{\left(\frac{\Delta I_2}{I_1}\right)^2 + \left(\frac{I_2 \Delta I_1}{I_1^2}\right)^2}. \tag{102}$$

The results are plotted as a function of the cascade size p in Fig. 12 with error bars as in Eq. (102). The Fano factor decreases rapidly from its maximum value of 0.333... for $p = 1$ and approaches 0.180... as $p \to \infty$. We next compute the exact value of F in this limit $p \to \infty$ of a long superlattice, again assuming $\lambda \gg |\kappa_d|\, L^2$.

4.2.2 The long superlattice limit

The transmission probability $T_n^{(p)}$ of Eq. (101) is plotted as a function of mode index n for various values of λ and p in Fig. 13. One observes a series of peaks in $T_n^{(p)}$, whose number increases with $\lambda/\left|\kappa_d\right| L^2$, as illustrated in the first row of plots in Fig. 13. The peaks occur at values of n where Δ is imaginary, and $T_n^{(p)}$ is exponentially damped whenever Δ is a real number.

When Δ is imaginary, the second hyperbolic cosine in the denominator of $T_n^{(p)}$ oscillates with a frequency proportional to p, the number of graphene segments in the cascade. Therefore, $T_n^{(p)}$ has a series of "sub-peaks" in the regions of imaginary Δ, whose number increases with p, as illustrated in the second row of plots in Fig. 13. We further observe in the second row of Fig. 13 that the damping to the sides of the regions with imaginary Δ is enhanced as p increases. This is also due to the factor of p in the second hyperbolic cosine function of Eq. (101).

Motivated by the above observations, we partition the wave numbers into a series of peak regions where Δ is imaginary. The length of these regions is on the order of $\Delta n(n_\lambda)$ in Eq. (68). Each peak region is then sub-partitioned into sub-peak regions, with a length that corresponds to the oscillation period of the second hyperbolic cosine of Eq. (101) at imaginary Δ. That length is of the order $\Delta n_p(n_p) \sim \Delta n(n_p)/p$. Fig. 14 illustrates both periods of oscillation, showing the transmission probability Eq. (101) for $p = 4$ with doped region thickness $\lambda = 4\left|\kappa_d\right| L^2$.

In order to calculate the Fano factor for a long graphene superlattice ($p \gg 1$), we first integrate I_1 and I_2 of Eq. (64) for each peak region $\Delta n_\lambda(n_\lambda)$ over all sub-peak regions $\Delta n_p(n_p)$. The result is then summed over the peak region $\Delta n_\lambda(n_\lambda)$ by a second integration, resulting in the desired integral over one peak region. Finally, in the limit $\lambda \gg \left|\kappa_d\right| L^2$, the peak spacing becomes small compared to the decay scale of the transmission probability, set by $\mathcal{L}$, and the full integral can be found by further summing the single peak result over all such peaks, amounting to a third integration.

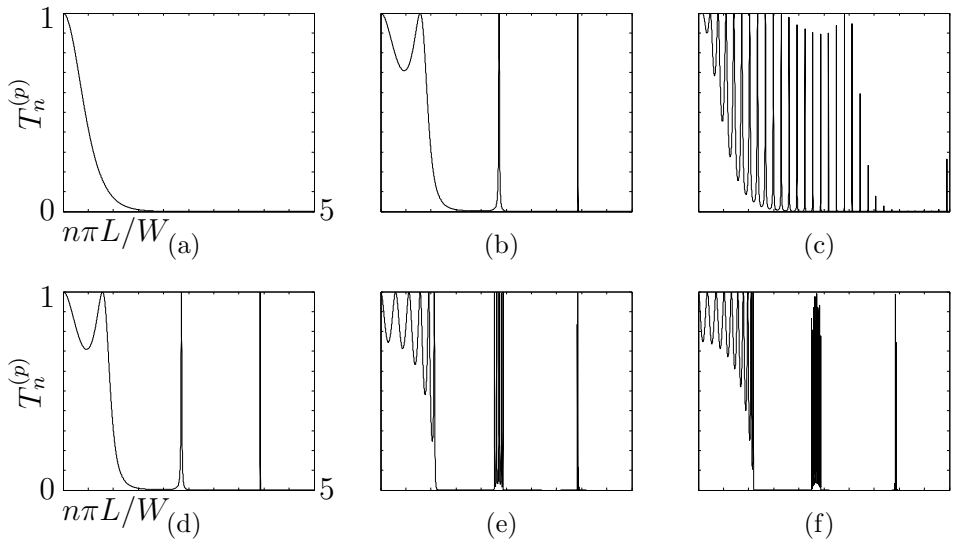

Figure 13: Plots of the transmission probability Eq. (101) as a function of mode index n. The cascade size is $p = 2$ in the first row of plots, while the doped region thickness takes the increasing values $\lambda = 0.01\,|\kappa_d|\,L^2$ (a), $\lambda = 2\,|\kappa_d|\,L^2$ (b) and $\lambda = 20\,|\kappa_d|\,L^2$ (c). Larger thicknesses lead to a higher frequency of peaks in the transmission probability. In the second row, the doped region thickness is $\lambda = 2\,|\kappa_d|\,L^2$, and the increasing cascade sizes $p = 2$ (a), $p = 6$ (b), and $p = 10$ (c) cause an increasing frequency of the sub-peak oscillations and strong damping outside of the peak regions.

4.2.3 Analytic results

Motivated by the previous analysis, we calculate the integral I_1 by averaging the transmission probability of Eq. (101) over one oscillation of $\cos(k_d\lambda)$. This result is then integrated over each oscillation within a given peak region. Finally, this result is integrated over all peak regions. We write

$$I_1 \approx \int_0^\infty dx \int_{\Delta\in\Im} dn_0 \langle T_n^{(p)} \rangle, \tag{103}$$

where $\langle\cdot\rangle$ denotes the average over one oscillation of the cosine function and x and n_0 are dummy variables whose significance is described below. This expression generalizes easily to I_2.

To begin, we fix our attention on one peak of $T_n^{(p)}$. For large λ, the period of the cosine function in Eq. (101) is small, and we linearize about a point $\tilde{n}$ within one

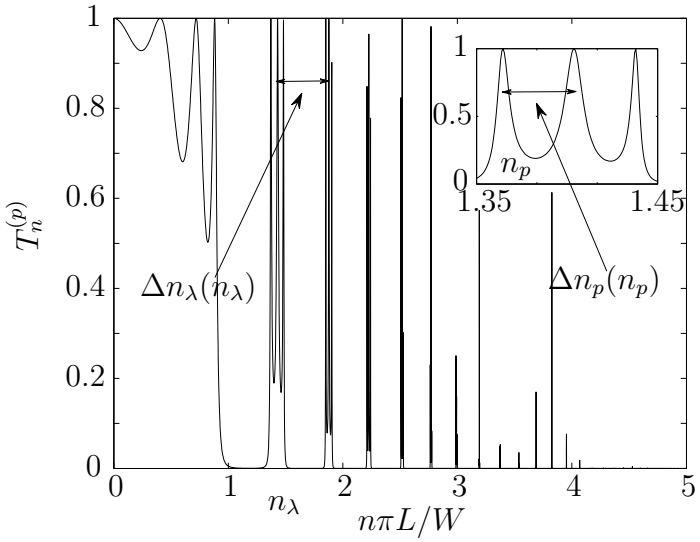

Figure 14: Transmission probability Eq. (101) as a function of mode index n for $p = 4$ and $\lambda = 4\,|\kappa_d|\,L^2$, showing peak oscillations with frequency set by λ and sub-peak oscillations with frequency set by $p\lambda$. The first peak region to the right of the central region, indexed by n_λ, is shown magnified in the inset. The peak period is given by $\Delta n_\lambda(n_\lambda)$ in the neighborhood of peak n_λ, while the period of sub-peak oscillation is $\Delta n_p(n_p)$, around peaks indexed by n_p. Both periods become infinitesimal in the limit $p \gg 1$ with $\lambda \gg |\kappa_d|\,L^2$.

period, where

$$\begin{aligned}\lambda k_d(n) &= \delta(\tilde{n}) - \omega(\tilde{n})n \\ \delta(\tilde{n}) &= \kappa_d\lambda\left(1 + \frac{\tilde{n}^2\pi^2}{2\kappa_d^2 W^2}\right) \\ \omega(\tilde{n}) &= \frac{2\pi^2\lambda\tilde{n}}{\kappa_d W^2}.\end{aligned} \tag{104}$$

The parameter $\tilde{n}$ will drop out of the calculation in the continuum limit. Because the cosine term oscillates rapidly compared to the decay scale of the $\cosh(n\mathcal{L})$ term in Δ, we approximate the hyperbolic cosine as approximately a constant $\cosh(x\mathcal{L})$ for some x in the neighborhood of the peak region in question. In the peak regions, Δ is imaginary, and hence the peak region size is determined by

$$\Delta^2(n,x) \equiv \cos^2(\delta - \omega n)\cosh^2(x\mathcal{L}) - 1 \leq 0. \tag{105}$$

Hence, the peak region in the neighborhood of x is defined by

$$n \in \left(\frac{\delta + \theta - \pi}{\omega}, \frac{\delta - \theta}{\omega} \right)$$
$$\theta = \arccos\left(\frac{1}{\cosh x\mathcal{L}} \right). \tag{106}$$

In order to make analytic progress, we linearize the $\operatorname{arcsinh}(\Delta)$ term in Eq. (101) about a point n_0 in the sub-peak region within the period of $\cos k_d\lambda$. Recalling that Δ is imaginary within the peak region, we write

$$p \cdot \operatorname{arcsinh}(\Delta) = ip \cdot \operatorname{arcsinh}\left(\sqrt{1 - \cos^2\left(k(n)\lambda\right)\cosh^2(x\mathcal{L})} \right)$$
$$\approx a(n_0) - b(n_0)n, \tag{107}$$

where

$$a(n_0) = p \cdot \operatorname{arcsinh}\left(\sqrt{1 - \cos^2\left(k(n_0)\lambda\right)\cosh^2(x\mathcal{L})} \right) + bn_0$$
$$b(n_0) = -p\frac{d}{dn} \operatorname{arcsinh}\left(\sqrt{1 - \cos^2\left(k(n)\lambda\right)\cosh^2(x\mathcal{L})} \right)\Bigg|_{n=n_0}. \tag{108}$$

Within the sub-peak region in the neighborhood of x, the transmission probability is then given approximately by

$$T_n^{(p)} \approx \frac{2\Delta^2(n_0, x)}{\left[\Delta^2(n_0, x) + \sin^2\left(k(n_0)\lambda\right)\right]\cos\left(a - bn\right) + \left[\Delta^2(n_0, x) - \sin^2\left(k(n_0)\lambda\right)\right]}. \tag{109}$$

The average of Eq. (109) over one period is of the form

$$\langle T_n^{(p)} \rangle = \frac{1}{2\pi}\int_{-\pi}^{\pi} \frac{C}{A\cos u + B} du, \tag{110}$$

where

$$A = \Delta^2(n_0, x) + \sin^2\left(\delta - \omega n\right)$$
$$B = \Delta^2(n_0, x) - \sin^2\left(\delta - \omega n\right)$$
$$C = 2\Delta^2(n_0, x). \tag{111}$$

This integral can be computed using the integral of Eq. (71) when $|A/B| < 1$. This requirement is satisfied within a peak region where $\Delta^2(n_0, x) < 0$, since

$$\left|\frac{A}{B}\right| = \left|\frac{\sin^2(\delta - \omega n) + \Delta^2(n_0, x)}{\sin^2(\delta - \omega n) - \Delta^2(n_0, x)}\right| < 1. \tag{112}$$

Using Eq. (71), the average over each period of the transmission probability is given by

$$\langle T_n^{(p)} \rangle = \frac{\sqrt{1 - \cos^2(\delta - \omega n_0)\cosh^2(x\mathcal{L})}}{\sin(\delta - \omega n_0)} \tag{113}$$

Similarly, for I_2, we find that the average of $\left(T_n^{(p)}\right)^2$ is of the form

$$\langle \left(T_n^{(p)}\right)^2 \rangle = \frac{1}{2\pi} \int_{-\pi}^{\pi} \frac{C^2}{(A\cos u + B)^2} du, \tag{114}$$

and we have

$$\langle \left(T_n^{(p)}\right)^2 \rangle = \frac{1}{2}\left[\langle T_n^{(p)} \rangle + \frac{\left(1 - \cos^2(\delta - \omega n_0)\cosh^2(x\mathcal{L})\right)^{3/2}}{\sin^2(\delta - \omega n_0)}\right] \tag{115}$$

Using Eq. (106) for the length of the peak region, the approximation of I_1 now takes the form

$$I_1 \approx \int_0^{\infty} dx \int_{\theta}^{\pi-\theta} du \frac{\sqrt{1 - \cos^2 u \cosh^2 x\mathcal{L}}}{\sin u \cosh x\mathcal{L}}, \tag{116}$$

where $\theta = \arccos(1/\cosh x\mathcal{L}) \in (0, \pi/2)$ and $u = \delta - \omega n_0$. Similarly, I_2 is approximately

$$I_2 \approx \frac{1}{2}\int_0^{\infty} dx \int_{\theta}^{\pi-\theta} du \left[\frac{\sqrt{1 - \cos^2 u \cosh^2 x\mathcal{L}}}{\sin u \cosh x\mathcal{L}} + \frac{\left(1 - \cos^2 u \cosh^2 x\mathcal{L}\right)^{3/2}}{\sin u \cosh x\mathcal{L}}\right]. \tag{117}$$

All of the above integration steps can be performed analytically, giving the exact Fano factor $F = 1/(8\ln 2)$ in the limit $p \to \infty$ with $\lambda/|\kappa_d| L^2 \to \infty$. This result is in agreement with the numerical results plotted in Fig. 12, and it differs from the Fano factor calculated for the geometry of section 4.1, as well as the calculations of Tworzydło *et al.* [167] The shot noise for transport through a graphene superlattice as depicted in Fig. 11 thus provides another unambiguous signature of evanescent mode transport.

4.3 Discussion and Conclusions

Throughout this chapter, we have assumed translational invariance in the y-direction. We now briefly discuss the sensitivity of our results to a breaking of that symmetry before summarizing. As a typical mechanism for such symmetry breaking, we consider a gate edge which makes a non-zero angle $\Delta\phi$ with the vertical. At such an interface, transverse modes are mixed. Electrons with momentum $k_x \sim \kappa_d = V_d/v_{\rm F}$ in the $\hat{x}$-direction increase their momentum in the $\hat{y}$-direction by an amount $\Delta q \approx \kappa_d \Delta\phi$ as they traverse such an edge.

To avoid qualitatively changing the above calculations, this momentum shift must be small on the scale $\kappa_d/p\lambda q$ of the oscillations of the transmission probability, requiring $\Delta\phi \ll 1/p\lambda q$. Noting that the typical momenta contributing to the Fano factor in our calculation are of order $q \simeq 1/L$, this results in the condition

$$\Delta\phi \ll L/p\lambda. \tag{118}$$

In addition, we have assumed $\lambda \gg |\kappa_d|\, L^2$ in all of our analytical calculations. These results therefore require

$$1 \ll |\kappa_d|\, L \ll \frac{\lambda}{L} \ll \frac{1}{p\Delta\phi} \tag{119}$$

in setups with angular imperfections.

In conclusion, we have proposed several experimental geometries for which the shot noise provides an unambiguous signature of transport through evanescent modes at the Dirac point of graphene. For the case of two gated graphene strips in series, separated by a long highly doped region, the Fano factor can be controlled through either spatial asymmetry or the gate potentials. In particular, the Fano factor has a universal minimum of $F = 1/4$ for the spatially symmetric case with both gated regions tuned to the Dirac point. This result differs from the value $F = 1/3$ expected for transport through a disordered metal, which allows for a particularly conclusive experimental investigation of evanescent mode transport in graphene. For the case

of a long superlattice of evanescent regions, we predict another universal value of the Fano factor, $F = 1/(8 \ln 2)$.

CHAPTER V

DEPENDENCE OF THE FANO FACTOR ON THE CHEMICAL POTENTIAL IN GRAPHENE NANO-RIBBONS

In the experiment of Danneau *et al.*, [50] the Fano factor reached a peak value $F \sim 1/3$ and displayed a strong dependence on the chemical potential. This provides evidence for evanescent wave transport; as the chemical potential departs from the Dirac point, states that are evanescent at the Dirac point become propagating, which decreases backscattering and hence the Fano factor. This would not be the case if the observed shot noise was caused by impurities. However, the energy scale of the measured dependence of the Fano factor on the chemical potential was considerably larger than theory predicts. [167] As the dependence of F on the chemical potential provides the main experimental evidence for evanescent wave transport in graphene to date, this deviation from the theoretical prediction is disturbing.

In this chapter, we show that the measured dependence of the Fano factor on the chemical potential is consistent with the assumption that it originates from evanescent waves when the effects of the electrical contacts are accounted for. It has been shown by first-principles calculations that contacts to graphene have two main effects on electron transport: doping of the pieces of graphene underneath the contacts and electron scattering at the interface from contact to graphene. It turns out that the Ti-graphene contacts used in the experiment of Ref. [50] are highly transparent at low energies, [16] such as those in the experiment. We therefore neglect contact scattering at the low energies relevant to the experiment, and focus on the effects of doping through the contacts.

While the theory of Ref. [167] assumes a constant potential, local doping of the graphene underneath the contacts results in a space-dependent electric potential. We show that the space dependence of the electric potential results in an increase of the voltage scale of the Fano factor. This effect can be understood in terms of an effective reduction of the length of the graphene ribbon to a region around the potential minimum. This results in an increased voltage scale for the response of the conduction electrons to an electric potential, which is set by the level spacing in the ribbon. This correction is inversely proportional to the reduced length. Remarkably, the maximum of the Fano factor remains $F = 1/3$ when the space dependence of the potential caused by doping through the contacts is taken in to account, in agreement with the experiment of Danneau *et al.* [50] This calculation thus lends additional support to an interpretation of the experiment of Ref. [50] in terms of evanescent waves in graphene.

We calculate the Fano factor as a function of the gate voltage for a graphene nanoribbon as follows: in Sec. 5.1, we employ a conformal map technique to calculate the potential in the graphene ribbon, neglecting screening from the conduction electrons. We then identify a regime where such screening is negligible. We use the resulting potential in Sec. 5.2 to calculate the transmission through the GNR. In order to understand the physics of the voltage scale increase of the Fano factor, we first identify limits where this calculation can be done analytically. In Sec. 5.3, we calculate the transmission numerically from the wave functions, also finding good agreement with experimental observations when our analytic approach fails. We conclude with a summary in Sec. 5.4.

5.1 Calculation of the potential

In this section, we introduce the system geometry and employ a conformal map technique in order to calculate the potential on the GNR, neglecting the graphene

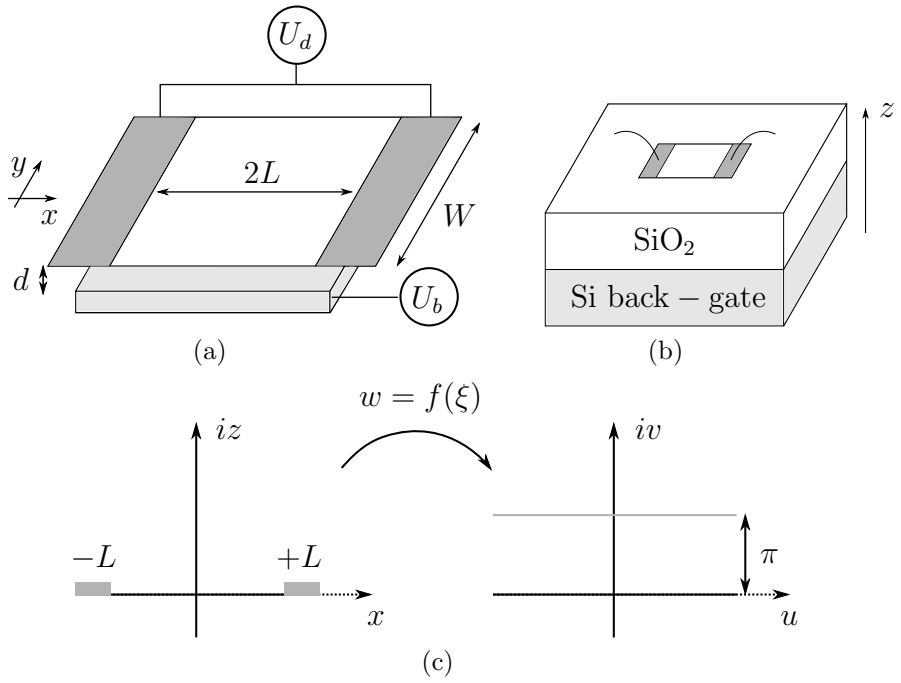

Figure 15: (a) Graphene nano-ribbon geometry consisting of a graphene sheet with lead regions (dark gray rectangles) separated by an undoped region (white rectangle). An insulating SiO_2 layer of thickness d (not shown) separates the graphene sheet from a Si back-gate (light gray rectangle). (b) An example of simplified experimental geometry as considered in Ref. [50]. (c) For the $d = 0$ case, the conformal map $w = f(\xi)$ maps the (x, iz) plane to the (u, iv) plane. The undoped graphene regions are sent to the real line $v = 0$ while the doped graphene regions are sent to the line $v = \pi$. The height of the doped lead regions shown here is for illustration purposes and has no physical meaning.

conduction electrons. We then identify a regime where such screening is negligible.

In the experiment of Danneau *et al.*, [50] a graphene nano ribbon (GNR) was mechanically exfoliated, deposited on a Si/SiO_2 substrate as in Fig. 15b, and brought in close contact with Ti contacts. An insulating SiO_2 layer of thickness $d \simeq 300$ nm separated the graphene from a Si back-gate. We assume that the electronic structure of the sections of the ribbon underneath the contacts is unmodified, except for doping through the contacts. It has been shown using density-functional calculations that this model is a good approximation for non-wetting contacts [17] and also for (wetting) Ti contacts at low energies. [16]

5.1.1 Model

To find the electric potential U on the GNR, we model the system by two metallic half-planes separated by a distance $2L$, representing the contacts, and a third metallic plane, representing the Si back-gate, at distance d below the GNR, as shown in Fig. 15a. All metals are assumed to be perfect, and hence equipotentials, and we choose coordinates such that the contact edges are along the y-direction and at $x = \pm L$. The z axis is perpendicular to the back-gate and GNR.

In equilibrium, the contact plates are at identical electric potentials U_d, while the back-gate has a potential U_b. Under the reasonable assumption that the distance between the contacts and the GNR is negligible, U_d is also the electrostatic potential in the graphene regions underneath the contacts. In the absence of a back-gate and in the limits that we take below, the potential on the ribbon close to the center of the GNR differs from U_d by the work function difference between the GNR and the metal contacts. The back-gate is used to manipulate the potential in this region where, in the same limits, all electron scattering occurs.

We employ a low-energy Dirac model of the electron dynamics in the GNR with $\hbar = 1$,

$$H_\gamma = v_{\rm F}\vec{\sigma}_\gamma \cdot \vec{p} + V(x), \tag{120}$$

where $\vec{\sigma}_\gamma = (\gamma\sigma_x, \sigma_y)$ is a vector of Pauli matrices with the valley index $\gamma = \pm 1$, $\vec{p} = -i\vec{\nabla}$ is the electron momentum and $v_{\rm F}$ is the electron velocity. The potential energy of electrons on the GNR is given in terms of the electric potential U by $V(x) = -eU(x)$. Using translational invariance in the $\hat{y}$-direction and choosing boundary conditions that do not mix transverse modes, [22, 30] the momentum q along the $\hat{y}$-direction is conserved, and the scattering problem becomes one dimensional:

$$H_\gamma = v_{\rm F}(-i\gamma\sigma_x\partial_x + q\sigma_y) + V(x). \tag{121}$$

We focus on the most interesting regime of the Fano factor measurement of Danneau *et al.*, [50] namely an interval $I_{\rm D}$ of chemical potentials $-V(0)$ in the middle of the GNR with width $\Delta\mu$. The Fano factor reaches its maximum $F \approx 1/3$ at the center of this interval, and decays monotonically to a value $F < 0.25$ at the boundaries. Existing theory [167] assumes a piecewise constant shape of V, with $V = V_\infty \gg v_{\rm F}/L$ underneath the contacts and $V = V_0$ in between. This potential shape is obtained from our electrostatic model in the limit $d \to 0$. In that case, $V(0) = V_0 = -eU_b$ between the contacts, and the propagating electron states oscillate with a spatial period on the order of $v_{\rm F}/eU_b$.

Such theory predicts oscillations of the Fano factor with period $\Delta\mu \simeq v_{\rm F}/L$. In the experiment, [50] however, the interval $I_{\rm D}$ was found to be at least a factor of 2 larger than this prediction. In the experiment, $d \neq 0$, and the electrostatic model of Ref. [167] is oversimplified. Below, we analyze the effects of nonzero distance d between the GNR and the back-gate, assuming that d is small in a sense that will be specified. In that case, one still has $V(0) \approx -eU_b$, but the potential V is no longer piecewise constant. We show below that such non-zero d resolves the discrepancy between theory and experiment. The gate voltage dependence of the Fano factor measured by Danneau *et al.* [50] is plotted in Fig. 16.

5.1.2 The conformal map

We begin our calculation with the electrostatic potential $U(x)$ on the GNR. In a first approximation, we neglect doping of the GNR, effectively assuming it is a perfect insulator. We will justify this approximation for small d in the following section. Additionally, assuming that the contacts lie directly on top of the GNR and that the distance d to the back-gate is small compared to the length L of the ribbon, $d \ll L$, we find the potential U on the GNR to a good approximation (at distance $\Delta x \gg d$

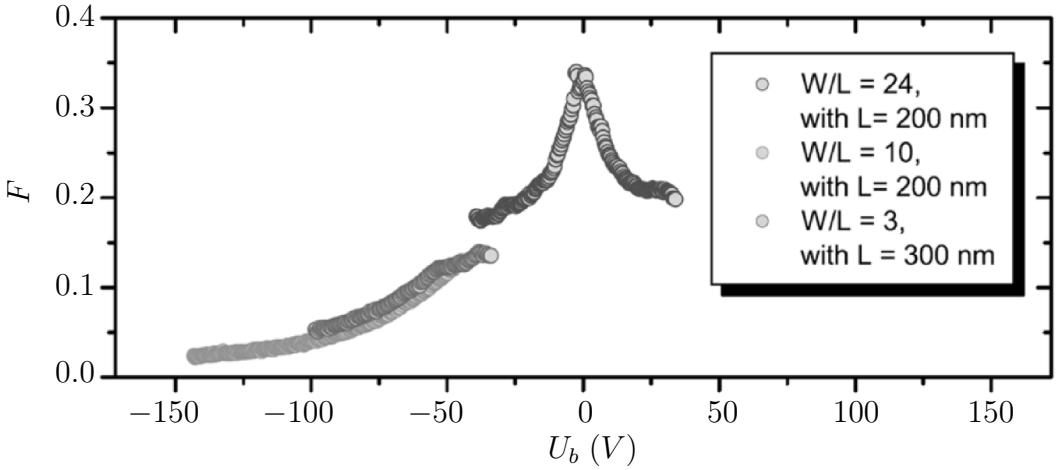

Figure 16: The Fano factor as a function of gate voltage measured by Danneau *et al.* [50] for three different samples with $|U_b - U_d| = 40$ mV. Two of the three samples are unintentionally p-doped, shifting the Dirac point (Adapted from Danneau *et al.* [50]).

from the contacts) from the electric field $\vec{E}_0$ on the ribbon when $d = 0$:

$$U_0 = U_b + \hat{z} \cdot \vec{E}_0 d/\epsilon_r, \tag{122}$$

where $\epsilon_r \approx 3.9$ [73] is the relative electric permittivity of the SiO_2 layer separating the GNR from the back-gate. The permittivity can be written $\epsilon_r = \epsilon/\epsilon_0$, where ϵ_0 is the vacuum permittivity and ϵ is the permittivity of silicon oxide.

The electric field $\vec{E}_0$ at $d = 0$ may be found by an appropriate conformal mapping, exploiting translational invariance in the direction along the contact edges. The electric potential U satisfies the two-dimensional Laplace equation $\nabla^2 U(x, z) = 0$, along with the boundary conditions

$$\begin{aligned} U(|x| > L, z = 0) &= U_d, \\ U(|x| < L, z = 0) &= U_b. \end{aligned} \tag{123}$$

The conformal map

$$\begin{aligned} f(\xi) &= \ln\left(\frac{\xi - L}{\xi + L}\right) \\ &= \ln\left|\frac{\xi - L}{\xi + L}\right| + i\mathrm{Arg}\left(\frac{\xi - L}{\xi + L}\right) \end{aligned} \tag{124}$$

from the complex plane $\xi = (x, iz)$ into the complex plane $w = (u, iv)$ maps these boundary conditions onto those of a parallel plate capacitor, with a plate separation of π, as shown in Fig. 15c. When $z \to 0$, the map $f(\xi)$ sends the graphene regions under the contacts at $|x| > L$ in the ξ-complex plane to the real line $v = 0$ in the w-complex plane. Similarly, for $z \to 0$, the region $|x| < L$ in the ξ-plane is mapped to the line $v = \pi$ in the w-plane.

The potential in the (u, iv) plane is thus

$$U(u, v) = \frac{(U_b - U_d)v}{\pi} \propto \operatorname{Im} w. \tag{125}$$

For any complex number ξ, we have

$$\frac{\xi - L}{\xi + L} = \frac{(\xi - L)(\xi^* + L)}{|\xi + L|^2} = \frac{|\xi|^2 - L^2 + 2iL \operatorname{Im} \xi}{|\xi + L|^2}, \tag{126}$$

where ξ^* denotes the complex conjugate of ξ. Furthermore, we have

$$\operatorname{Arg}(\xi) = \tan^{-1}\left(\frac{\operatorname{Im} \xi}{\operatorname{Re} \xi}\right). \tag{127}$$

In the (x, iz) plane, the conformal map satisfies

$$\operatorname{Arg}\left(\frac{\xi - L}{\xi + L}\right) = \tan^{-1}\left(\frac{2zL}{x^2 + z^2 - L^2}\right). \tag{128}$$

Under the map Eq. (124), Eq. (125) thus gives the electric potential

$$U(x, z) = \frac{U_b - U_d}{2\pi} \tan^{-1}\left(\frac{2zL}{x^2 + z^2 - L^2}\right) + U_b \tag{129}$$

in the original (x, iz) plane.

It is easily seen that the solution of Eq. (129) satisfies the Laplace equation. To see that it also satisfies the boundary conditions Eq. (123), first suppose that $|x| > L$. As $z \to 0$, the argument of the inverse tangent in Eq. (129) approaches zero from the positive side. Hence, the inverse tangent function vanishes in this case, satisfying the boundary conditions in the doped graphene regions. When $|x| < L$ with $z \to 0$, the argument of the inverse tangent approaches zero from the negative side, and hence

the inverse tangent approaches 2π, satisfying the boundary condition in the undoped regions.

By differentiation, we now find the electric field $\vec{E}_0$ on the graphene sheet for $d = 0$ from Eq. (129) and, using Eq. (122), we obtain the electric potential on the ribbon at $d \ll L$ and $L - |x| \gg d$ as

$$\begin{aligned} U_0(x) &= U_b + \hat{z} \cdot \vec{E}_0(x,0) d/\epsilon_r \\ &= U_b + \frac{U_b - U_d}{\epsilon_r \pi \left(1 - x^2/L^2\right)} \left(\frac{d}{L}\right). \end{aligned} \tag{130}$$

5.1.3 Corrections due to screening by the graphene sheet

Next, we account for the screening of the electric potential generated by the contacts arising from the electrons in the ribbon itself. Quantifying this screening requires a determination of the electron density $n(x)$ that accumulates on the ribbon due to the potential $V(x)$. The corresponding charge density $-en$ induces a screening electric field $\vec{E}_{sc}$, which in turn modifies the potential V on the ribbon. Under our assumption $d \ll L$, we have

$$V(x) = eU_b + e\left\{\hat{z} \cdot [\vec{E}_0(x,0) + \vec{E}_{sc}(x,0)]d\right\}/\epsilon_r, \tag{131}$$

and $\vec{E}_{sc}$ is approximately given by Gauss' law:

$$\hat{z} \cdot \vec{E}_{sc}(x,0) = -\frac{en}{\epsilon_0}. \tag{132}$$

A determination of the density

$$n(x) = \sum_{q,\varepsilon<0} |\psi_{q,\varepsilon}(x)|^2 \tag{133}$$

requires the wave functions $\psi_{q,\varepsilon}(x)$. Rather than carrying out the requisite quantum mechanical calculation, we identify [176] a parameter regime where the screening field E_{sc} may be neglected, $E_{sc} \ll E_0$. The key observation allowing this approximation is that the induced electron density n is space dependent for $d = 0$, since $V(x)$ is

at $|x| < L$. One thus expects that the effects of screening may also be neglected for non-zero d below a critical distance d_c. In Ref. [176] we establish the existence of such a critical distance and we compute d_c. We find

$$d_c = \epsilon_r v_{\mathrm{F}} \hbar (\epsilon_0 L)^{3/4} e^{-7/4} (U_b - U_d)^{-1/4}. \tag{134}$$

For the remainder of this article we assume that $d \ll d_c \ll L$. In that regime we have, to a good approximation, $V(x) = -eU_0(x)$ and $V(0) = -eU_b$.

5.2 Transport calculations

In order to calculate the q-dependent transmission probabilities for transport through a GNR as in Fig. 15a, we employ the transfer matrix method, as in Chp. 4. Assuming translational invariance in the $\hat{y}$-direction and choosing boundary conditions that do not mix modes at the doped-undoped region interfaces, the momentum q along the $\hat{y}$-direction is conserved and the scattering problem is one dimensional, as described by the Hamiltonian Eq. (121). We restrict the analysis to one valley with index $\gamma = +1$ and energy equal to the chemical potential $\mu = 0$. The transfer matrix $M(x, x')$ for the requisite Dirac spinors of a mode with transverse momentum q satisfies the equation

$$i\partial_x M(x, x') = \left[iq\sigma_z + \frac{V(x)}{v_{\mathrm{F}}} \sigma_x \right] M(x, x'). \tag{135}$$

5.2.1 Analytic calculation of transmission probability

In parts of the central graphene region with potential Eq. (130), transport is semi-classical and the transfer matrix can be found using an adiabatic approximation. This is the case whenever [46] $qV'/V(V^2/v_{\mathrm{F}}^2 - q^2) \ll 1$. Loosely speaking, this condition is met where the potential is large, such as near the contacts. It has been shown in Ref. [46] that no electron scattering takes place in those regions. All shot noise is therefore produced in the regions that do not allow such an approximation, near the classical turning points where $V = \pm v_{\mathrm{F}} q$.

As previously mentioned, we assume that the regions of interest, where electron scattering occurs, are at $|x| \ll L$. The precise form of the potential at $|x| \simeq L$ is thus irrelevant, and we may approximate the potential Eq. (130) quadratically,[1]

$$V(x) = \gamma x^2 - V_b, \tag{136}$$

where $\gamma = e(U_d - U_b)d/\epsilon_r \pi L^3$ and $V_b = eU_b$ is set by the back-gate voltage U_b. To make analytical progress, we assume $|V_b| \gg v_{\mathrm{F}}^{2/3}\gamma^{1/3}$. While this is not the most relevant limit experimentally, this calculation will provide physical insight into the transport problem.

Our analytical approach decomposes the GNR into "adiabatic regions," where the semi-classical approximation may be applied, and "non-adiabatic regions" near the classical turning points $V = \pm v_{\mathrm{F}} q$, where it cannot. One finds that for $|V_b| \gg v_{\mathrm{F}}^{2/3}\gamma^{1/3}$, each non-adiabatic region is short enough for the potential to allow linearization throughout the region. The transfer matrix for a linear potential has been found exactly in Ref. [46]. This, together with the adiabatic solution for the remaining regions and the composition rule $M(x, x') = M(x, x'')M(x'', x')$, allows us to construct the transfer matrix through the entire GNR.

We find the above condition $|V_b| \gg v_{\mathrm{F}}^{2/3}\gamma^{1/3}$ for applicability of the described analytical approach by self-consistently assuming that the potential V may be linearized in the non adiabatic regions. It has been shown [46] that, in this case, transport through a non-adiabatic region around a pair of classical turning points $V = \pm v_{\mathrm{F}} q$ is exponentially suppressed by a factor $\exp(-\pi v_{\mathrm{F}} q^2/V')$. Thus, only modes with $q \lesssim \sqrt{V'/v_{\mathrm{F}}}$ contribute significantly to transport, and we may neglect all other modes. The condition quoted above for adiabatic electron dynamics thus effectively becomes $v_{\mathrm{F}} V' \ll V^2$. Using the explicit form Eq. (136) of the potential V, we find

[1] Here we assume $\gamma > 0$. In reality, Ti contacts n-dope graphene, such that $\gamma < 0$. [16] The sign of γ, however, can be changed by a particle-hole transformation $U = \sigma_z$, and none of our conclusions depend on it.

that this condition is fulfilled everywhere except in regions of length Δx around the points x_0 with $V(x_0) = 0$ that are short enough to allow linearization of V, that is $\Delta x \ll x_0$ if $|V_b| \gg v_{\mathrm{F}}^{2/3}\gamma^{1/3}$.

In the following few subsections, we calculate transport through the GNR in this limit. Exploiting the inversion symmetry of the potential V, we may restrict our analysis to $x > 0$ and obtain the transfer matrix for $x < 0$ by symmetry. The Hamiltonian of Eq. (121) is symmetric under the operator $\mathcal{P} = \sigma_y\mathcal{R}$, where $\mathcal{R}$ denotes reflection on the line $x = 0$, such that $\mathcal{R}\psi(x) = \psi(-x)$. Therefore, from the transfer matrix M at $x, x' > 0$, one obtains the one for $-x, -x' < 0$ by $\mathcal{P}M\mathcal{P}^{-1}$. Then, from $M(x, 0)$ for $x > 0$ one finds

$$M(0, y) = \sigma_y M^{-1}(-y, 0)\sigma_y \tag{137}$$

at $y < 0$, and accordingly the transfer matrix through the entire ribbon is

$$M(x, y) = M(x, 0)M(0, y) = M(x, 0)\sigma_y M^{-1}(-y, 0)\sigma_y, \tag{138}$$

with $x > 0$ and $y < 0$.

5.2.1.1 Adiabatic (semi-classical) regions

Following the work of Cheianov and Fal'ko, [46] the transfer matrix in the adiabatic regions, where $qV'/V(V^2/v_{\mathrm{F}}^2 - q^2) \ll 1$, is found using the transformation

$$Y(x) = \frac{1}{V(x)} \begin{pmatrix} i\chi & i\chi^* \\ V(x) & V(x) \end{pmatrix}, \tag{139}$$

with $\chi = v_{\mathrm{F}}\,[q + ik(x)]$ and the longitudinal wave number $k(x) = \sqrt{[V(x)/v_{\mathrm{F}}]^2 - q^2}$. For our form of V, the transverse momentum q is negligible compared to k throughout the adiabatic regions with $qV'/V(V^2/v_{\mathrm{F}}^2 - q^2) \ll 1$, and $Y(x)$ simplifies to

$$Y_{\pm} = \begin{pmatrix} -\operatorname{sgn} V & \operatorname{sgn} V \\ 1 & 1 \end{pmatrix}, \tag{140}$$

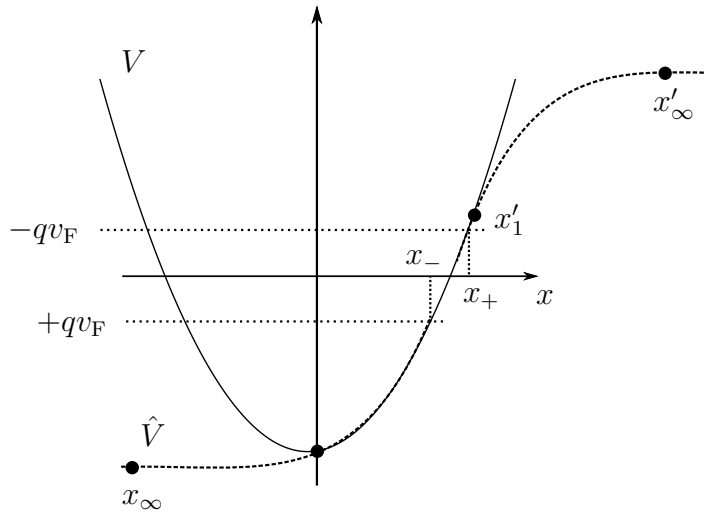

Figure 17: Plots of the quadratic potential V in the GNR (solid curve) and the asymptotically constant potential $\hat{V}$ considered by Cheianov and Fal'ko [46] (dashed curve). The two potentials coincide in the region between the points $x = 0$ and x'_1 (here, primed coordinates refer to points to the right of the origin). We define x_0 such that $V(x_0) = 0$. The classical turning points for the right side of the potential at $x_\pm = x_0 \pm \ell$ lie within the region where V can be linearized. The points x_∞ and x'_∞ are asymptotically far away from the turning points.

where $\operatorname{sgn} V$ is the sign of the potential $V(x)$. The transfer matrix for the adiabatic regions $M_\mathrm{ad}(x, y)$ is then given by

$$M_\mathrm{ad}(x, y) = Y(x)\tilde{M}_\mathrm{ad}(x, y)Y^{-1}(y), \tag{141}$$

where the matrix $\tilde{M}_\mathrm{ad}(x, y)$ satisfies the equation

$$\begin{aligned} \partial_x \tilde{M}_\mathrm{ad}(x, y) &= ik(x)\sigma_z \tilde{M}_\mathrm{ad}(x, y) + \Omega(x)\tilde{M}_\mathrm{ad}(x, y), \\ \Omega(x) = -Y^{-1}\partial_x Y &= \frac{q\partial_x V(x)}{2k^2(x)V(x)} \begin{pmatrix} -\chi & \chi^* \\ \chi & -\chi^* \end{pmatrix}. \end{aligned} \tag{142}$$

We may disregard the term proportional to Ω in Eq. (142) in the limit $|qV'/(Vk^2)| \ll 1$.

5.2.1.2 Non-adiabatic regions

The adiabatic condition $qV'/Vk^2 \ll 1$ breaks down near the turning points $x = x_0 \pm \ell$, where $k(x) = 0$, and at x_0, where $V(x_0) = 0$. We assume that the length of the entire

non-adiabatic region at $x > 0$, which includes the interval $(x_0 - \ell, x_0 + \ell)$, is small on the scale x_0 on which the potential varies, as discussed above. In this limit, we may approximate the potential $V(x)$ linearly in the non adiabatic region,

$$V(x) \approx 2\gamma x_0 (x - x_0) = 2\sqrt{V_b \gamma}(x - x_0). \tag{143}$$

Electron transport through a linear potential in graphene has an analytic solution. We use the solution formulated in Ref. [46] for potentials that may be linearized in the non-adiabatic regions and that reach asymptotic values at $|x| \to \infty$. To this end, we define an auxiliary potential $\hat{V}$ with asymptotic values at $|x| \to \infty$ and a linear region around the turning points, which coincides with the linear region of the true potential V, as in Fig. 17. Due to the assumption $|V_b| \gg v_{\mathrm{F}}^{2/3}\gamma^{1/3}$, the potential V may be linearized throughout the non adiabatic region at $x > 0$, and we may choose $\hat{V}$ to coincide with V in that entire region. The transfer matrix for a GNR with potential $\hat{V}$ is [46]

$$\begin{aligned}
\alpha &= e^{\pi\theta}, \\
\beta^* &= -e^{\pi\theta/2}\frac{\sqrt{2\pi}e^{i\pi/4}\theta^{1/2+i\theta}}{\Gamma(1+i\theta)}e^{i\varphi}, \\
\varphi &= k_F\ell - \int_\ell^\infty \left[\hat{k}(x) - k_F\right] dx, \\
\theta &= \frac{q^2 v_{\mathrm{F}}}{4\sqrt{V_b\gamma}},
\end{aligned} \tag{144}$$

where $\hat{k}(x) = \sqrt{[\hat{V}(x)/v_{\mathrm{F}}]^2 - q^2}$.

5.2.1.3 Concatenation of adiabatic and non-adiabatic regions

In order to calculate the transfer matrix for transport through the entire right side of the potential $x > 0$, we combine the transfer matrices through the adiabatic regions with the solution Eq. (144) for transport through the auxiliary potential $\hat{V}$. Without loss of generality, we choose the auxiliary potential $\hat{V}$ to coincide with the true potential V not only in the non-adiabatic region, but in the entire region extending

from the potential minimum at $x = 0$ up to the right end of the non-adiabatic region at x_1'. We obtain from Eqs. (97), (99), and (144) the transfer matrix $\hat{M}(x_\infty', x_\infty)$, where $x_\infty < 0$ and $x_\infty' > 0$ are in the asymptotic regions of constant $\hat{V}$:

$$\hat{M}(x_\infty', x_\infty) = \hat{A}_+(x_\infty') \begin{pmatrix} \alpha & \beta^* \\ \beta & \alpha^* \end{pmatrix} \hat{A}_-^{-1}(x_\infty). \tag{145}$$

To construct the transfer matrix $M(x, 0)$ from $x = 0$ through the non adiabatic region to a point $x > x_1'$ (see Fig. 17), we first perform an adiabatic transfer along $\tilde{V}$ from $x = 0$ to the point $x_\infty < 0$. We then use $\hat{M}(x_\infty', x_\infty)$ to transport in the potential $\hat{V}$ from x_∞ to a point $x_\infty' > 0$. Next, we perform another adiabatic transfer in $\hat{V}$ from x_∞' back to x_1', the right end of the non-adiabatic region, where $\tilde{V}$ and V begin to deviate. The resulting transfer matrix describes transport from 0 to x_1' in the potential $\hat{V}$. Finally, we transport adiabatically in the true potential V from this point to x, resulting in

$$M(x, 0) = M_{\rm ad}(x, x_1')\hat{M}_{\rm ad}(x_1', x_\infty')\hat{M}(x_\infty', x_\infty)\hat{M}_{\rm ad}(x_\infty, 0). \tag{146}$$

The transfer matrix $M_-(x_1', -x)$ for negative x follows from Eqs. (137) and (146).

5.2.2 Analytic results

From the transfer matrix of Eq. (146), one analytically extracts the transmission probability using Eq. (99). The resulting transmission probability takes the form

$$\begin{aligned} T &= \left|\alpha^2 + ie^{-2i\phi}\,(b^*)^2\right|^{-2}, \\ \phi &= \int_{\ell - x_0}^{x_0 - \ell} \sqrt{V^2(x)/v_{\rm F}^2 - q^2}\,dx, \end{aligned} \tag{147}$$

where $b = -\sqrt{2\pi}e^{\pi\theta/2}\theta^{1/2-i\theta}/\Gamma(1 - i\theta)$ and $V(\pm x_0) = 0$. The wave function acquires the phase ϕ from traversing the central adiabatic region separating the turning point at $x = \ell - x_0$ from the turning point at $x = x_0 - \ell$.

For a finite number of transverse modes q_n, the Fano factor is found from the transmission probabilities $T_n = T(q_n)$ of Eq. (147) according to Eq. (53). In the

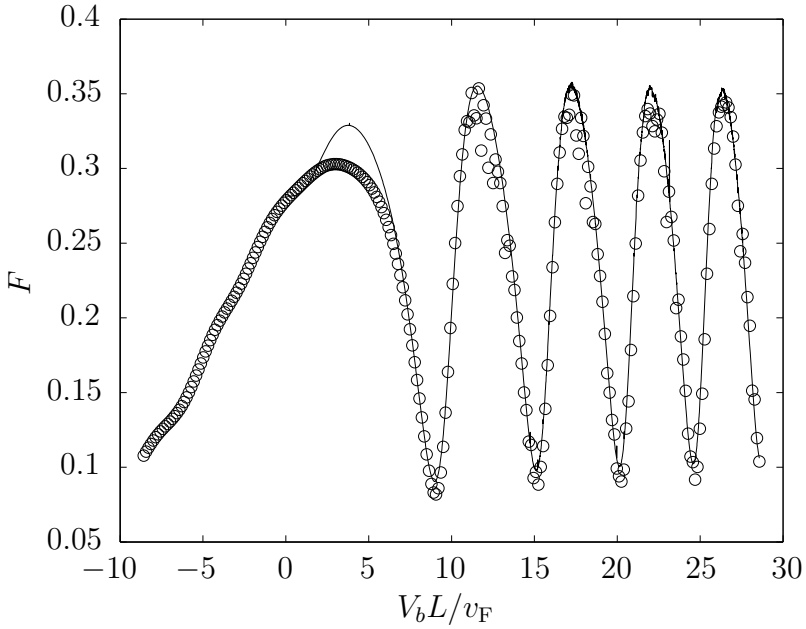

Figure 18: Analytic (solid curve) and numerical (circles) results for the Fano factor F as a function of back-gate voltage in units of v_F/L assuming $\hbar v_F = 0.7$ eV $\cdot$ m, $L = 500$ nm and $\gamma = 10^{-6}$ eV/m^2. The analytic results are calculated from the transmission probability of Eq. (147). The numerical result is calculated from the numerically integrated wave functions according to Eq. (121) and Eq. (156). The results differ at low back-gate voltages where the turning points no longer lie within the linear region of the potential and the semi-classical approximation used here breaks down.

continuum limit $W \gg L$, the sums over the mode index become integrals over the momentum q. The Fano factor is plotted as a function of the back-gate voltage in units of v_F/L in Fig. 18 (solid curve). The curve shows oscillations in gate voltage with a maximum of $F \simeq 1/3$, as predicted by the theory [167] describing evanescent mode transport in a piecewise constant potential. However, the width of the peaks is broader than predicted by the theory of Ref. [167], in agreement with the observations of Danneau *et al.* [50].

From Eq. (147), we find that the oscillations of the Fano factor predicted by our analytic calculation have period $\Delta V_b = (3\pi v_F/2)^{2/3}\gamma^{1/3}$. Substituting $\gamma = e(U_d - U_b)d/\epsilon_r \pi L^3$, the predicted oscillation period

$$\Delta V_b = \eta \Delta V_b \,|_{d=0} \tag{148}$$

is enhanced by a factor $\eta = (9e|U_b - U_d|d/4\epsilon_r v_F \pi^2)^{1/3}$ compared to the period $V_b|_{d=0} = \pi v_F/L$ for a piecewise constant potential. The enhancement factor for the parameters of the experiment of Ref. [50] takes a value of $\eta \approx 2$. The physical reason for this enhancement is now clear; rather than being confined to the ribbon of length $2L$, the electron states in the presence of doping from the contacts form standing waves between the two non-adiabatic regions that introduce electron scattering at $x = \pm x_0$. The oscillation period ΔV_b of F as a function of back-gate voltage is thus enhanced by a factor L/x_0.

Unfortunately, our above analytic approach breaks down at $|V_b| \lesssim v_F^{2/3}\gamma^{1/3}$, the regime $V_b \in I_D$ of the experimentally most interesting first Fano factor maximum. Physically, this is the regime where the potential may not be linearized in the non-adiabatic regions. In this case, the two non-adiabatic regions merge into one. To access that regime, we next perform numerical calculations of the transfer matrix.

5.3 Numerical calculation

In this section, we obtain the transmission probability by numerical integration of Eq. (121). At $|x| \to \infty$, the potential is large and the transport semi-classical. As explained above, this causes the transport to be independent of the precise shape of the potential. For what follows, we assume a large and spatially constant potential value $v_F\kappa$ such that, for $x \to \infty$, one has

$$i\partial_x \psi = \kappa \sigma_x \psi. \tag{149}$$

The general solution to this equation is a linear combination of right and left moving waves:

$$\psi_{\rightleftarrows} = e^{\pm i\kappa x} \begin{pmatrix} 1 \\ \pm 1 \end{pmatrix}. \tag{150}$$

Here, the subscript arrows refer to the direction of propagation. We choose the boundary condition

$$\psi(-L) = \begin{pmatrix} 1 \\ \\ 1 \end{pmatrix}, \tag{151}$$

which ensures that all states incoming from the left are right moving.

By the definition of the transfer matrix, the wave function for $x \to \infty$, far to the right of the non adiabatic regions, is obtained from the one far to the left as

$$\psi(x) = M(x, -x)\psi_{\rightarrow}(-x). \tag{152}$$

Noting that the columns of the matrix A, Eq. (97), are the spinors $\psi_{\rightleftarrows}$ of Eq. (150), we observe that $M(x, -x)\psi_{\rightarrow}(-x)$ equals the first column of the matrix $M(x, -x)A_{-}(-x)$. According to Eq. (99), the latter matrix is equal to

$$A_{+}(x) \begin{pmatrix} \alpha & \beta^* \\ \\ \beta & \alpha^* \end{pmatrix}. \tag{153}$$

Together with Eq. (152), the second component of $\psi(x)$ at $x \to \infty$ thus satisfies

$$|\psi_2(x)|^2 = |\alpha|^2 + |\beta|^2 + 2\,|\alpha\beta| \cos(\kappa x + \vartheta), \tag{154}$$

where ϑ is the difference of the complex phases of α and β. To extract α from a numerical solution of ψ, we maximize that solution over the adiabatic region to the right of the classical turning points:

$$\begin{aligned} \zeta &\equiv \max_{x \gg x_0} |\psi_2|^2 \\ &= |\alpha|^2 + |\beta|^2 + 2\,|\alpha\beta|\,. \end{aligned} \tag{155}$$

Finally, we exploit current conservation $|\alpha|^2 - |\beta|^2 = 1$, and solve Eq. (155) for the transmission $T = 1/|\alpha|^2$, which results in

$$T = \frac{4\zeta}{(1+\zeta)^2}. \tag{156}$$

We conclude that the transmission probability T may be extracted from a numerical solution of $\psi(x)$ for $x \gg x_0$, with the boundary condition Eq. (151), by maximizing that solution over the adiabatic region to the right of the classical turning points.

Numerical results for the Fano factor obtained by this procedure are plotted in Fig. 18 (circles). At $|V_b| \gg v_{\mathrm{F}}^{2/3}\gamma^{1/3}$, where our analytic approach is justified, the curve agrees with our analytic results, as expected. Our numerical calculation confirms what we had observed analytically for the first and most relevant Fano factor maximum with $|V_b| \gg v_{\mathrm{F}}^{2/3}\gamma^{1/3}$. Doping from the contacts increases the voltage scale of the Fano factor oscillations. From the full width at half maximum of our numerical results, we conclude that the width of the first peak of the Fano factor is enhanced by a factor $\eta \approx 1.7$ compared to the theory neglecting doping from the leads.

5.3.1 Digression on an alternate extraction method

Alternatively, the transmission probability can be extracted from the wave functions by averaging Eq. (154) over a range of x within the adiabatic region to the right of the potential center. We then have

$$\langle \left| \psi_1^{(R)} \right|^2 \rangle_x = |\alpha|^2 + |\beta|^2 \,. \tag{157}$$

Using the specific form of the transfer matrix elements as above, we find

$$T = \frac{2}{1 + \langle \left| \psi_1^{(R)} \right|^2 \rangle_x}. \tag{158}$$

While either extraction method may be used to obtain the transmission probability, we note that the method involving the maximum of the wave function will, in general, be more accurate than the method involving the average, as it does not depend as strongly on the specific length scale chosen for the adiabatic region. Both solutions will agree exactly in the case where the wave functions can be found analytically.

5.4 Discussion and Conclusions

In conclusion, we have shown that the anomalously large voltage scale observed in the GNR shot noise experiments of Danneau *et al.* [50] is consistent with evanescent wave transport when the effect of doping by the contacts is accounted for. We have identified a regime of small graphene-back-gate distances where the effects of screening by conduction electrons in the GNR can be neglected. In this regime, we find the electric potential on the GNR with contacts, and we use it to obtain the Fano factor as a function of the back-gate voltage.

We employ both a semi-classical and a numerical approach to the transport. The semi-classical approach illuminates the origin of the predicted increased gate voltage period of the Fano factor. The potential due to doping from the leads introduces electron scattering around, generally, two pairs of classical turning points of the conduction electrons at distance $2x_0 < 2L$. The standing waves that form in between cause oscillations of the Fano factor with period $\Delta V_b \simeq v_{\rm F}/x_0$, which is larger than the scale $\Delta V_b \simeq v_{\rm F}/L$ of the same oscillations without doping by the contacts. Our numerical results show that the contact potential enhances ΔV_b by a factor of $\eta \approx 2$, consistent with the experimental observations. [50] However, the limit Eq. (134) assumed in this article in order to neglect screening by the GNR is not well satisfied in the experiment of Ref. [50]. Our calculations therefore provide a more qualitative than quantitative explanation of the observations of Danneau *et al.* [50] Most importantly, they demonstrate that an interpretation of that experiment in terms of evanescent waves is possible and strongly indicated, despite the discussed discrepancy with the original theory.

CHAPTER VI

CONCLUSION

Clean graphene exhibits non-equilibrium current fluctuations, or shot noise, near the Dirac point [167]. Even in impurity free graphene, evanescent modes lead to scattering, producing shot noise. For short and wide graphene strips, the Fano factor takes the universal value $F = 1/3$ at the Dirac point, decaying with increasing chemical potential as modes become propagating. The experimental verification of this prediction suggests that transport at the Dirac point of graphene is carried by evanescent modes. However, two problems persist. First, the Fano factor value $F = 1/3$ is ambiguous, as the Fano factor also assumes this value in disordered metals. Second, the experimentally observed voltage scale for the Fano factor is considerably larger than that predicted by theory. [50] These unresolved issues motivated this work.

To remove the Fano factor ambiguity, we propose several new geometries. For two evanescent graphene regions of equal length, separated by a long highly doped region and contacted at either end by ideal leads, we analytically derive a universal Fano factor $F = 1/4$ under certain conditions, clearly distinct from the value in the presence of disorder. A measurement of this value of the Fano factor can provide unambiguous evidence of transport through evanescent modes. We further calculate the Fano factor profile as asymmetries are introduced, providing another signature of evanescent modes. In the same geometry, the Fano factor can also be controlled by tuning the potential in one evanescent region. The crossover from $F = 1/4$ to $F = 1/3$ as a function of gate voltage is another novel signature of evanescent modes.

We extend this calculation for two evanescent regions to an arbitrary number of

evanescent regions, separated by highly doped regions. For such graphene superlattices, the Fano factor at the Dirac point shows a strong dependence on the number of evanescent regions, decaying quickly from $F = 1/3$ for one region to the limiting value $F = 1/(8 \ln 2)$ for an infinitely long superlattice, a result we calculate analytically in certain limits. We have provided a number of geometries with novel, universal values of the Fano factor, and the experimental verification of these predictions can be an unambiguous demonstration of transport through evanescent modes.

For the case of a single evanescent region, we provide an explanation for the anomalous gate voltage dependence of the Fano factor observed experimentally. Due to doping by the contacts to the electrical circuit, the potential profile in the graphene ribbon deviates from the square well potential considered in the seminal work of Tworzydło *et al.* [167] We calculate the true potential using a conformal mapping technique, and identify a parameter regime where the screening by the graphene conduction electrons is negligible. Using this potential, we calculate the transfer matrix semi-classically in order to obtain the Fano factor as a function of back-gate voltage. Despite the modified potential, we find a Fano factor maximum of $F = 1/3$, as in the experiment. We support these semi-classical results numerically, finding an enhancement of the voltage scale by a factor $\eta \approx 2$, consistent with the experimental observations.

Hence, we find that the experimental results are compatible with theoretical considerations of evanescent mode transport when the effect of doping from the contacts is accounted for. Moreover, our analytical calculation provide a physical explanation of this enhanced voltage scale. The potential due to doping from the leads introduces electron scattering around two pairs of classical turning points of the conduction electrons at distance less than the length of the full ribbon. The standing waves that form in between cause oscillations of the Fano factor, with a period that is larger than the scale of the same oscillations in the absence of doping effects from the leads.

In summary, we have provided new geometries that allow for unambiguous experimental tests of evanescent wave transport in graphene using shot noise measurements. The Fano factor can be controlled through either spatial asymmetry or gate voltage. We have extended these considerations to graphene superlattices, where we find yet another novel Fano factor value. By accounting for the effect of doping by the contacts, we find that the current experimental evidence for evanescent mode transport is, in fact, consistent with theoretical predictions.

APPENDIX A

GRAPHENE BOUNDARY CONDITIONS

In this thesis, we consider boundary conditions that do not mix modes at the doped-undoped graphene interfaces. In particular, we use the infinite mass and semiconducting and metallic armchair boundary conditions.

A.1 Infinite mass boundary confinement

The infinite mass boundary condition, discussed by Berry and Mondragon, [22] restricts the charge carriers to a finite domain via an additional mass term in the Hamiltonian. The Dirac Hamiltonian of Eq. (12) with potential $V(x)$ is amended to become

$$H = v_{\mathrm{F}}\vec{\sigma}_{\gamma}\cdot\vec{p} + v^{2}M(y)\sigma_{z} + V(x). \tag{159}$$

The mass term $M(y)$ is zero within the graphene strip, and it rises to $+\infty$ at the boundaries $y = 0$ and $y = W$. This confines the particles to the interior of the strip.

Suppose that the particles are confined to a finite domain D parametrized by an arc length s and possessing an outward unit normal vector $\vec{n}(s) = (\cos\alpha(s), \sin\alpha(s))$, where $\alpha(s)$ is the angle between the outward normal and the x-axis at the point s. As shown by Berry and Mondragon, [22] the condition that the Hamiltonian remain hermitian (the expectation value of the energy in any state ψ must be real) implies that the infinite mass boundary condition must ensure that there is no outward current at any point s on the boundary of D. This condition is equivalent to the boundary condition

$$\psi_{2}/\psi_{1} = iBe^{i\alpha(s)}, \tag{160}$$

where B is a real number, possibly depending on s, that is determined by the limiting

behavior of the mass term $M(y)$ at the boundary.

It can be shown [22] that $B = 1$ for the case where $M(y) \to \infty$ outside of D. For the geometry considered here, the unit normal makes an angle of $\alpha = \pi/2$ for all points along the boundary $y = W$ and $\alpha = -\pi/2$ for all points along the boundary $y = 0$. Hence, the infinite mass boundary condition in this geometry is

$$\begin{aligned} \psi|_{y=0} &= \sigma_x \psi|_{y=0}, \\ \psi|_{y=W} &= -\sigma_x \psi|_{y=W}. \end{aligned} \tag{161}$$

Application of this boundary condition to the plane wave solutions to the Dirac equation given in Eq. (57) leads to a quantized transverse wave number of the form

$$q_n = \tfrac{\pi}{W}\left(n + \tfrac{1}{2}\right); \quad n = 0, 1, 2... \tag{162}$$

The extra factor of $1/2$ arises from the π shift in the infinite mass boundary condition.

A.2 Metallic and semiconducting armchair edge boundary conditions

Graphene nano-ribbons with armchair boundary conditions have been studied experimentally [76] as well as theoretically [66, 15, 152]. Theoretically, both the tight-binding model and the massless two dimensional Dirac equation predict that ribbons with armchair edges can be metallic or semiconducting, depending on the width of the ribbon [152]. The form of the boundary conditions for the massless Dirac equation, as considered in this thesis, is provided by Brey and Fertig, [30] who find that the band structure is gapless only when the width expressed in units of the lattice constant is divisible by three.

Physically, the armchair edge boundary condition requires that the wave function vanish on both graphene sublattices at the edge of the nano-ribbon. This is accomplished by mixing states (ψ_A, ψ_B) from the K point with states (ψ'_A, ψ'_B) from the K' point. The states with primed wave functions satisfy the same Dirac equation as the

unprimed wave functions with $p_y \to -p_y$. The armchair edge boundary condition is then given by [30]

$$\psi_\mu(y=0) = \psi'_\mu(y=0)$$
$$\psi_\mu(y=W) = \psi'_\mu(y=W)e^{i\phi}; \quad \phi = \tfrac{2\pi}{3a_0}W \ ,$$

where $\mu = \{A, B\}$, a_0 is the lattice constant and W is the width of the ribbon. The phase ϕ is a multiple of 2π for the metallic state, where the width is a multiple of three times the lattice constant. Otherwise, for the semiconducting cases, the phase is a multiple of $\pm 2\pi/3$.

Application of the metallic armchair edge boundary condition to the plane wave solutions of the Dirac equation Eq. (57) gives the transverse wave number as $q_n = n\pi/W$. Similarly, the transverse wave number for the semiconducting armchair edge is found the be $q_n = (n + 1/3)\,\pi/W$.

In summary, the transverse wave number for these boundary conditions is given by $q_n = (n + \alpha)\,\pi/W$, where

$$\alpha = \begin{cases} 1/2 & \text{infinite mass} \\ 0 & \text{metallic armchair} \\ 1/3 & \text{semiconducting armchair.} \end{cases} \tag{163}$$

In the continuum limit $W \gg L, R$, the transport properties should be independent of the boundary conditions, and α drops out of the calculation.

REFERENCES

[1] Abedpour, N., Esmailpour, A., Asgari, R., and Tabar, M. R., "Conductance of a disordered graphene superlattice," *Phys. Rev. B*, vol. 79, p. 165412, 2009.

[2] Acheson, E. G., "Deflocculated graphite," *J. Franklin Inst.*, vol. 164, p. 375, 1907.

[3] Akhmerov, A. R. and Beenakker, C. W. J., "Boundary conditions for Dirac fermions on a terminated honeycomb lattice," *Phys. Rev. B*, vol. 77, p. 085423, 2008.

[4] Akimenko, A. I., Verkin, A. B., and Yanson, I. K., "Point-contact noise spectroscopy of phonons in metals," *J. Low Temp. Phys.*, vol. 54, p. 247, 1984.

[5] Altshuler, B. L., Levitov, L. S., and Yakovets, Y. A., "Nonequilibrium noise in a mesoscopic conductor: a microscopic analysis," *JETP Lett.*, vol. 59, p. 857, 1994. [Pis'ma Zh. Éksp. Teor. Fiz. **59**, 821 (1994)].

[6] Ando, T., Nakanishi, T., and Saito, R., "Berry's phase and absence of back scattering in carbon nanotubes," *J. Phys. Soc. Japan*, vol. 67, p. 2857, 1998.

[7] Andreoni, W., *The Physics of Fullerene-Based and Fullerene-Related Materials*. Berlin: Springer, 1 ed., 2000.

[8] Arovas, D. P., Brey, L., Fertig, H. A., Kim, E.-A., and Ziegler, K., "Dirac spectrum in piecewise constant one-dimensional (1D) potentials," *New J. Phys.*, vol. 12, p. 123020, 2010.

[9] Ashcroft, N. W. and Mermin, N. D., *Solid state physics*. Philadelphia: Saunders College, 1 ed., 1976.

[10] Averin, D. V., "Charge sensitivity of the single electron tunneling transistor with discrete energy spectrum," *J. Appl. Phys.*, vol. 73, p. 2593, 1993.

[11] Baranger, H. U. and Mello, P. A., "Mesoscopic transport through chaotic cavitites: a random S-matrix theory," *Phys. Rev. Lett.*, vol. 73, p. 142, 1994.

[12] Baranger, H. U. and Stone, A. D., "Electrical linear-response theory in an arbitrary magnetic field: a new Fermi surface formation," *Phys. Rev. B*, vol. 40, p. 8169, 1989.

[13] Barbier, M., Peeters, F. M., Vasilopoulos, P., and Pereira Jr., J. M., "Dirac and Klein-Gordon particles in one-dimensional periodic potentials," *Phys. Rev. B*, vol. 77, p. 115446, 2008.

[14] Barbier, M., Vasilopoulos, P., and Peeters, F. M., "Dirac electrons in a Kronig-Penney potential: Dispersion relation and transmission periodic in the strength of the barriers," *Phys. Rev. B*, vol. 80, p. 205415, 2009.

[15] Barone, V., Hod, O., and Scuseria, G. E., "Electronic structure and stability of semiconducting graphene nanoribbons," *Nano Lett.*, vol. 6, p. 2748, 2006.

[16] Barraza-Lopez, S., Kindermann, M., and Chou, M. Y., "Charge transport through graphene junctions with wetting metal leads," *Nano Lett.*, vol. 12, p. 3424, 2012.

[17] Barraza-Lopez, S., Vanević, M., Kindermann, M., and Chou, M. Y., "Effects of metallic contacts on electron transport through graphene," *Phys. Rev. Lett.*, vol. 104, p. 076807, 2010.

[18] Beenakker, C. W. J., "Random-matrix theory of quantum transport," *Rev. Mod. Phys.*, vol. 69, p. 731, 1997.

[19] Beenakker, C. W. J. and Büttiker, M., "Suppression of shot noise in metallic diffusive conductors," *Phys. Rev. B*, vol. 46, p. 1889, 1992.

[20] Berger, C., Song, Z., Li, T., Li, X., Ogbazghi, A. Y., Feng, R., Dai, Z., Marchenkov, A. N., Conrad, E. H., First, P. N., and de Heer, W. A., "Ultrathin epitaxial graphite: 2D electron gas properties and a route toward graphene-based nanoelectronics," *J. Phys. Chem. B*, vol. 108, p. 19912, 2004.

[21] Berry, M. V., "Quantal phase factor accompanying adiabatic change," *Proc. R. Soc. Lond.*, vol. A 392, p. 45, 1984.

[22] Berry, M. V. and Mondragon, R. J., "Neutrino billiards: time-reversal symmetry-breaking without magnetic fields," *Proc. R. Soc. Lond.*, vol. A 412, p. 53, 1987.

[23] Birk, H., de Jong, M. J. M., and Schönberger, C., "Shot-noise suppression in the single-electron tunneling regime," *Phys. Rev. Lett.*, vol. 75, p. 1610, 1995.

[24] Blanter, Y. M. and Büttiker, M., "Shot-noise current-current correlations in multiterminal diffusive conductors," *Phys. Rev. B*, vol. 56, p. 2127, 1997.

[25] Blanter, Y. M. and Büttiker, M., "Shot noise in mesoscopic conductors," *Physics Reports*, vol. 336, p. 1, 2000.

[26] Bliokh, Y. P., Freilikher, V., Savel'ev, S., and Nori, F., "Transport and localization in periodic and disordered graphene superlattices," *Phys. Rev. B*, vol. 79, p. 075123, 2009.

[27] Boehm, H. P., Clauss, A., Fischer, G. O., and Hofmann, U., "Dünnste Kholenstuff-Folien," *Z. Naturforschg.*, vol. 17, p. 150, 1962.

[28] Boehm, H. P., Setton, R., and Stumpp, E., "Nomenclature and terminology of graphite intercalation compounds," *Carbon*, vol. 24, p. 241, 1986.

[29] Boyle, W. S. and Noziéres, P., "Band structure and infrared absorption of graphite," *Phys. Rev.*, vol. 111, p. 782, 1958.

[30] Brey, L. and Fertig, H. A., "Electronic states of graphene nanoribbons," *Phys. Rev. B*, vol. 73, p. 235411, 2006.

[31] Brey, L. and Fertig, H. A., "Emerging zero modes for graphene in a periodic potential," *Phys. Rev. Lett.*, vol. 103, p. 046809, 2009.

[32] Brodie, B. C., "On the atomic weight of graphite," *Proc. R. Soc. Lond.*, vol. 10, p. 249, 1859.

[33] Bürki, J. and Stafford, C. A., "Comment on "Quantum suppression of shot noise in atom-size metallic contacts"," *Phys. Rev. Lett.*, vol. 83, p. 3342, 1999.

[34] Büttiker, M., "Four-terminal phase-coherent conductance," *Phys. Rev. Lett.*, vol. 57, p. 1761, 1986.

[35] Büttiker, M., "Symmetry of electrical conduction," *IBM J. Res. Dev.*, vol. 32, p. 317, 1988.

[36] Büttiker, M., "Quantized transmission of a saddle-point constriction," *Phys. Rev. B*, vol. 41, p. 7906, 1990.

[37] Büttiker, M., "Scattering theory of thermal and excess noise in open conductors," *Phys. Rev. Lett.*, vol. 65, p. 2901, 1990.

[38] Büttiker, M., "Scattering theory of current and intensity noise correlations in conductors and wave guides," *Phys. Rev. B*, vol. 46, p. 12485, 1992.

[39] Callen, H. B. and Welton, T. A., "Irreversibility and generalized noise," *Phys. Rev.*, vol. 83, p. 34, 1951.

[40] Calogeracos, A. and Dombey, N., "History and physics of the Klein paradox," *Contemp. Phys.*, vol. 40, p. 313, 1999.

[41] Castro Neto, A., Guinea, F., and Peres, N. M., "Drawing conclusions from graphene," *Phys. World*, vol. 19, p. 33, 2006.

[42] Castro Neto, A. H., Guinea, F., Peres, N. M. R., Novoselov, K. S., and Geim, A. K., "The electronic properties of graphene," *Rev. Mod. Phys.*, vol. 81, p. 109, 2009.

[43] Cayssol, J., Huard, B., and Goldhaber-Gordon, D., "Contact resistance and shot noise in graphene transistors," *Phys. Rev. B*, vol. 79, p. 075428, 2009.

[44] Chang, L. L., Esaki, L., and Tsu, R., "Resonant tunneling in semiconductor double barriers," *Appl. Phys. Lett.*, vol. 24, p. 593, 1974.

[45] Charlier, J.-C., Blase, X., and Roche, S., "Electronic and transport properties of nanotubes," *Rev. Mod. Phys.*, vol. 79, p. 677, 2007.

[46] Cheianov, V. V. and Fal'ko, V. I., "Selective transmission of Dirac electrons and ballistic magnetoresistance of p-n junctions in graphene," *Phys. Rev. B*, vol. 74, p. 041403(R), 2006.

[47] Chen, L. Y. and Ting, C. S., "Theoretical investigation of noise characteristics of double-barrier resonant-tunneling systems," *Phys. Rev. B*, vol. 43, p. 4534, 1991.

[48] Chen, L. Y. and Ying, S. C., "Shot noise suppression in quantum point contact systems," *Mod. Phys. Lett. B*, vol. 9, p. 573, 1995.

[49] Dahm, A. J., Denenstein, A., Langenberg, D. N., Parker, W. H., Rogovin, D., and Scalapino, D. J., "Linewidth of the radiation emitted by a Josephson junction," *Phys. Rev. Lett.*, vol. 22, p. 1416, 1969.

[50] Danneau, R., Wu, F., Craciun, M. F., Russo, S., Tomi, M. Y., Salmilehto, J., Morpurgo, A. F., and Hakonen, P. J., "Shot noise in ballistic graphene," *Phys. Rev. Lett.*, vol. 100, p. 196802, 2008.

[51] Das Sarma, S., Adam, S., Hwang, E. H., and Rossi, E., "Electronic transport in two-dimensional graphene," *Rev. Mod. Phys.*, vol. 83, p. 407, 2007.

[52] Davenport Jr., W. B. and Root, W. L., *An introduction to the theory of random signals and noise*. New York: Wiley-IEEE Press, 1 ed., 1987.

[53] Davies, J. H., Hyldgaard, P., Hershfield, S., and Wilkins, J. W., "Classical theory for shot noise in resonant tunneling," *Phys. Rev. B*, vol. 46, p. 9620, 1992.

[54] de Heer, W. A., "Epitaxial graphene: a new electronic material for the 21st century," *MRS Bulletin*, vol. 36, p. 632, August 2011.

[55] de Jong, M. J. M. and Beenakker, C. W. J., "Shot noise in mesoscopic systems," in *Mesoscopic electron transport* (Sohn, L. L., Kouwenhoven, L. P., and Schön, G., eds.), vol. Nato ASI Series E Vol. 345, pp. 225–258, Boston: Springer, 1 ed., 1997.

[56] de Jonge, N., Allioux, M., Oostveen, J. T., Teo, K. B., and Milne, W. I., "Low noise and stable emission from carbon nanotube electron sources," *Appl. Phys. Lett.*, vol. 87, p. 133118, 2005.

[57] Deacon, R. S., Chuang, K.-C., Nicholas, R. J., Novoselov, K. S., and Geim, A. K., "Cyclotron resonance study of the election and hole velocity in graphene monolayers," *Phys. Rev. B*, vol. 76, p. 081406(R), 2007.

[58] Dekker, C., Scholten, A. J., Liefrink, F., Eppenga, R., van Houten, H., and Foxon, C. T., "Spontaneous resistance switching and low-frequency noise in quantum point contacts," *Phys. Rev. Lett.*, vol. 66, p. 2148, 1991.

[59] DiCarlo, L., Williams, J. R., Zhang, Y., McClure, D. T., and Marcus, C. M., "Shot noise in graphene," *Phys. Rev. Lett.*, vol. 100, p. 156801, 2008.

[60] Dillon, R. O., Spain, I. L., and McClure, J. W., "Electronic energy band parameters of graphite and their dependence on pressure, temperature and acceptor concentration," *J. Phys. Chem. Solids*, vol. 38, p. 635, 1977.

[61] Dumitrescu, V. I., "The prehistory of the balkans to 1000 B.C.," in *The Cabridge ancient history Vol. 3 Pt. 1: the prehistory of the Balkans; and the middle Aegean world, tenth to eighth centuries B.C.* (Boardman, J., Edwards, I. E. S., Hammond, N. G. L., and Sollberger, E., eds.), pp. 36–37, New York, NY: Cambridge University Press, 2006.

[62] Fauser, B., Tolksdorf, J., and Zeidler, E., *Quantum Gravity*. Basel: Birkhäuser, 1 ed., 2007.

[63] Fisher, D. S. and Lee, P. A., "Relation between conductivity and transmission matrix," *Phys. Rev. B*, vol. 23, p. 6851, 1981.

[64] Fogler, M. M., Novikov, D. S., Glazman, L. I., and Shklovskii, B. I., "Effect of disorder on a graphene *p-n* junction," *Phys. Rev. B*, vol. 77, p. 075420, 2008.

[65] Forbeaux, I., Themlin, J.-M., and Debever, J.-M., "Heteroepitaxial graphite on 6H-SiC(0001): Iinterface formation through conduction-band electronic structure," *Phys. Rev. B*, vol. 58, p. 16396, 1998.

[66] Fujita, M., Wakabayashi, K., Nakada, K., and Kusakabe, K., "Peculiar localized state at zigzag graphite edge," *Journal of the Physical Society of Japan*, vol. 65, p. 1920, 1996.

[67] Fürst, J. A., Pedersen, J. G., Flindt, C., Mortensen, N. A., Brandbyge, M., Pedersen, T. G., and Jauho, A.-P., "Electronic properties of graphene antidot lattices," *New J. Phys.*, vol. 11, p. 095020, 2009.

[68] Geim, A. K. and Novoselov, K. S., "The rise of graphene," *Nat. Mat.*, vol. 6, pp. 183–191, 2007.

[69] Glazman, L. I., Lesovik, G. B., Khmel'nitskii, D. E., and Shekhter, R. I., "Reflectionless quantum transport and fundamental ballistic-resistance steps in microscopic constrictions," *JETP Lett.*, vol. 48, p. 238, 1988. [Pis'ma Zh. Éksp. Teor Fiz. **48**, 218 (1988)].

[70] Golub, A. and Horovitz, B., "Shot noise in graphene with long-range Coulomb interaction and local Fermi distribution," *Phys. Rev. B*, vol. 81, p. 245424, 2010.

[71] González, J., Guinea, F., and Vozmediano, M. A. H., "Marginal fermi-liquid behavior from two-dimensional Coulomb interaction," *Phys. Rev. B*, vol. 59, p. 2474, 1988.

[72] Gorbar, E. V., Gusynin, V. P., Miransky, V. A., and Shovkovy, I. A., "Magnetic field drive metal-insulator phase transition in planar surfaces," *Phys. Rev. B*, vol. 66, p. 045108, 2002.

[73] Gray, P. R., Hurst, P. J., Lewis, S. H., and Meyer, R. G., *Analysis and design of analog integrated circuits*. New York: Wiley, 5 ed., 2009.

[74] Gusynin, V. P. and Sharapov, S. G., "Unconventional integer quantum Hall effect in graphene," *Phys. Rev. Lett.*, vol. 95, p. 146801, 2005.

[75] Haldane, F. D. M., "Model for a quantum hall effect without Landau levels," *Phys. Rev. Lett.*, vol. 61, p. 2015, 1988.

[76] Han, M. Y., Özyilmaz, B., Zhang, Y., and Kim, P., "Energy band-gap engineering of graphene nanoribbons," *Phys. Rev. B*, vol. 98, p. 206805, 2007.

[77] Henny, M., Oberholzer, S., Strunk, C., and Schönenberger, C., "1/3-shot-noise suppression in diffusive nanowires," *Phys. Rev. B*, vol. 59, p. 2871, 1999.

[78] Hermann, L. G., Delattre, T., Morfin, P., Berroir, J.-M., Plaçais, B., Glattli, D. C., and Kontos, T., "Shot noise in Fabry-Perot interferometers based on carbon nanotubes," *Phys. Rev. Lett.*, vol. 99, p. 156804, 2007.

[79] Huard, B., Sulpizio, J. A., Stander, N., Todd, K., Yang, B., and Goldhaber-Gordon, D., "Transport measurements across a tunable potential barrier in graphene," *Phys. Rev. Lett.*, vol. 98, p. 236803, 2007.

[80] Imry, Y., "Physics of mesoscopic systems," in *Directions in condensed matter physics* (Grinstein, G. and Mazenko, G., eds.), pp. 101–152, Philadelhia, PA: World Scientific Publishing, 1 ed., 1986.

[81] Itzykson, C. and Zuber, J.-B., *Quantum Field Theory*. New York: Dover, 2006.

[82] Jalabert, R. A., Pichard, J.-L., and Beenakker, C. W. J., "Universal quantum signatures of chaos in ballistic transport," *Europhys. Lett.*, vol. 27, p. 255, 1994.

[83] Jiang, Z., Henriksen, E. A., Tung, L. C., Wang, Y.-J., Schwartz, M. E., Han, M. Y., Kim, P., and Stormer, H. L., "Infrared spectroscopy of Landau levels go graphene," *Phys. Rev. Lett.*, vol. 98, p. 197403, 2007.

[84] Johnson, J. B., "Thermal agitation of electricity in conductors," *Phys. Rev.*, vol. 32, p. 97, 1928.

[85] Katsnelson, M. I., "Zitterbewegung, chirality, and minimal conductivity in graphene," *Eur. Phys. J. B*, vol. 51, p. 157, 2006.

[86] Katsnelson, M. I. and Novoselov, K. S., "Graphene: New bridge between condensed matter physics and electrodynamics," *Solid State Comm.*, vol. 143, p. 3, 2007.

[87] Katsnelson, M. I., Novoselov, K. S., and Geim, A. K., "Chiral tunneling and the Klein paradox in graphene," *Nature Phys.*, vol. 2, p. 620, 2006.

[88] Khlus, V. A., "Current and voltage fluctuations in the microcontacts of normal and superconductive metals," *Sov. Phys. JETP*, vol. 66, p. 1243, 1987. [Zh. Éksp. Teor. Fiz. **93**, 2179 (1987)].

[89] Klein, O., "Die reflexion von elektronen an einem potentialsprung nach der relativischen dynamik von Dirac," *Z Phys.*, vol. 53, p. 157, 1929.

[90] Kumar, A., Saminadayar, L., Glattli, D. C., Jin, Y., and Etienne, B., "Experimental test of the quantum shot noise reduction theory," *Phys. Rev. Lett.*, vol. 76, p. 2778, 1996.

[91] Landauer, R., "Spatial variation of currents and fields due to localized scatterers in metallic conduction," *IBM J. Res. Dev.*, vol. 1, p. 223, 1957.

[92] Landauer, R., "Johnson-Nyquist noise derived from quantum mechanical transmission," *Physica D*, vol. 38, p. 226, 1989.

[93] Landauer, R. and Martin, T., "Equilibrium and shot noise in mesoscopic systems," *Physica B*, vol. 175, p. 167, 1991.

[94] Larkin, A. I. and Ovchinnikov, Y. N., "Radiation line width in the Josephson effect," *Sov. Phys. JETP*, vol. 26, p. 1219, 1968. [Zh. Éksp. Teor. Fiz. **53**, 2159 (1968)].

[95] Larkin, I. A. and Reznikov, M., "Shot noise and I-V curve in a ballistic quantum point contact," in *Proceedings of the 23rd international conference on the physics of semiconductors* (Scheffler, M. and Zimmermann, R., eds.), (Singapore), p. 1565, World Scientific, 1996.

[96] Lee, H. and Levitov, L. S., "Current fluctuations in a single tunnel junction," *Phys. Rev. B*, vol. 53, p. 7383, 1996.

[97] Lemme, M. C., Echtermeyer, T. J., Baus, M., and Kurz, H., "A graphene field-effect device," *IEEE Electron Device Lett.*, vol. 28, p. 282, 2007.

[98] Lesovik, G. B., "Excess quantum noise in 2D ballistic point contacts," *JETP Lett.*, vol. 49, p. 592, 1989. [Pis'ma Zh. Éksp. Teor. Fiz. **49**, 513 (1989)].

[99] Levitov, L. S., Lee, H. W., and Lesovik, G. B., "Electron counting statistics and cohere states of electric current," *J. Math Phys.*, vol. 37, p. 4845, 1996.

[100] Levitov, L. S. and Lesovik, G. B., "Charge distributen in quantum shot noise," *JETP Lett.*, vol. 58, p. 230, 1993.

[101] Levitov, L. S. and Lesovik, G. B., "Quantum measurement in electric circuit." arxiv:cond-mat/9401004, 1994.

[102] Lewenkopf, C. H., Mucciolo, E. R., and Castro Neto, A. H., "Numerical studies of conductivity and Fano factor in disordered graphene," *Phys. Rev. B*, vol. 77, p. 081410(R), 2008.

[103] Li, Y. P., Tsui, D. C., Heremans, J. J., Simmons, J. A., and Weimann, G. W., "Low-frequency noise in transport through quantum point contacts," *Appl. Phys. Lett.*, vol. 57, p. 774, 1990.

[104] Liefrink, F., Dijkhuis, J. I., de Jong, M. J. M., Molenkamp, L. W., and van Houten, H., "Experimental study of reduced shot noise in a diffusive mesoscopic conductor," *Phys. Rev. B*, vol. 49, p. 14066, 1994.

[105] Liefrink, F., Scholten, A. J., Dekker, C., Eppenga, R., van Houten, H., and Foxon, C. T., "Low-frequency noise of quantum point contacts in the ballistic and quantum Hall regime," *Physica B*, vol. 175, p. 213, 1991.

[106] Liu, S. T. and van der Ziel, A., "Noise in thin film Al-Al_2O_3-Al diodes," *Physica*, vol. 37, p. 241, 1967.

[107] Low, T. and Appenzeller, J., "Electronic transport properties of a tilted graphene *p*-*n* junction," *Phys. Rev. B*, vol. 80, p. 155406, 2009.

[108] Lu, X., Yu, M., Huang, H., and Ruoff, R. S., "Tailoring graphite with the goal of achieving single sheets," *Nanotechnology*, vol. 10, p. 269, 1999.

[109] Martin, T. and Landauer, R., "Wave-packet approach to noise in multichannel mesoscopic systems," *Phys. Rev. B*, vol. 45, p. 1742, 1992.

[110] McClure, J. W., "Band structure of graphite and de Haas - van Alphen effect," *Phys. Rev.*, vol. 108, p. 612, 1957.

[111] McClure, J. W., "Analysis of multicarrier galvanomagnetic data for graphite," *Phys. Rev.*, vol. 112, p. 715, 1958.

[112] Merchant, C. A. and Marković, N., "Current and shot noise measurements in a carbon nanotube-based spin diode," *J. Appl. Phys.*, vol. 105, p. 07C711, 2009.

[113] Meyer, J. C., Geim, A. K., Katsnelson, M. I., Novoselov, K. S., Booth, T. J., and Roth, S., "The structure of suspended graphene sheets," *Nature*, vol. 446, p. 60, 2007.

[114] Miao, F., Wijeratne, S., Zhang, Y., Coskun, U., Bao, W., and Lau, C., "Phase coherent transport of charges in graphene quantum billiards," *Science*, vol. 317, p. 1530, 2007.

[115] Nagaev, K. E., "On the shot noise in dirty metal contacts," *Phys. Lett. A*, vol. 169, p. 103, 1992.

[116] Nakada, K., Fujita, M., Dresselhaus, G., and Dresselhaus, M. S., "Edge state in graphene ribbons: nanometer size effect and edge shape dependence," *Phys. Rev. B*, vol. 54, p. 17954, 1996.

[117] Nauen, A., Hapke-Wurst, I., Hohis, F., Zeitler, U., Haug, R. J., and Pierz, K., "Shot noise in self-assembled InAs quantum dots," *Phys. Rev. B*, vol. 66, p. 161303(R), 2002.

[118] Nauen, A., Hohis, F., Maire, N., Pierz, K., and Haug, R. J., "Shot noise in tunneling through a single quantum dot," *Phys. Rev. B*, vol. 70, p. 033305, 2004.

[119] Nazarov, Y. V., "Limits of universality in disordered conductors," *Phys. Rev. Lett.*, vol. 73, p. 134, 1994.

[120] Nelson, D., Piran, D. R., and Weinberg, S., *Statistical Mechanics of Membranes and Surfaces*. Singapore: World Scienfitic, 2 ed., 2004.

[121] Novoselov, K. S., Geim, A. K., Morozov, S. V., Jiang, D., Dubonos, S. V., Grigorieva, I. V., and Firsov, A. A., "Electric field effect in atomically thin carbon films," *Science*, vol. 306, p. 666, 2004.

[122] Novoselov, K. S., Geim, A. K., Morozov, S. V., Jiang, D., Katsnelson, M. I., Grigorieva, I. V., Dubonos, S. V., and Firsov, A. A., "Two-dimensional gas of massless Dirac fermions in graphene," *Nature*, vol. 438, p. 197, 2005.

[123] Novoselov, K. S., Jiang, Z., Zhang, Y., Morozov, S. V., Stormer, H. L., Zeitler, U., Mann, J. C., Boebinger, G. S., Kim, P., and Geim, A. K., "Room temperature quantum Hall effect in graphene," *Science*, vol. 315, p. 5817, 2007.

[124] Nyquist, H., "Thermal agitation of electric charge in conductors," *Phys. Rev.*, vol. 32, p. 110, 1928.

[125] Onac, E., Balestro, F., Trauzettel, B., Lodewijk, C. F. J., and Kouwenhoven, L. P., "Shot-noise detection in a carbon nanotube quantum dot," *Phys. Rev. Lett.*, vol. 96, p. 026803, 2006.

[126] Ouacha, H., Willander, M., Yu, H. Y., Park, Y. W., Kabir, M. S., Magnus Persson, S. H., Kish, L. B., and Ouacha, A., "Noise properties of an individual and two crossing multi walled carbon nanotubes," *Appl. Phys. Lett.*, vol. 80, p. 1055, 2002.

[127] Özyilmaz, B., Jarillo-Herrero, P., Efetov, D., Abanin, D. A., Levitov, L. S., and Kim, P., "Electronic transport and quantum hall effect in bipolar graphene *p-n-p* junctions," *Phys. Rev. Lett.*, vol. 99, p. 166804, 2007.

[128] Park, C.-H., Son, Y.-W., Yang, L., Cohen, M. L., and Louie, S. G., "Electron beam supercollimation in graphene superlattices," *Nano Lett.*, vol. 8, p. 2920, 2008.

[129] Park, C.-H., Son, Y.-W., Yang, L., Cohen, M. L., and Louie, S. G., "Landau levels and quantum hall effect in graphene superlattices," *Phys. Rev. Lett.*, vol. 103, p. 046808, 2009.

[130] Pedersen, M. H., van Langen, S. A., and Büttiker, M., "Charge fluctuations in quantum point contacts and chaotic cavities in the presence of transport," *Phys. Rev. B*, vol. 57, p. 1838, 1998.

[131] Pedersen, T. G., Flindt, C., Pedersen, J., Mortensen, N. A., Jauho, A.-P., and Pedersen, K., "Graphene antidot lattices: Designated defects and spin qubits," *Phys. Rev. Lett.*, vol. 100, p. 136804, 2008.

[132] Pereira Jr., J. M., Vasilopoulos, P., and Peeters, F. M., "Graphene-based resonant-tunneling structures," *Appl. Phys. Lett.*, vol. 90, p. 132122, 2007.

[133] Peres, N. M. R., Guinea, F., and Neto, A. H. C., "Electronic properties of disordered two-dimensional carbon," *Phys. Rev. B*, vol. 73, p. 125411, 2006.

[134] Peres, N. M. R., Neto, A. H. C., and Guinea, F., "Conductance quantization in mesoscopic graphene," *Phys. Rev. B*, vol. 73, p. 195411, 2006.

[135] Petroski, H., *The Pencil: A History of Design and Circumstance*. New York: Knopf, 1 ed., 1992.

[136] Reklaitis, A. and Reggiani, L., "Monte Carlo analysis of shot-noise suppression in tunneling transport through semiconductor heterostructures," *Phys. Stat. Sol. b*, vol. 204, p. 459, 1997.

[137] Reklaitis, A. and Reggiani, L., "Monte Carlo study of shot noise suppression," *J. Appl. Phys.*, vol. 82, p. 3161, 1997.

[138] Reznikov, M., Heiblum, M., Shtrikman, H., and Mahalu, D., "Temporal correlation of electrons: Suppression of shot noise in a ballistic quantum point contact," *Phys. Rev. Lett.*, vol. 75, p. 3340, 1995.

[139] Roche, P.-E., Kociak, M., Guéron, S., Kasumov, A., Reulet, B., and Bouchiat, H., "Very low shot noise in carbon nanotubes," *Eur. Phys. J. B*, vol. 28, p. 217, 2002.

[140] Rogovin, D. and Scalapino, D. J., "Tunnel junction current fluctuations," *Physica*, vol. 55, p. 399, 1971.

[141] Rogovin, D. and Scalapino, D. J., "Fluctuation phenomena in tunnel junctions," *Ann. Phys.*, vol. 86, p. 1, 1974.

[142] Rycerz, A., Recher, P., and Wimmer, M., "Conformal mapping and shot noise in graphene," *Phys. Rev. B*, vol. 80, p. 125417, 2009.

[143] Rycerz, A., Tworzydlo, J., and Beenakker, C. W. J., "Valley filter and valley valve in graphene," *Nat. Phys.*, vol. 3, p. 172, 2007.

[144] Saito, R., Dresselhaus, G., and Dresselhaus, M. S., *Physical properties of carbon nanotubes*. London: Imperial College Press, 1 ed., 1998.

[145] Saito, R., Fujita, M., Dresselhaus, G., and Dresselhaus, M. S., "Electronic structure of chiral graphene tubules," *Appl. Phys. Lett.*, vol. 60, p. 2204, 1992.

[146] San-Jose, P., Prada, E., and Golubev, D. S., "Universal scaling of current fluctuations in disordered graphene," *Phys. Rev. B*, vol. 76, p. 195445, 2007.

[147] Scherbakov, A. G., Bogachek, E. N., and Landman, U., "Noise in three-dimensional nanowires," *Phys. Rev. B*, vol. 57, p. 6654, 1998.

[148] Schön, G., "Quantum noise in tunnel junctions," *Phys. Rev. B*, vol. 32, p. 4469, 1985.

[149] Schottky, W., "Über spontane Stromschwankungen in verschiedenen Elektrizitätsleitern," *Ann. Phys.*, vol. 57, p. 541, 1918.

[150] Schuessler, A., Ostrovsky, P. M., Gornyi, I. V., and Mirlin, A. D., "Analytic theory of ballistic transport in disordered graphene," *Phys. Rev. B*, vol. 79, p. 075405, 2009.

[151] Semenoff, G. W., "Condensed matter simulation of a three dimensional anomaly," *Phys. Rev. Lett.*, vol. 53, p. 2449, 1984.

[152] Sen, Y. W., Cohen, M. L., and Louie, S. G., "Energy gaps in graphene nanoribbons," *Phys. Rev. Lett.*, vol. 97, p. 216803, 2006.

[153] Shepard, K., "Multichannel, multiprobe Landauer formula in the presence of a uniform magnetic field," *Phys. Rev. B*, vol. 43, p. 11623, 1991.

[154] Slonczewski, J. C. and Weiss, P. R., "Band structure of graphite," *Phys. Rev.*, vol. 109, p. 272, 1958.

[155] Snyman, I. and Beenakker, C. W. J., "Ballistic transmission through a graphene bilayer," *Phys. Rev. B*, vol. 75, p. 045322, 2007.

[156] Sonin, E. B., "Charge transport and shot noise in a ballistic graphene sheet," *Phys. Rev. B*, vol. 77, p. 233408, 2008.

[157] Soule, D. E., McClure, J. W., and Smith, L. B., "Study of Shubnikov-de Haas effect: Determination of the Fermi surfaces in graphite," *Phys. Rev.*, vol. 134, p. A453, 1964.

[158] Spry, W. J. and Scherer, P. M., "de Haas-van Alphen effect in graphite between 3 and 85 Kilogauss," *Phys. Rev.*, vol. 120, p. 826, 1960.

[159] Stander, N., Huard, B., and Goldhaber-Gordon, D., "Evidence for Klein tunneling in graphene p-n junctions," *Phys. Rev. Lett.*, vol. 102, p. 026807, 2009.

[160] Steinbach, A. H., Martinis, J. M., and Devoret, M. H., "Observation of hot-electron shot noise in a metallic resistor," *Phys. Rev. Lett.*, vol. 76, p. 3806, 1996.

[161] Stone, A. D., Mello, P. A., Muttalib, K. A., and Pichard, J.-L., "Random matrix theory and maximum entropy models for disordered conductors," in *Mesoscopic phenomena in solids* (Altshuler, B. L., Lee, P. A., and Webb, R. A., eds.), p. 369, Amsterdam: North-Holland, 1991.

[162] Stone, S. D. and Szafer, A., "What is measured when you measure resistance? – the Landauer formula revisited," *IBM J. Res. Dev.*, vol. 32, p. 384, 1988.

[163] Titov, M., "Impurity-assisted tunneling in graphene," *Europhys. Lett.*, vol. 79, p. 17004, 2007.

[164] Titov, M. and Beenakker, C. W. J., "Josephson effect in ballistic graphene," *Phys. Rev. B*, vol. 74, p. 041401(R), 2006.

[165] Tsu, R. and Esaki, L., "Tunneling in a finite superlattice," *Appl. Phys. Lett.*, vol. 22, p. 562, 1973.

[166] Tworzydło, J., Synman, I., Akhmerov, A. R., and Beenakker, C. W. J., "Valley-isospin dependence of the quantum hall effect in a graphene p-n junction," *Phys. Rev. B*, vol. 76, p. 035411, 2007.

[167] Tworzydło, J., Trauzettel, B., Titov, M., Rycerz, A., and Beenakker, C. W. J., "Sub-poissonian shot noise in graphene," *Phys. Rev. Lett.*, vol. 96, p. 246802, 2006.

[168] van Bommel, A. J., Crombeen, J. E., and van Tooren, A., "LEED and Auser electron observations of the SiC(0001) surface," *Surf. Sci.*, vol. 48, p. 463, 1975.

[169] van den Brom, H. E. and van Ruitenbeek, J. M., "Quantum suppression of shot noise in atom-size metallic contacts," *Phys. Rev. Lett.*, vol. 82, p. 1526, 1999.

[170] van der Ziel, A., *Noise in solid state devices and circuits*. New York: Wiley-Interscience, 1 ed., 1986.

[171] van Wees, B. J., van Houten, H., Beenakker, C. W. J., Williamson, J. G., Kouwenhoven, L. P., van der Marel, D., and Foxon, C. T., "Quantized conductance of point contacts in a two-dimensional electron gas," *PRL*, vol. 60, p. 848, 1988.

[172] Vanević, M., Stojanović, V. M., and Kindermann, M., "Character of electronic states in graphene antidot lattices: Flat bands and spatial localzation," *Phys. Rev. B*, vol. 80, p. 045410, 2009.

[173] Wakabayashi, K., Fujita, M., Ajiki, H., and Sigrist, M., "Electronic and magnetic properties of nanographite ribbons," *Phys. Rev. B*, vol. 59, p. 8271, 1999.

[174] Wallace, P. R., "The band theory of graphite," *Phys. Rev.*, vol. 71, p. 622, 1947.

[175] Wharam, D. A., Thornton, T. J., Newbury, R., Pepper, M., Ahmed, H., Frost, J. E. F., Hasko, D. G., Peacock, D. C., Ritchie, D. A., and Jones, G. A. C., "One-dimensional transport and the quantisation of the ballistic resistance," *J. Phys. C*, vol. 21, p. L209, 1988.

[176] Wiener, A. D. and Kindermann, M., "Effects of the contacts on shot noise in graphene nano-ribbons." in preparation.

[177] Wiener, A. D. and Kindermann, M., "Signatures of evanescent mode transport in graphene," *Phys. Rev. B*, vol. 84, p. 245420, 2011.

[178] Williams, J. R., DiCarlo, L., and Marcus, C. M., "Quantum hall effect in a gate-controlled p-n junction of graphene," *Science*, vol. 317, p. 638, 2007.

[179] Williamson, S. J., Foner, S., and Dresselhaus, M. S., "de Haas-van Alphen effect in pyrolytic and single-crystal graphite," *Phys. Rev.*, vol. 140, p. A1429, 1965.

[180] Wu, F., Queipo, P., Nasibulin, A., Tsuneta, T., Wang, T. H., Kauppinen, E., and Hakonen, P. J., "Shot noise with interaction effects in single-walled carbon nanotubes," *Phys. Rev. Lett.*, vol. 99, p. 156803, 2007.

[181] Wu, F., Tsuneta, T., Tarkiainen, R., Gunnarsson, D., Wang, T.-H., and Hakonen, P. J., "Shot noise of a multi walled carbon nanotube field effect transistor," *Phys. Rev. B*, vol. 75, p. 125419, 2007.

[182] Yurke, B. and Kochanski, G. P., "Momentum noise in vacuum tunneling transducers," *Phys. Rev. B*, vol. 41, p. 8184, 1990.

[183] Zhang, L. M. and Fogler, M. M., "Nonlinear screening and ballistic transport in a graphene *p-n* junction," *Phys. Rev. Lett.*, vol. 100, p. 116804, 2008.

[184] Zhang, Y., Tan, Y.-W., Stormer, H. L., and Kim, P., "Experimental observation of the quantum hall effect and Berry's phase in graphene," *Nature*, vol. 438, p. 201, 2005.

[185] Zheng, Y. and Ando, T., "Hall conductivity of a two-dimensional graphite system," *Phys. Rev. B*, vol. 65, p. 245420, 2002.

[186] Žutić, I., Fabian, J., and Das Sarma, S., "Spintronics: fundamentals and applications," *Rev. Mod. Phys.*, vol. 76, p. 323, 2004.

VITA

Alex Wiener was born in Nashua, NH in 1982. He attended Nashua High School before moving to New Orleans in 2001 to study math and physics at Tulane University. While at Tulane, Alex performed undergraduate research in experimental biophysics and quantum chaos, resulting in an honors thesis under Prof. Lev Kaplan. He also participated in the National Institute of Standards and Technology Research Experience for Undergraduates during the summer of 2003, and spent the following summer working with Prof. Hossein Sadeghpour on problems in molecular physics at the Institute for Theoretical Atomic, Molecular and Optical Physics at Harvard University. Alex graduated summa cum laude from Tulane in 2005 and moved to Atlanta to begin graduate studies at Georgia Tech in quantum information theory with Prof. Li You. After working for two years on entanglement measures, including a summer at the Kavli Institute for Theoretical Physics in Beijing, China in 2007, he began his doctoral research in condensed matter theory with Prof. Markus Kindermann, culminating in this thesis. When not writing a dissertation, Alex enjoys many styles of music and film, as well as participating in roller hockey and soccer.